2011

Investigations on Morphology, Spectroscopy and Near-infrared Photoresponse Sensitization of Conjugated Polymers in Organic Photovoltaics

Zhongjian Hu
University of Central Florida

INVESTIGATIONS ON MORPHOLOGY, SPECTROSCOPY AND NEAR-INFRARED PHOTORESPONSE SENSITIZATION OF CONJUGATED POLYMERS IN ORGANIC PHOTOVOLTAICS

by

ZHONGJIAN HU

B.S. Qufu Normal University, China, 2002
M.S. Graduate School of the Chinese Academy of Sciences, 2005

A dissertation submitted in partial fulfillment of the requirements
for the degree of Doctor of Philosophy
in the Department of Chemistry
in the College of Sciences
at the University of Central Florida
Orlando, Florida

Summer Term, 2011

Major Advisor: Andre J. Gesquiere

ABSTRACT

Conjugated polymer architecture and morphology are two of the key factors that determine corresponding opto-electronic device performance. It is well-known that conjugated polymers display a variety of conformations and exhibit aggregation in their materials and even for individual polymer chains. The intrinsic structural heterogeneity of conjugated polymers strongly complicates the active layer morphology and phase separation, which are crucial for photoinduced charge generation and transport in polymer based bulk heterojunction-organic photovoltaics device (BHJ-OPVs).

Aiming to probe the molecular level correlations between conjugated polymer architecture, morphology and optoelectronic properties, single molecule spectroscopy (SMS) and single particle spectroscopy (SPS) were employed. The molecular level folding properties of conjugated polymers were studied and correlated to the chemical architecture and rigidness of the polymer backbones by means of SMS and single molecule polarization anisotropy imaging. First, a block copolymer consisting of poly(3-hexylthiophene) (P3HT) and [60]fullerene (C_{60}) was investigated due to its potential for forming active layers in OPV devices that exhibit long-term phase stability and efficient exciton dissociation into free charge carriers. It was demonstrated that the grafting of the C_{60}-containing block does not significantly affect the conformation of the backbone of the P3HT block. Next, a series of thiophene based polymers showing different macroscale crystallization behavior were investigated. The rigidness of the

conjugated polymer backbones was found to be correlated with the chemical architecture of the molecules. However, even the polymers that show no folding in their respective crystals and are thus expected to be the most rigid, still exhibit folding at the single molecule level. From this work it is clear that besides chemical architecture, intermolecular interactions in the crystal structure also need to be considered.

For conjugated polymer materials, in this dissertation specifically the blends of conjugated polymers with fullerenes as found in the active layer of OPVs, the investigation of the molecular level correlations between conjugated polymer architecture, morphology and optoelectronic properties can be prohibitively complex due to the presence of a large number of molecules. Furthermore, in the research presented herein, as well as in the literature, it has been clearly shown that the polymer molecules themselves exhibit severe heterogeneity in their properties (chain morphology, aggregation, optical and electronic properties). Therefore, in order to simplify the structure-property investigations concerning nanodomains in BHJ-OPVs, we developed P3HT/$PC_{60}BM$ ($PC_{60}BM$: [6,6]-phenyl-C_{61}-butyric acid methyl ester) composite nanoparticles (NPs). The size of the nanoparticles corresponds with a few polymer and fullerene domains when considering a similarly sized volume in the active layer of OPVs. Single particle spectroscopy combined with this unique nanoparticle material system reveals variations in molecular conformation and aggregation of the conjugated polymer chains upon doping with different weight percentages of fullerene.

These newly developed NPs were embedded in a hole-injection device to study the exciton-hole polaron interactions and the charge transfer processes at the interface between a hole-transporting layer and the NPs. Pronounced charge trapping was observed for donor-acceptor blend NPs due to the large amount of photogenerated free charge carriers.

Besides fundamental studies on morphology-property relations for thiophene based conjugated polymers, fabrication of BHJ-OPVs based on P3HT and $PC_{60}BM$ was also completed. Low band gap polymer PTB-7 (poly[[4,8-bis[(2-ethylhexyl)oxy]benzo [1,2-b:4,5-b']dithiophene-2,6-diyl][3-fluoro-2-[(2-ethylhexyl)carbonyl]thieno[3,4-b] thiophenediyl]]) and a near-infrared (NIR) small dye molecule were incorporated into active layers of these P3HT/$PC_{60}BM$ BHJ-OPVs to expand the photoresponse of the devices. The effects of doping the P3HT/$PC_{60}BM$ BHJ-OPVs with PTB-7 and NIR dye on the device performance and film morphology were investigated. The doping of PTB-7 can efficiently extend the photoresponse of the resultant devices into the NIR regime and improve the device performance with respect to the reference (undoped) devices, demonstrating an elegant and pragmatic approach in improving light-harvesting efficiency in BHJ-OPVs.

ACKNOWLEDGEMENT

First and foremost, I would like to sincerely thank my research advisor Prof. Andre J. Gesquiere for providing me such a unique opportunity in pursing my PhD research, for his continuous intellectual stimulation, his enormous support and encouragement, and the freedom and patience he offered to me during my PhD study and research. It is my great honor and pleasure to work with him and in his group.

I also would like to offer special thanks to my dissertation committee members including Dr. Saiful I. Khondaker, Dr. Shengli Zou and Dr. Jingdong Ye for their invaluable time and support and helpful discussions and suggestions. I am very grateful to Dr. Yi Liao for providing me with a solar simulator and near-infrared dyes. With many precious discussions with him, I really have learned a lot from him.

I also have to specially thank Dr. Lei Zhai for offering us the block copolymer sample, PBTTT-14 and PQT-12 for single molecule spectroscopy studies. His assistance and advice during my graduate research are greatly appreciated. Dr. Richard D. McCullough at Carnegie Mellon University should be appreciated for providing us PTzQT-12. Sincere thanks also go to Dr. Diego J. Diaz and Dr. Winston V. Schoenfeld for assistance in cyclic-voltammetry experiment and external quantum efficiency measurement in the solar cell research project, respectively.

Special thanks also to Dr. Jianhua Zou, Dr. Jianhua Liu, Dr. Ping Peng, Yuan Chen and Ming Wei for their assistance, cooperation and discussions in my PhD research. My

gratitude also goes to great undergraduates Lauren Simon and Simon Tang for their continuous help with my dissertation research. Thanks to my graduate student colleagues Max Bonner, Mona Matthew and Dr. Daeri Tenery for the friendship, help and encouragement along the way in the past few years. I also thank Arjun Mathur, Kirsten Treglown and Kirsti Baker for the happiness and laughter brought.

Finally, I would like to thank all my family members for their love, encouragement and support over the years. Deepest gratitude goes to my wife, Xiaohong Yu, for being with me through all of this. Without her support, I could never make this finished.

Thank you!

TABLE OF CONTENTS

LIST OF FIGURES

LIST OF TABLES

SUMMARY

This dissertation will consist of seven chapters including the introduction as the first chapter. **Chapter 1** presents the background and significance of investigating morphology and spectroscopy at molecular and nanometer scale of conjugated polymers as well as broadening photoresponse range in polymer based bulk heterojunction organic photovoltaics (BHJ-OPVs). **Chapter 2** describes the instrumentation and methods employed in this dissertation research. First, the custom built Single Molecule Spectroscopy/Single Particle Spectroscopy (SMS/SPS) instrumentation will be discussed, followed by sample preparation methods for SMS/SPS experiments as well as the nanoparticle preparation and characterization methods. Then, the fabrication of hole-injection device based on NPs is presented. At the end, the instrumentation used for solar cell characterization is described, which is followed by the preparation of conjugated polymer solar cells. **Chapter 3** covers the SMS study of a homopolymer poly(3-hexylthiophene) (P3HT) and a block copolymer containing P3HT and [60]fullerene (C_{60}). With single molecule spectra and polarization anisotropy data, the molecular level conformation of these two polymers was probed and compared. It was revealed that the attachment of the C_{60}-containing block can slightly reduce the aggregation of the P3HT block but does not significantly affect the conformation of the backbone of the P3HT block**. Chapter 4** is focusing on the SMS investigation of four thiophene-based polymers having distinct macroscale

crystallization behaviors. These were chosen due to the efficiencies of the OPVs fabricated from these conjugated polymers to be among the highest reported in literature. SMS data clearly reveal differences in the molecular conformation of these polymers as a function of chemical architectures and the rigidness of polymer backbones. In **Chapter 5**, composite nanoparticles (NPs) consisting of P3HT and [6,6]-phenyl-C_{61}-butyric acid methyl ester ($PC_{60}BM$) are developed as a model system for nanodomains generally observed in active layers in polymer/fullerene BHJ-OPVs. The size of these NPs corresponds to only a few of this kind of nanodomains. Various bulk characterization results on pristine P3HT and P3HT/$PC_{60}BM$ composite NPs are demonstrated, followed by detailed investigations by SPS to reveal the variations in polymer structure at the molecular and nanometer level. The key finding is that this material system consists of two crystalline aggregates of different emission energy, which exhibit a variation in their relative abundance with changing $PC_{60}BM$ dopant concentration. To explore the interaction between the excitons and hole polarons as well as the charge trapping at hole-transporting-layer/nanoparticle interface in devices, in **Chapter 6** the NPs are introduced into a hole-only device. The donor-acceptor blend NPs demonstrate distinct charge trapping at the interface caused by the large amount of photogenerated free charge carriers. Besides the fundamental studies on morphology-property relations in conjugated polymers, fabrication of P3HT/$PC_{60}BM$ BHJ-OPVs was also conducted. In **Chapter 7,** the near-infrared (NIR) sensitization of

the P3HT/$PC_{60}BM$ solar cell by using low band gap polymer PTB-7 (poly[[4,8-bis[(2-ethylhexyl)oxy]benzo[1,2-b:4,5-b']dithiophene-2,6-diyl][3-fluoro-2-[(2-ethylhexyl)carbonyl]thieno[3,4-b]thiophenediyl]]) and a NIR absorbing small molecule dye was investigated. It was found that the incorporation of PTB-7 can effectively enhance the photoresponse of the P3HT/$PC_{60}BM$ in the NIR region and improve the device performance with respect to the reference (undoped) devices, suggesting a simple and efficient approach in improving light-harvesting efficiency in BHJ-OPVs.

CHAPTER 1. SIGNIFICANCE AND BACKGROUND

1.1 Significance of Dissertation Research

1.1.1 Single molecule spectroscopy for conjugated polymers applied in organic electronics: a bottom-up approach for understanding conjugated polymer morphology and optoelectronic properties at the molecular level

Since the ground breaking discovery of electrically conducting polymers three decades ago,[1,2] conjugated polymers have attracted an overwhelming research interest due to the combined processability and outstanding mechanical characteristics of polymers, while the ability to readily tailor the electrical, optical and magnetic properties of these functional organic molecules is available.[3,4] In particular, conjugated polymers have been widely used in various applications including organic photovoltaics (OPVs), organic light-emitting diodes (OLED), organic field effect transistors (OFET) and other opto-electronic devices.[5-7] A tremendous amount of experimental and theoretical work has been devoted to the investigation of the structural, electrical, optical properties and their correlations in view of these device applications.[4,8,9]

Structurally, single conjugated polymer chains can be depicted as an ensemble of quasi-independent and localized conjugated segments (i.e. chromophores) due to the presence of bends, kinks, twists or chemical defects of the chain.[10] Typically, a conjugated polymer molecule itself is a highly disordered and complex system, in which each polymer chain finds itself in a unique conformational state. This topology feature leads to various electronic and photophysical interactions between nearby

chromophores on a single polymer chain including energy or charge transfer, ground or excited state aggregate formation.[11] Therefore, the photophysics properties of individual conjugated polymer molecules are governed not only by the weakly-coupled chromophores but also by the interactions between them due to various polymer chain conformations. When it comes to practical applications such as OPVs, OLED or OFETs, these phenomena become more complicated due to the presence of multiple polymer chains, the strongly inhomogeneous morphology and thus optoelectronic properties of conjugated polymer bulk films. This issue is compounded by introducing dopants into this material system, the processing conditions used (e.g. solvent, temperature), specifically the effect thereof on the structural and electronic interactions between polymer molecules in the material.[12] In this circumstance, one can imagine that conventional bulk experiments cannot unveil the structural, electrical, optical properties and their correlations at the molecular or nanometer scale.[10,11,13] In the case of OLEDs for instance, it is intriguing to know whether the electroluminescence observed is general to the ensemble of molecules or just representative of specific sub-ensembles present in the active layer due to possible excitation migration or energy transfer.[10] The device performance of polymer OPVs is directly related to the film morphology,[14] which at its most basic level is a function of the conformation of individual polymer chains. By studying the photophysical and photochemical properties for single polymer chains, the correlations between molecular-level

morphology, chemical architecture, photophysical and photochemical properties can be accessed.[15] This fundamental investigation is imperative to effectively harness the applicability of conjugated polymers in organic electronics, and in this dissertation specifically OPVs.

In the presented dissertation research, the focus is on the fundamental study of structure-property relationships of individual conjugated polymer chains of several polythiophene conjugated polymers important in organic electronics with the single molecule spectroscopy (SMS) technique. We aim to access information about molecular conformation, photophysical and electronic properties of individual polymer chains by studying individual polymer chains, thereby removing the ensemble averaging effect brought by conventional bulk measurements, in order to correlate these properties with the architecture (chemical structure) of these molecules. This single molecule level insight serves as guidance to efficiently engineer these materials for improved performance in device applications.

1.1.2 Composite conjugated polymer/fullerene nanoparticles as a model system for bulk heterojunction organic photovoltaics: probing morphology-properties relations at nanometer scale

Over the past two decades, OPVs based on solution processed semiconductors, particularly conjugated polymers, have emerged as a unique technology that is complementary to inorganic photovoltaics in the race to renewable energy.[16-18] This

technology is promising because the active layer can be fabricated as a large area on flexible substrates through simple, low-cost, but efficient solution processing techniques such as spin-coating, ink-jet printing and roller-casting.[19,20]

As a consequence of the low dielectric constant of organic materials like conjugated polymers, light irradiation mainly produces strongly bound electron-hole pairs (excitons).[21] To realize exciton dissociation into free charge carriers, the donor-acceptor structure has been proposed, in which the conjugated polymers act as light absorbers and electron donors and fullerenes are widely applied as electron acceptors due to their high electron affinity.[22,23] Furthermore, the most efficient exciton dissociation is achieved in the active layers of conjugated polymer solar cells that consist of an interpenetrating network of the conjugated polymer (as electron donor) and fullerene (as electron acceptor). This device design, which increases the interfacial area between the donor and acceptor, greatly enhances the charge separation efficiency - up to unity in some cases - and has been termed the bulk heterojunction-OPV (BHJ-OPVs).[24,25]

The optoelectronic properties of conjugated polymers are highly dependent on polymer chain morphology and polymer chain interactions.[10,13,26] On the nanometer scale, variations in conjugated polymer chain conformation, packing or aggregation can result in complex heterogeneous materials. Despite of the enhanced charge separation efficiency in BHJ, the intermingling structure between the conjugated polymer and fullerene usually introduces an even more complex and inhomogeneous structure.[12]

Unbalanced charge transport and undesired vertical phase separation have been frequently reported.[14,25,27,28] In addition, different active layer thicknesses as well as various blend ratios of the donor and acceptor have also been proposed and discussed.[17,18] Although much knowledge have been revealed through bulk measurement techniques including current-voltage measurement and charge mobility characterization, bulk measurements for heterogeneous systems like BHJ only provide ensemble-averaged data on the material properties that drive material function. Hence, there are still debates over some fundamental questions including active layer thickness, blend ratio, processing methods, and even device structures for enhanced OPV efficiency.[18,29-31] To get out of this dilemma, *the fundamental understanding concerning the nanometer scale structure-properties relations is imperative.* This can be accomplished by eliminating the ensemble-averaging effect by simplifying the material system analyzed.

In this dissertation research, part of the research effort has been devoted to probe and relate material composition, morphology, optoelectronic properties, and interfacial charge transfer processes at the nanometer scale. To realize this research goal, donor/acceptor composite nanoparticles (NPs) were developed as a simplified model system for the active layers of efficient polymer/fullerene BHJ-OPVs. These NPs lie in between the bulk and single molecules in terms of size, but have the functionality of the bulk material with only a small number of molecules present. The size of the

nanoparticles corresponds with a few polymer and fullerene domains when considering a similarly sized volume in the active layer of OPVs.[32,33] In this context, a domain in the active layer is considered to be a (partially) ordered polymer region surrounded by fullerene regions (or vice versa) in the bulk that are separated from/connected to the next domain by more disordered i.e. randomly organized polymer/fullerene boundaries.[12] The latter are often termed domain boundaries or grain boundaries. By combining the nanoparticle approach with single nanoparticle fluorescence detection one or a few nanodomains as found in the active layer of devices can be address to study structure-function relationships at the nanoscale and molecular level, and to reveal the domain to domain heterogeneity of properties. Furthermore, the NPs were applied in hole-only devices to investigate the interaction between the excitons and injected holes as well as the charge trapping at hole transporting layer/nanoparticle interfaces.

1.1.3 Near-infrared photoresponse sensitization in conjugated polymer/fullerene solar cells

With the introduction of the BHJ structure in polymer based OPVs, this field has witnessed a rapid growth in the past two decades.[19,22,34] Among all material systems, the blend of poly(3-hexylthiophene) (P3HT) and [6,6]-phenyl-C_{61}-butyric acid methyl ester ($PC_{60}BM$) has dominated the polymer photovoltaic cells for more than 5 years. The highest reported power conversion efficiency (PCE) for these BHJ-OPVs is

4-5%.[34,35] Although P3HT is not the ideal donor polymer, the P3HT/$PC_{60}BM$ system has been proven moderately efficient with good device lifetimes, facile cell fabrication and abundant commercial availability. Therefore, there are many ongoing research efforts on this material system.[36] Previous investigations generally indicate that the device performance of P3HT/$PC_{60}BM$ system is limited mainly by two factors: *narrow solar light absorption range and poor control over morphology.*[16] Due to a relatively large band gap of ~ 1.9 eV, P3HT can only capture photons with a wavelength less than 675 nm, i.e. at best 27% of the available solar photons.[18] In addition, even for cells with 4-5% PCE the external quantum efficiency (EQE) is usually less than 60-70% due to various factors including light reflection loss, charge recombination and inefficient charge collection.

One important approach to realize this goal is the fabrication of tandem solar cells using polymers with different energy gaps.[37-39] This approach incorporates at least two solar cells linked in series with different absorption characteristics, thus offering a broader absorption range. Although tandem solar cells appear promising in improving the device performance, two main factors make the design complicated and challenging: a) a perfect balance between the front and back cells in photocurrent is required for optimal performance and b) the attenuation of light that can be absorbed by the back cell due to the presence of the front cell.[40] Currently, the development and application of low band gap (LBG) polymers for BHJ-OPVs is believed to be one of the most

promising strategies in improving device efficiency. These polymers have a better spectral overlap with the solar spectrum, particularly in the NIR region of the solar spectrum. Several LBG polymers were synthesized and employed in OPVs, including PCDTBT (poly[[9-(1-octylnonyl)-9H-carbazole-2,7-diyl]-2,5-thiophenediyl-2,1,3 benzothiadiazole-4,7-diyl-2,5-thiophenediyl]) and PTB-7 (poly[[4,8-bis[(2-ethyl hexyl)oxy]benzo[1,2-b:4,5-b']dithiophene-2,6-diyl][3-fluoro-2-[(2-ethylhexyl)carbon yl]thieno[3,4-b]thiophenediyl]]), which exhibit light absorption up to ~ 700 and ~ 800 nm, respectively.[19,41] Highly efficient OPV devices were fabricated using PCDTBT and PTB-7 in the active layer, and yielded devices with PCE of 6.1% and 7.4%, respectively. Despite of their performance in OPVs, at present these LBG polymers are not easily commercially accessible and are very expensive due to complicated synthetic steps.[42,43] In addition, poor solubility, low charge mobility and reduced absorption in the visible wavelength range are often associated with LBG polymers.[44-46]

In consideration of the structural complications with tandem solar cells and the limited accessibility to LBG polymers, there are still many efforts in optimizing the prototypical P3HT BHJ-OPV.[47-50] Herein, with the purpose of capturing more near-infrared photons in a typical P3HT/$PC_{60}BM$ solar cell, broadband absorbing OPVs were fabricated from P3HT/$PC_{60}BM$ active layers that were directly doped with near-IR absorbing low band gap polymer or dye. In addition, to simplify the device fabrication, a solvent additive was applied in preparing the active layers to optimize the

phase separation while eliminating the necessity of post annealing process of the active layers.

1.2 Background of Dissertation Research

1.2.1 Overview of conjugated polymer-fullerene solar cells

To address the ever increasing global energy demand with a renewable resource while minimizing detrimental effects on the environment, the past few decades have witnessed an upsurge in photovoltaic devices research.[51-56] Organic Photovoltaic Devices (OPV) based on conjugated polymers provide great advantages due to low-cost synthesis of materials and easy processing of thin, large area and flexible plastic films via spin coating or ink-jet printing methods.[16,57] Due to the low dielectric constant of organic semiconductors, light absorption in conjugated polymers generally can only result in coulombically bound electron-hole pairs (excitons) rather than free charge carriers typically generated in inorganic semiconductors.[21] To achieve an efficient exciton separation into charge carriers, Tang seminally proposed a donor-acceptor concept in which photogenerated excitons can be dissociated at the interface between two materials with different electron affinity: the electron donor and the electron acceptor.[23] To make viable devices, two device architectures were developed as shown in Figure 1. 1: the donor-acceptor bilayer and the bulk heterojunction structure (BHJ). The former architecture has been widely adopted in

vacuum deposited molecular solar cells.[23,58] However, the performance of such bilayer devices is strongly limited by the requirement of exciton diffusion to the donor/acceptor interface, the short exciton diffusion length of ~ 10 nm, and optical absorption depths of ~ 100 nm of most organic materials.[16] The BHJ structure can maximize the interfacial area for exciton dissociation while reducing the distances required for the exciton to travel to such an interface via an interpenetrating and bicontinuous network of donor and acceptor phases. The most efficient polymer based OPVs are based on BHJ architecture.[19,41]

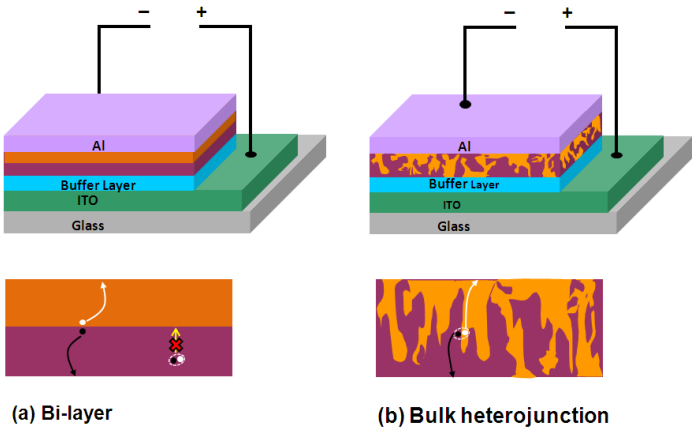

Figure 1. 1 Schematic configurations of typical bilayer (a) and bulk heterojunction (b) organic solar cells. In the bilayer structure (a), the interfacial area between the donor and acceptor is limited. Photogenerated excitons far away from the interface cannot diffuse to the interface and therefore cannot contribute to free charge carrier generation. However, in the bulk heterojunction structure (b), the donor and acceptor molecules are intimately mixed. The resultant bicontinuous interpenetrating network provides a large interfacial area for exciton dissociation.

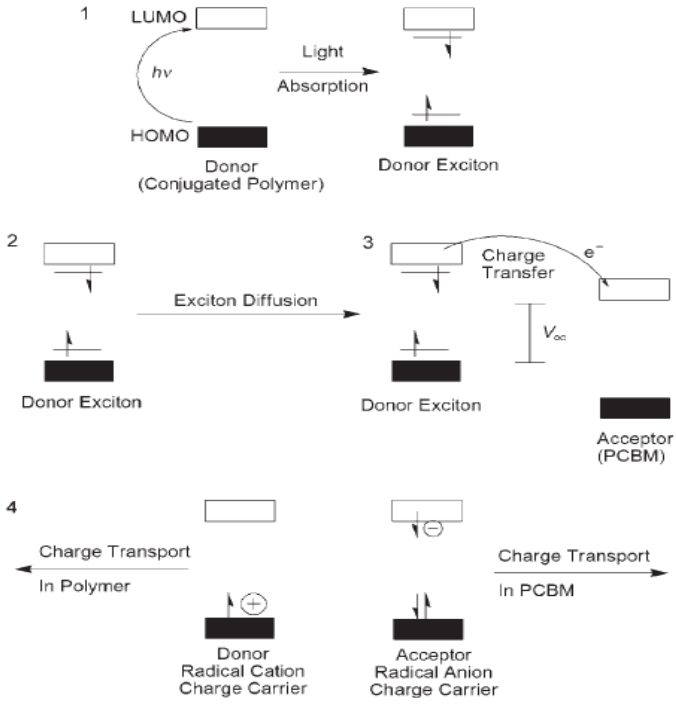

Figure 1. 2 General mechanism of photogeneration of charge carriers in polymer/fullerene solar cell. (Reproduced from reference[20])

Since the discovery of ultrafast photoinduced charge transfer from the conjugated polymer of poly[2-methoxy-5-(2-ethylhexyloxy)-1,4-phenylene-vinylene] (MEH-PPV) to buckminsterfullerene in 1992,[22] conjugated polymer/fullerene solar cells have attracted great attention.[5,19,34] Fullerenes are widely used as the electron acceptors in polymer OPVs because of its high electron affinity relative to many polymers, the ultrafast charge transfer between polymers and fullerenes as well as a very high electron mobility of up to 1 $cm^2/V{\cdot}s$ in FET device.[16] Figure 1. 1(b) depicts a scheme of the typical BHJ conjugated polymer/fullerene solar cells, in which the active layer, i.e., conjugated polymer and fullerene blend film, is sandwiched in between two electrodes with different work functions. Generally, the fundamental mechanism in the energy

conversion process of OPVs involves four steps as shown in Figure 1. 2: (1): light absorption and exciton generation (mainly in conjugated polymer); (2): exciton diffusion to the interface between donor and acceptor; (3): exciton dissociation into free charge carriers at the interface; and (4) charge transport and collection via bicontinuous networks of donor and acceptor to the electrodes.[16] Over the past decade, the device power conversion efficiency has been greatly increased: from 2.5% using poly-(2-methoxy-5-(3'-7'-dimethyloctyloxy)-1,4-phenylenevinylene) (MDMO-PPV) /$PC_{60}BM$ to 5% for the most prominent and extensively studied P3HT/$PC_{60}BM$ system in recent years. To capture more sunlight and achieve better device performance, many promising low band gap (LBG) polymers have also been developed.[19,24,39,43,59] Among these polymers, using bensodithiophene polymer poly[[4,8-bis[(2-ethylhexyl)oxy]-benzo-[1,2-b:4,5-b']dithiophene-2,6-diyl][3-fluoro-2-[(2-ethylhexyl)carbonyl]thieno[3 ,4-b]thiophenediyl]] (PTB-7), Liang and coworkers reported the highest published PCE of 7.4%.[19] Even more encouragingly, in December 2010, Konarka Technologies Inc announced a new world record of 8.3% PCE for a single junction polymer based OPV device with a surface area of 1 cm^2, certificated by the National Energy Renewable Laboratory (NREL).[60] This new record is approaching the 10-11% efficiency mark, which is believed to be the threshold for widespread commercialization of the conjugated polymer solar cell technology.[16,61]

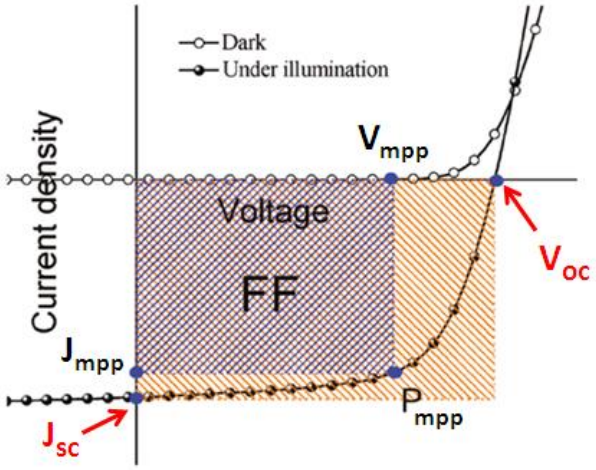

Figure 1. 3 Typical current-voltage characteristic of a solar cell under dark (unfilled circle) and illumination (filled circle). V_{oc} and J_{sc} represent open circuit voltage and short circuit current density, respectively. V_{mpp} and J_{mpp} are voltage and current density, respectively, at the maximum power point (P_{mpp}). (Adapted from reference[62])

In order to determine the efficiency of a solar cell, current-voltage curves as presented in Figure 1. 3, tested under both dark and light illumination, are a common way to characterize device properties. Several important parameters are listed below.

Open circuit voltage (V_{oc}): the voltage across the device under sunlight when there is no current flow. It is the maximum voltage across the cell.

Short circuit current (J_{sc}): the current flows through the device normalized by the device area under sunlight when there is no additional resistance (i.e. no load on the device). It is the maximum current that the cell can produce.

Fill factor (FF): the ratio of the actual maximum power output to the product of V_{oc} and J_{sc}, i.e., the theoretical maximum output if both voltage and current are at maximum values as shown in Equation 1.1:

$$F = \frac{V_{mpp}J_{mpp}}{V_{oc}J_{sc}} \quad (1.1)$$

where V_{mpp} and J_{mpp} are the voltage and current, respectively, at the actual maximum power output point.

External quantum efficiency (EQE): also referred to as the incident photon conversion efficiency (IPCE) refers to the ratio of the number of photogenerated electrons collected at the electrode to the number of incident photons impinging on the device. I can be calculated via Equation 1.2.

$$EQE = \frac{J_{sc}/q}{P_{in}/h\gamma} \quad (1.2)$$

From EQE, the J_{sc} under AM1.5G illumination can be calculated by convolution with the power density of the solar spectrum (P_{in}) using Equation 1.3.[63]

$$J_{sc} = \frac{q}{hc}\int_{\lambda 1}^{\lambda 2} EQE \cdot P_{in}(\lambda) \cdot \lambda \cdot d\lambda \quad (1.3)$$

Here, q is the elementary charge (1.6×10^{-19} C), h the Planck's constant (6.626×10^{-34}J·S), c the constant of speed of light, $P_{in}(\lambda)$ the solar irradiance as a function of wavelength.

Power conversion efficiency (η, PCE): the ratio of actual maximum power output (P_{mpp}) of the cell to power incident on the device can be estimated through Equation 1.4.

$$\eta = \frac{P_{mpp}}{P_{in}} = \frac{V_{oc}J_{sc}FF}{P_{in}} \quad (1.4)$$

P_{in} defines the power integrated over all the wavelengths, which is fixed at 100 mW/cm^2 under Air Mass 1.5G 1 sun standard characterization conditions.

1.2.2 Single Molecule Spectroscopy: an efficient approach in addressing heterogeneous optoelectronic properties of conjugated polymer molecules

A conjugated polymer is generally composed of a linear framework of alternating single and double bonds between carbon atoms of the polymeric chain, which can support the spatially delocalized π-electrons resulting from the neighboring overlapped p_z-orbitals. However, in conjugated polymers, the π-electrons cannot be spatially delocalized over the entire polymer chain due to the presence of bends, kinks or chemical effects in the polymer backbone, resulting in the formation of quasi-independent conjugated segments behaving as chromophores.[11] The entire polymer chain therefore can be depicted as a chain with optically and electronically distinct chromophores as schematically depicted in Figure 1. 4(a).[10] The strong coupling interaction between chromophores results in a strong dependence of the spectroscopy and photophysics on the polymer chain morphology. Figure 1. 4(b) depicts the absorption and fluorescence emission spectra of a solution of the prototypical conjugated polymer MEH-PPV. The broad unstructured absorption is characteristic of all chromophores on the polymer chain being illuminated. In contrast, the fluorescence spectrum is rather narrow and vibronically structured, which has been assumed to arise from emission originating from a small subset of the lowest energy chromophores. In other words, there is an efficient energy transfer, probably by Förster mechanism, in the polymer chain.[10,13] This assertion was supported by time-resolved fluorescence spectroscopy experiments performed for different conjugated polymers:

gradually red shifted emission spectra within the first few picoseconds and loss in fluorescence polarization memory.[64-66] Conventional bulk experiments can yield valuable ensemble averages of the properties of interest; however, it washes out many informative and important photophysical details at the molecular scale in the highly heterogeneous and complex nanostructured conjugated polymer materials. For instance, some concerns that can be raised are listed below:

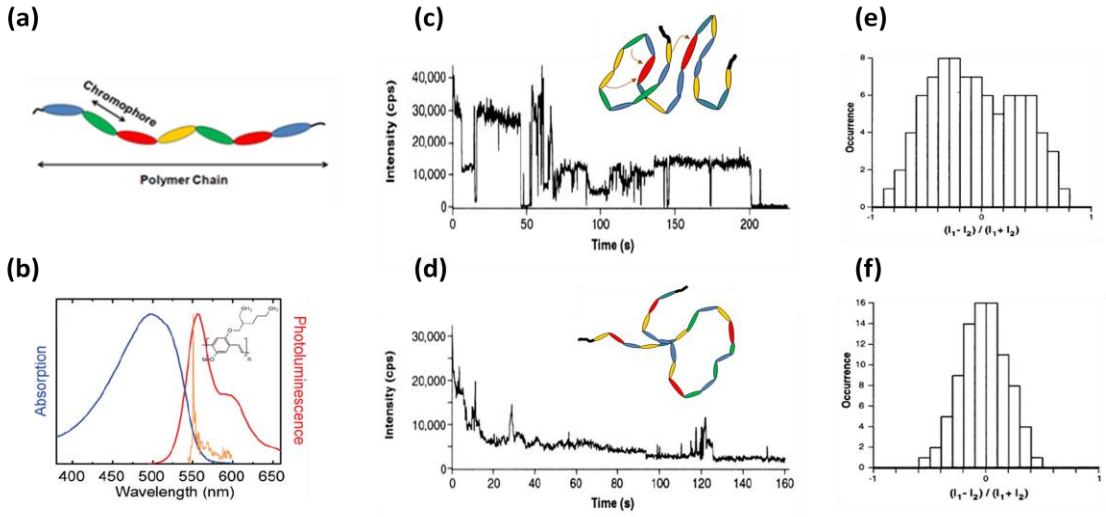

Figure 1. 4 (a) A cartoon for a polymer chain consisting of chromophores lined together. (b) Ensemble fluorescence emission spectra of MEH-PPV dispersed in a polystyrene matrix at room temperature (red line) and at 5 K (pin line). The absorption spectrum (blue line) and the structure of MEH-PPV (inset) are also shown. (c) Typical defect-cylinder conformation for MEH-PPV polymer chain in bad solvents (e.g. toluene) and the fluorescence intensity transients exhibiting intermittency. In this conformation, efficient intrachain energy transfer occurs due to close contact between chromophores. The corresponding emission polarization anisotropy distribution histogram for single molecules is shown in (e). (d) Typical random coil conformation for MEH-PPV polymer chain in good solvents (e.g. chloroform) and the fluorescence intensity transients showing an exponential decrease. The corresponding emission polarization anisotropy distribution histogram for single molecules is displayed in (f). (Adapted from reference[10,67])

1) Is there energy transfer between different chromophores within an individual polymer chain?

2) How does polymer chain conformation affect the photophysics of the individual optically active units and the whole molecule?

3) What is the intrinsic linewidth of absorption and emission spectra of a single polymer chain?

4) What is the polymer chain conformation at single molecule level?

……

To answer these questions and thus effectively harness the potential of conjugated polymers for applications in optoelectronic devices, a fundamental understanding on the molecular or nanometer level scale morphology, electronic, photophysical and chemical properties as well as their correlations is of great importance.

With improvements in low-level light detection technique in the past decade single molecule/particle spectroscopy (SMS/SPS) has become a unique approach in unraveling many amazing photochemical and photophysical observations for fluorescent conjugated polymer molecules.[10,11,13] The first SMS investigation of a conjugated polymer with over 1000 chromophores, (MEH-PPV) by Barbara and coworkers, led to the observation of fluorescence intermittency, i.e. milliseconds fluorescence fluctuation between on and off states, and discrete fluorescence emission levels.[68] These astonishing quantum observations, usually observed in a single

chromophore system, indicate that in a single polymer chain there is a strong interaction between chromophores along the polymer chain and an effective excitation migration to photogenerated quencher sites. These quenchers were revealed to be resulting from photoreaction between exciton traps and oxygen.[69] Later on, this quenching process was found to be reversible by Gesquiere et al through the Fluorescence-Voltage/Single Molecule Spectroscopy (F-V/SMS) technique.[70] A strong dependence of fluorescence spectra of single MEH-PPV polymer chains on its conformation in toluene (a poor solvent) and chloroform (a good solvent) was reported by Huser et al, and is demonstrated in Figure 1. 4.[67,71] In MEH-PPV/toluene samples, the polymer molecules take a tightly folded conformation; therefore multichromophoric polymer chains behave as a single chromophore in photophysics as demonstrated by the intermittency in fluorescence intensity transient due to a very efficient three-dimensional exciton funneling to lowest energy sites (Figure 1. 4(c)). The corresponding polarization ratio histogram is shown in Figure 1. 4(e), in which the high value and broad distribution of polarization ratios indicates a well-defined emission dipole moment. In contrast, for MEH-PPV/chloroform chains, the polymer chains are extended and the fluorescence intensity decays continuously as the conjugated segments bleach one by one, indicative of multichromophoric fluorescence behavior (i.e. there is little interaction between the segments in an extended chain) (Figure 1. 4(d)). This is supported by the Gaussian distribution around 0 of the

polarization anisotropy shown in Figure 1. 4(f), implying a random emission resulted from multichromophoric emission.

Yu et al studied the individual MEH-PPV molecules dispersed in poly(methyl methacrylate) (PMMA) matrix at low temperature (20 K) to resolve emission from different chromophores.[72] It was found that the narrow bandwidth fluorescence spectrum at low temperature shows the distinction between different types of chromophores in the spectrum compared to the room-temperature spectra. Two types of single molecule spectra were obtained at low temperature and they were assigned as either a single-chromophore type (Figure 1. 5(a)) or a multi-chromophore type (Figure 1. 5(b)). The low-energy chromophores ("red" sites) are believed to be due to intramolecular conjugated chain contacts or long conjugated segments, which cause a local lowering of the exciton energy.[13,73,74] The histogram of low-temperature spectra clearly shows a bimodal distribution of the chromophores with low and high energies sites, i.e. "red" and "blue" sites, respectively. Two distinct conformations have been predicted from computer simulation which involve defect coil and defect cylinder as exemplified in the left of Figure 1. 5.[75] The defect coil conformation is an extended structure with rod-like conjugated segments connected by defects. In contrast, the defect cylinder involves a collapsed, ordered and compact structure. Each of these conformations when considered separately still exhibits slight variations in the peak emission energies due to differences between individual molecules in the extent of

intrachain stacking both for the extended and "aggregated" (compact) conformations.[69,72]

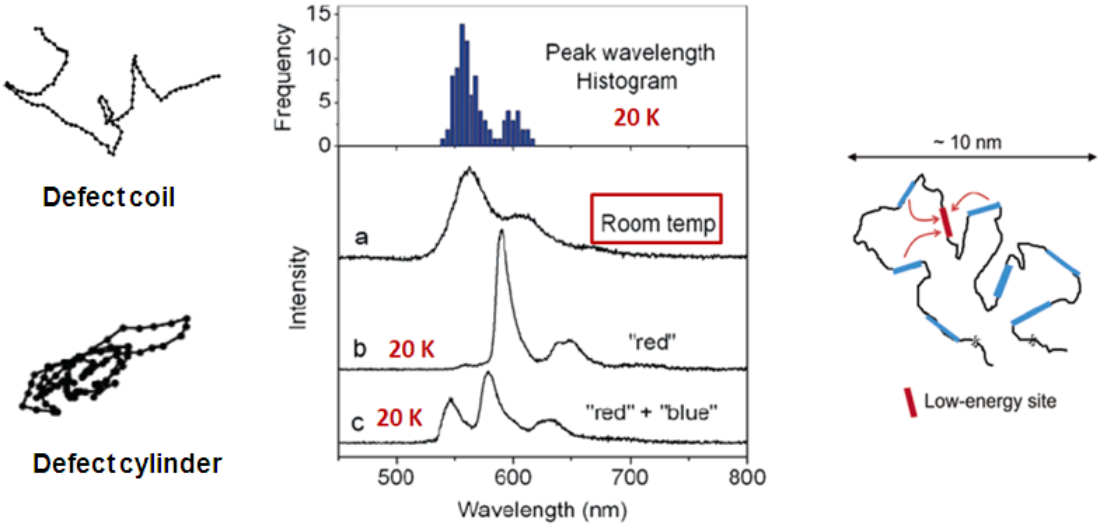

Figure 1. 5 (a) MEH-PPV single molecule spectra at room temperature of 300 K. (b) and (c) are emission spectra of a single chromophore and a multi-chromophore, respectively, at 20 K. The top panel shows the statistical distribution of the "red" and "blue" sites at low temperature. The typical defect coil and defect cylinder conformations generated by computer simulation for MEH-PPV single molecule are given in the left. The right figure illustrates the intramolecular energy funneling from high energy sites to the "red" site in the defect cylinder conformation. (Adapted from reference[13,72,75])

To directly probe the conformation of individual polymer chain and thus correlate the structure-optoelectronic properties relationship has been of great importance in polymer nanoscience and nanotechnology.[11] In the case of fluorescent conjugated polymers, the conformation of a chain can be related to the fluorescence polarization. Using single molecule polarization spectroscopy and computer simulation, Hu et al measured a statistical ensemble of individual polymer chains, probing a

two-dimensional projection of the three-dimension anisotropy ellipsoid, and the resultant polarization distribution was fitted with Monte-Carlo simulations.[75] A highly ordered, collapsed cylindrical conformation for MEH-PPV single chain was demonstrated,[75] which probably dictates the observed efficient exciton funneling in single polymer chains and significant local anisotropy in thin films. With SMS spectra, polarization and photobleaching dynamics data, Huser et al showed clear correlations between MEH-PPV polymer chain conformation and fluorescence features for samples spun cast from different solvents as shown in Figure 1. 4. By taking a similar approach, Sugimoto et al also studied a graft copolymer consisting of a polythiophene backbone and long polystyrene (PS) branches (Figure 1. 6).[15] The researchers found that at the single molecule level the presence of the PS branch leads to a more extended conformation of the polythiophene backbone compared to the collapsed globule-like conformation of the polythiophene precursor molecules taken from the synthetic process. Several other optical microscopy techniques have also been applied in analyzing the polymer chain conformations at the single molecule level such as combination of the wide-filed epi-illumination microscopy and total-internal reflection microscopy,[11,76,77] and defocused wide-field imaging.[78,79] More detailed information about these techniques can be found in recent references.[11,77-80]

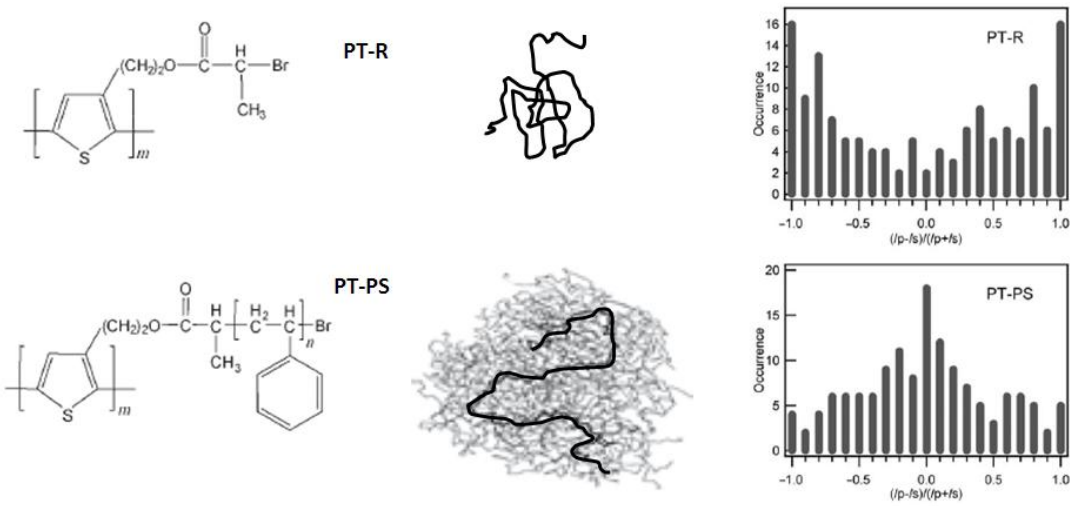

Figure 1. 6 Comparison between the polarization anisotropy (left) between polythiophene without and with the graft of polystyrene (right). The middle cartoons display the conformation for these two polymers. (Adapted from references[11,15])

1.2.3 Heterogeneous and complex morphology of conjugated polymer/fullerene blend active layers in OPVs

For polymer/fullerene based BHJ-OPVs, the investigation concerning the morphology-performance relationship has attracted great research endeavors. As one can imagine, the blended film morphology is even more complicated compared to the already heterogeneous morphology of conjugated polymer films. Dating back to the MDMO-PPV/$PC_{60}BM$ solar cell device, SEM imaging was conducted by Hoppe et al on cross-sections of these films as illustrated in Figure 1. 7 to probe the morphological details in this material system.[81] For films spin cast from toluene, the $PC_{60}BM$ cluster size goes up to more than 0.5 μm when the $PC_{60}BM$ content increases. However, in chlorobenzene cast films, nanospheres with a size of 20 nm were found for all the films even at a high $PC_{60}BM$ concentration. The much smoother surface and smaller clusters in the film cast from chlorobenzene have been attributed to the better mixing of

polymer and fullerene in chlorobenzene. The finer nanoscale phase separation observed in chlorobenzene film yielded a more efficient BHJ device with a PCE of. 2.5% for MDMO-PPV:$PC_{60}BM$ at a weight ratio of 1:4.

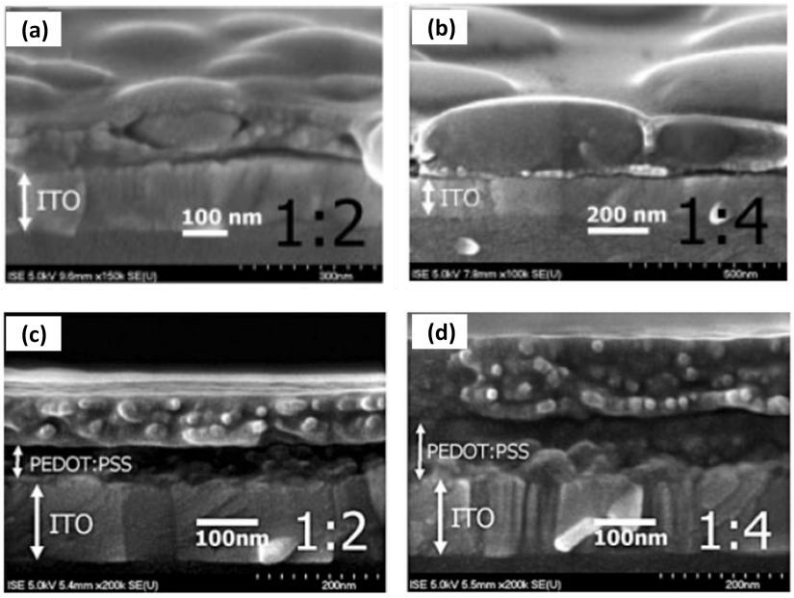

Figure 1. 7 SEM imaging for the cross-section of MDMO-PPV:$PC_{60}BM$ films with different weight ratios spin coated from toluene (a-b) and chlorobenzene (c-d), respectively. (Adapted from reference[81])

Microscopic heterogeneity was not only observed in morphology but also in photocurrent. Groves and coworkers investigated the photocurrent collection for the same materials system with photoconductive AFM (pcAFM).[82] Figure 1. 8(a-c) presents the AFM topography, spatially resolved photocurrent image under 532 nm laser irradiation, and corresponding current-voltage curves collected in different positions on a MDMO-PPV:$PC_{60}BM$ film spun cast from xylene. Analogous to the

AFM topography, the photocurrent map taken on the same area also exhibits nanoscale heterogeneity, with the photocurrent varying by more than one order of magnitude over the detected area. Although the photocurrent features are related to the $PC_{60}BM$ clusters, not all the clusters affect the photocurrent collection in the same way. For example, for the positions marked with square and triangle, despite of similar topographical features, the short circuit photocurrent signal is different by a factor of three, which has been ascribed to the vertical morphology as seen in Figure 1. 7.

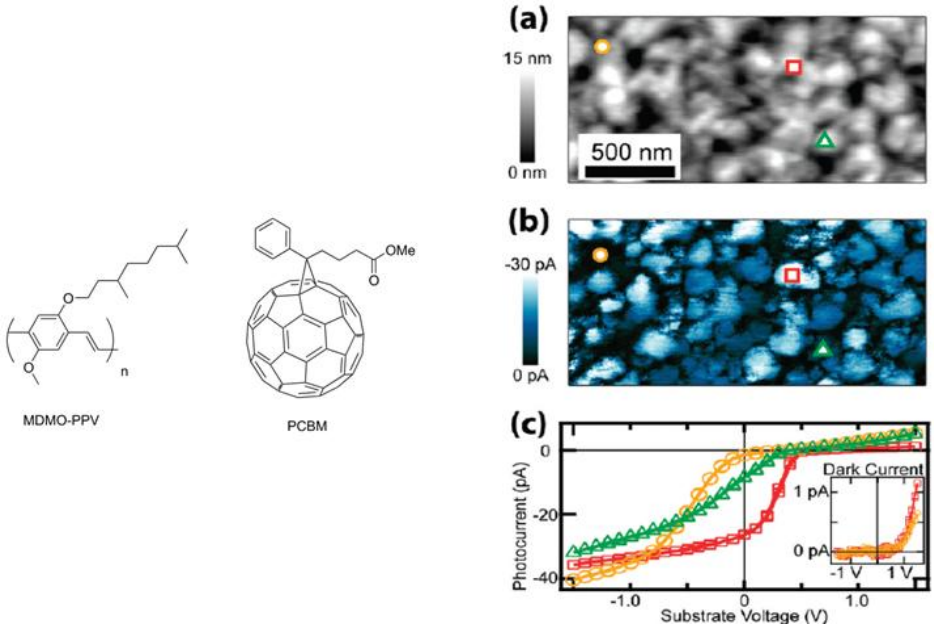

Figure 1. 8 (a) AFM topography for a MDMO-PPV:$PC_{60}BM$ (1:4) blend film spin coated from xylene. (b) Photocurrent imaging taken for the same area as in (a). (c) displays the current-voltage curves collected for the positions marked in (a) and (b). (Reproduced from reference[82])

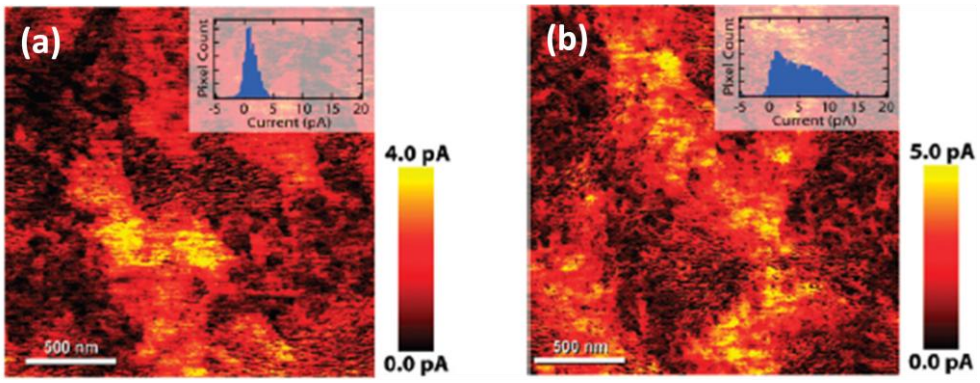

Figure 1. 9 Photocurrent images for P3HT/$PC_{60}BM$ (1:1) film before (a) and after annealing at 110 °C for 2 min (b). The insets in each image give the photocurrent distribution histograms. (Adapted from reference[83])

Figure 1. 9 presents two pcAFM images for P3HT/$PC_{60}BM$ film before (a) and after (b) thermal annealing, in which the photocurrent histograms are shown as insets. It can be observed that after thermal annealing, the heterogeneity in photocurrent distribution is increased, indicative of the complex nanometer level morphology in these solar cells. Dante et al using high resolution AFM probed the surface and internal morphology of P3HT/$PC_{60}BM$ film as shown in Figure 1. 10.[33] As can be observed, both the surface and the internal structures exhibit nanometer scale domains ranging from ~ 10 nm for the surface to ~ 5 nm for the internal part of the film. In polymer/fullerene solar cells, the size of the domains should be sufficiently small to facilitate exciton diffusion to the interface and subsequent dissociation into free charges. On the other hand, sufficient spatial separation of the electron and hole transporting networks is also required to reduce charge recombination. Therefore, reaching such a balanced phase separation inside the active layer is critical for the

optimization of charge generation, transport and device performance.

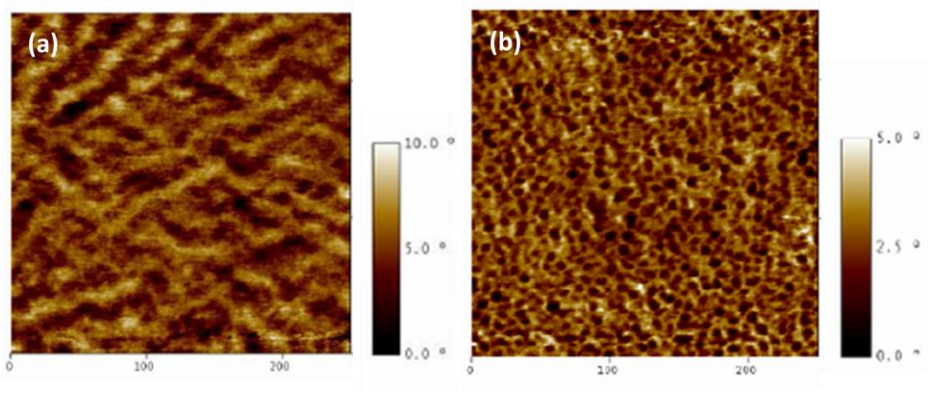

Figure 1. 10 AFM phase images of the (a) surface and (b) cross-section of a P3HT/$PC_{60}BM$ film. The imaging range is 250 nm × 250 nm. (Adapted from reference[33])

To study the relations between surface topography and local spectral properties Nguyen et al, using near-field scanning optical microscope (NSOM), investigated the topographic features and spatially resolved photoluminescence (SRPL) for MEH-PPV films spin-cast from chlorobenzene (CB) solution.[84] Figure 1. 11 (right) shows an image with predominantly flat topography with small features that are a few hundred nanometers in diameter and 10 nm high. The SRPL spectra (Figure 1. 11, left) collected on two different positions, on top of one of the bumps for position 1 and on the flat region for position 2, clearly display distinctly different emission spectra despite the fact that these two locations are only 1 μm apart. Generally, the researchers found that the SRPL spectra collected from the flat region resemble those of polymer CB solutions, while the spectra taken for the bumps exhibit a relative increase near 620

nm and a weak red tail, which were assigned to interchain interactions in the bumps, specifically aggregation leading to the formation of low energy chromophores on single chains and shared excitations between chains. Complicating matters further, the investigators discovered that some areas in the flat regions can also exhibit emission spectra with enhancement of the red part of the spectrum, due to interchain aggregation. This finding further demonstrates the morphological complexity of conjugated polymer materials.

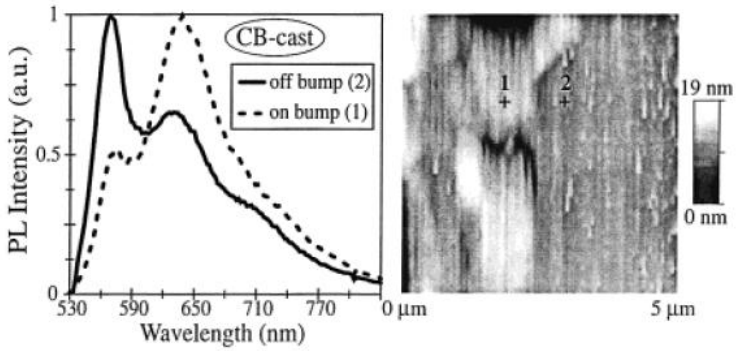

Figure 1. 11 Near-field scanning optical microscope (NSOM) topography image (right) and spatial resolved photoluminescence (SRPL) spectra collected on different positions of the MEH-PPV film cast from chlorobenzene solution. The scan range is 5 × 5 μm^2. (Reproduced from reference[84])

1.2.4 Light-harvesting in P3HT/PC_{60}BM solar cells

Due to the large band gap and narrow absorption bandwidth of many prototypical conjugated polymers only a fraction of the solar spectrum can be absorbed. As shown in Figure 1. 12, in the P3HT/PC_{61}BM system the absorption of light by P3HT primarily occurs in the range of 450-650 nm, and thus only ~ 25% of the solar radiation can be

absorbed.[85,86] In contrast, crystalline Si solar cells (band gap of ~1.1 eV) absorb light from 300 nm up to 1100 nm i.e. almost 77% of the solar radiation on earth. It has been estimated that expanding the absorption band of organic light absorbers from 350 to 900 nm would capture 46% solar radiation, therefore doubling the power conversion efficiency in ideal cases.[85]

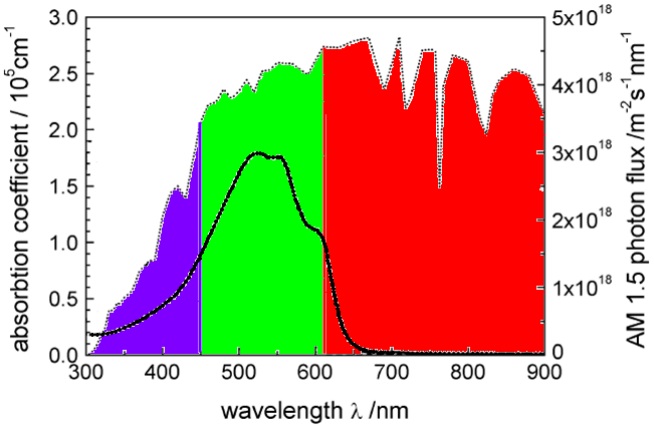

Figure 1. 12 Solar spectrum of sunlight at the earth's surface (dotted curve, AM 1.5 G). The black curve shows a typical absorption profile of P3HT film. (Adapted from reference[87])

Nowadays, the development of LBG polymers has been a common strategy to expand the spectral breadth of absorption. Some very efficient LBG polymers were synthesized and applied in OPVs including PCPDTBT (poly[2,6-(4,4-bis-(2-ethylhexyl)-4H-cyclopenta[2,1-b;3,4-b']dithiophene-alt-4,7-(2,1,3-benzothiadiazole), PCDTBT (poly [[9-(1-octylnonyl)-9H-carbazole-2,7-diyl]-2,5-thiophenediyl-2,1,3-benzothiadiazole-4 ,7-diyl-2,5-thiophenediyl]) and PTB-7.[19,41,88,89] Although these polymers are very

attractive the synthetic steps of these polymers are very complicated compared to the synthesis of P3HT, which makes them very expensive and not easily commercially available at present. For example, for the PTB series polymers, at the time of writing these are only available from one company with a price more than 15 times higher than the widely commercially available P3HT. Furthermore, many LBG polymers usually sacrifice some absorption in the visible region in order to extend the absorption range into the long wavelength regime.[44-46] Finally, several LBG polymers actually yield lower PCE compared with P3HT/$PC_{60}BM$. Take for example the LBG polymer poly({2,6-(4,4-bis(2-ethylhexyl)-4H-cylopenta[2,1-b;3,4-b']dithiophene}-alt-{4,7-(2, 1,3-benzothiadiazole)}), with a band gap of 1.45 eV. OPV devices based on this polymer (in a 1:1 blend with $PC_{61}BM$) show an open-circuit voltage (V_{oc}) of 0.65 eV, a peak external quantum efficiency (EQE) of about 30%, photocurrent response at nearly 900 nm but only a power efficiency of 2.7%.[44] The low PCE has been attributed to the low charge mobility in the active layer. In fact, it has been shown that the development of polymers only having a low band gap is not sufficient for effective light harvesting and improved efficiency.[20] A common and concomitant adverse effect in low band gap polymers pertains to low V_{oc}, which is in part determined by the energy difference between the HOMO of the polymer and LUMO of the acceptor in OPV device.[57]

Tandem solar cells using polymers with different energy gaps represent another alternative in achieving wide absorption range.[37-39,90] This approach incorporates at

least two solar cells linked in series with different absorption characteristics, thus offering a broader absorption range. An added advantage is that in such architecture V_{oc} is increased to the sum of the individual cells. In comparison with a PCE of 5% typically reported for single layer devices of P3HT/PC61BM, Kim et al have demonstrated PCE up to 6.5% in tandem solar cells of P3HT/PC_{70}BM (PC_{70}BM: [6,6]-phenyl C_{70}-butyric acid methyl ester) and PCPDTBT/PC_{60}BM.[39] Although tandem solar cells appear promising in improving the device performance, two main factors make the design complicated and challenging: a) a perfect balance between the front and back cells in photocurrent and b) the attenuation of light that can be absorbed by the back cell due to the presence of the front cell.[40]

With respect to the previous two methods in broadening the cell absorption range, there is a much simpler and versatile approach which involves a direct physically doping into the polymer/fullerene layer of absorbers with a complementary absorption range. To realized effective doping, the dopant must meet the following basic criteria: (1) the energy level of the dopant should lie intermediately to those of the polymer and fullerene; (2) the absorption coefficient of the dopant in the complementary range should be higher relative to the polymer and fullerene blend and (3) the dopant can either act as an electron donor and hole transporter or operate as an electron acceptor and transporter.[91] Recently, researchers have shown successful doping using either dyes or low band polymers with longer wavelength absorption region.

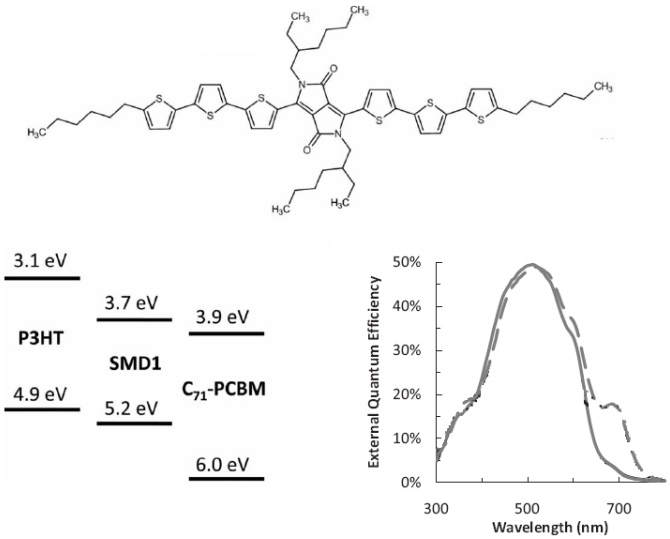

Figure 1. 13 Small molecule absorber structure and its energy levels with those of the polymer and fullerene. The EQE data is also included to show the photocurrent contribution of the dopant in the longer wavelength regime [solid line: reference cell of P3HT/P_{70}BM (10:10 mg/ml); dashed line: small molecule doped P3HT: P_{70}BM cell (10:10:2 mg/ml for P3HT: P_{70}BM:dopant). (Adapted from reference[47])

Peet et al demonstrated a photocurrent increase in P3HT/PC_{70}BM cell with doping a small molecule sensitizer for near-infrared (NIR) absorption.[47] Figure 1. 13 shows the small molecule structure and corresponding energy levels with P3HT and PC_{70}BM. From the EQE spectrum, direct photocurrent contribution from the dopant in the range of 650-750 nm can be clearly identified. Similar improvement of light-harvesting efficiency by introducing a phthalocyanine derivative (Figure 1. 14(a)) has been reported by Honda and coworkers.[92] Interestingly, the authors found that the introduction of silicon phthalocyanine (SiPc) can not only directly yield photocurrent output at the absorption wavelengths of SiPc but indirectly enhance charge separation from P3HT excitons through energy transfer from P3HT to SiPc molecules located at

the P3HT/$PC_{60}BM$ interface (Figure 1. 14(b)). It is estimated that this energy transfer rate is more than 100 times faster than the energy migration rate in P3HT, therefore promoting the P3HT exciton diffusion and subsequent dissociation (Figure 1. 14(c)).

Compared to small molecule absorbers doping, LBG polymer doping is more structurally favorable due to the miscibility of conjugated polymers. Despite great efforts and trials in producing single-layer cells with LBG polymer, less attention has been put into developing LBG polymer doped cells. Only recently the NIR sensitization of P3HT/$PC_{60}BM$ cells by the LBG polymer poly[2,1,3-benzothiadiazole-4,7-diyl[4,4-bis(2-ethylhexyl)-4H-cyclopenta[2,1-b:3,4-b']dithiophene-2,6-diyl]] PCPDTBT have been studied by Koppe et al.[48] Basically, the researchers found that in this ternary blend P3HT serves not only as an electron donor to $PC_{60}BM$ and PCPDTBT but also as a hole transporting matrix for PCPDTBT. Detailed analysis of photogenerated charge species via photoinduced absorption experiments revealed that the energy transfer between P3HT and PCPDTBT is negligible, probably due to the competing process of the ultrafast photoinduced electron transfer from the former to the latter.

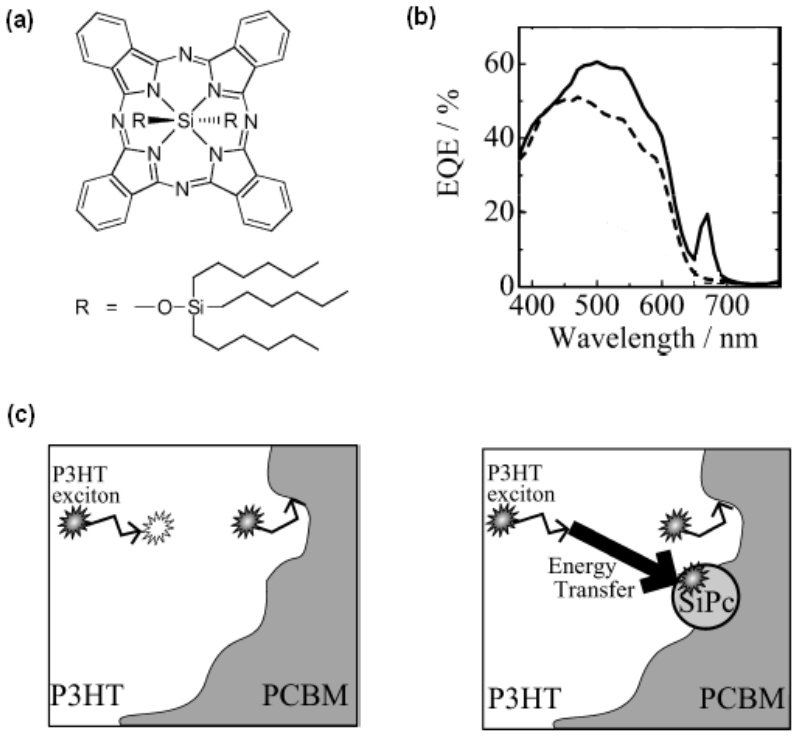

Figure 1. 14 (a) Chemical structure of SiPc. (b) EQE spectra of P3HT/$PC_{60}BM$ cells without (dashed line) and with SiPc. (c) Schematic illustration showing that with the absence of SiPc some P3HT excitons far away from the P3HT/$PC_{60}BM$ interface can not diffuse to the interface and get dissociated (left). In contrast, these excitons with the assistance of the incorporated dye can reach the interface by energy transfer to the SiPc molecule. (Adapted from reference[92])

CHAPTER 2. INSTRUMENTATION AND EXPERIMENTAL

2.1 Single Molecule/Particle Spectroscopy Instrumentation

2.1.1 Introduction

Although molecular information derived using bulk measurement can be valuable for homogeneous systems, it is not for complex and heterogeneous systems due to the ensemble-averaging effect. That is, the distributions of properties on a molecular level for heterogeneous systems can be averaged out and yield only a single parameter. In fact, many materials, chemical and biological systems are really heterogeneous due to e.g. heterogeneity of molecule structure, variations of the local environment at the molecular scale, variations in actual molecular behavior, or randomness in time of cycling through events by molecules in the ensemble.[10,13,93] To understand molecular properties and chemical and physical variations on a single molecular scale, researchers aspire to probe and study individual single molecules.

The study of single-molecule behavior dates back to early 1900s when Einstein conducted his famous work on Brownian motion, which basically confirmed the atomic theory of matter.[94] The invention and advance in late 20th century in scanning tunneling microscopy (STM) and atomic force microscopy (AFM) have allowed the visualization and even manipulation of single atoms and molecules.[95-97] Fluorescence microscopy, in comparison, offers a unique approach for luminescent materials in revealing a wealth of information on structure, photochemistry and photophysics,

chemical interaction, and dynamics of molecular species. *From spectral hole burning and fluorescence line narrowing to near-field and confocal fluorescence microscopy, these advances have allowed not only fluorescence imaging of single molecules with high spatial resolution but also conducting single-molecule spectroscopy at room temperature.* In 1989, the first demonstration of detection of individual molecules by the single molecule spectroscopy technique at low temperature was accomplished by Moerner and Kador.[98,99] Since then, great efforts have been exerted in single molecule detection techniques at room temperature where most materials function and biochemical reactions take place. Figure 2. 1 shows four different spectroscopy techniques developed for studying single molecule fluorescence. Among these techniques, the introduction of a laser confocal scanning microscopy (LCSM) greatly advances this field due to its simplicity and sensitivity, which will be described in the following section.[100]

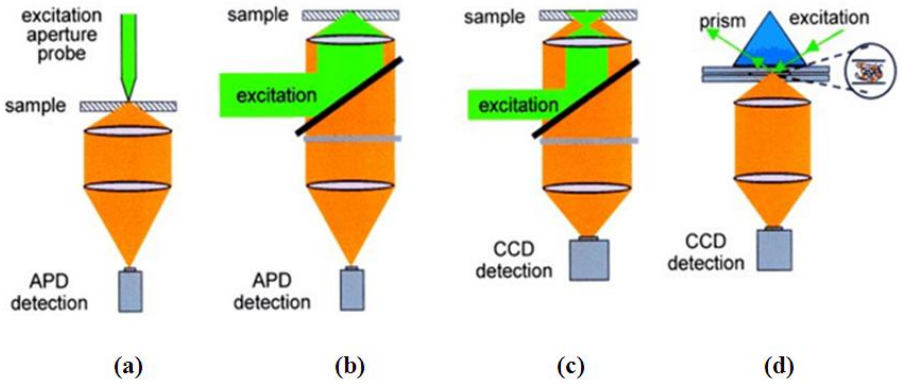

Figure 2. 1 Four different spectroscopy techniques in detecting single molecules (a) near-field optical spectroscopy, (b) laser confocal imaging, (c) wide-field imaging, and (d) total internal reflection imaging. (Reproduced from reference[100])

To probe individual molecules in SMS, two main requirements must be met: (1) *only one molecule is in resonance with the optical wavelength in the probed volume; (2) the signal-to noise ratio (SNR) for the single-molecule signal must be greater than unity in order to overcome contributions from detector noise, including shot noise, and contributions from the background, including scattered excitation light and background fluorescence.*[101] The first requirement can be generally achieved by using extremely diluted concentrations, e.g. 10^{-10} M in our case. With respect to the second prerequisite-to obtain as large a signal as possible, one needs to increase the efficiency of optical detection and reduce background noise. Using high numerical aperture microscope objectives and sensitive detectors such as silicon avalanche photodiodes (APD) or charge-coupled devices (CCD) in combination with proper filter sets are some of the key considerations besides the quantum yield of the fluorophore. Minimized probe volume can help reduce Raman scattering and reject any scattered radiation at the pumping wavelength. In confocal microscopy, the detection of a single fluorophore in the focal volume can be achieved by focusing the laser beam to a small probe volume of 0.5-1.0 μm^3, which has an approximately cylindrical shape with a diameter of 0.5 μm (diffraction limited) and height of 2 μm (limited by spherical aberration).[102] Meanwhile, for the target molecules, large absorption cross-section, high photo-stability, weak bottle necks into dark states such as triplet

states, operation below saturation of the molecular absorption and a high fluorescence quantum yield of fluorescence are desired. In addition, it is imperative to exclude fluorescent impurities by using ultrapure solvents, host matrix and ultra clean cover slides.

2.1.2 Home-built Sample Laser Confocal Scanning Microscope

Figure 2. 2 shows the home-built laser confocal scanning microscope (LCSM) setup on an optical table. The selected wavelength from an Ar^+-ion laser source (Melles Griot 43 series) is filtered, expanded, collimated and then directed into a commercially available inverted microscope (Zeiss Axiovert 200). The excitation laser is reflected by a dichroic mirror and then focused by an objective lens (Zeiss Fluar 100 ×, NA=1.3, WD=0.17 mm) of the microscope into a small probe volume with diffraction limited spot on the focal plane. The spot radius or the ideal resolution is related to the laser wavelength and numeric aperture through Equation 2.1,

$$D=0.51\lambda/NA \tag{2.1}$$

where λ is the excitation wavelength and NA is the numeric aperture. In reality, for the laser wavelength of 488 nm, the resolution is around 300 nm due to low specimen contrast and improper illumination.[103] After the sample is excited, the fluorescence signal is collected by the same objective lens, filtered and then split onto different types of detectors. Single particle fluorescence spectra were obtained by diverting the fluorescence signal through a spectrograph (PI Acton SP-2156) that is coupled to a

thermoelectrically cooled electron multiplying charged coupled device (CCD) (Andor iXon EM+ DU-897 BI). Each fluorescence spectrum was collected with 10-60 seconds exposure time. Three consecutive exposures were averaged for each molecule or nanoparticle. When the sample is raster scanned across the focused laser beam, a fluorescence image is created simultaneously at the image plane which is located at the the side port of the microscope in our case. The same image is collected with the optics optics of 100X magnification onto an avalanche photodiode (APD, PerkinElmer SPCM-AQR-14).

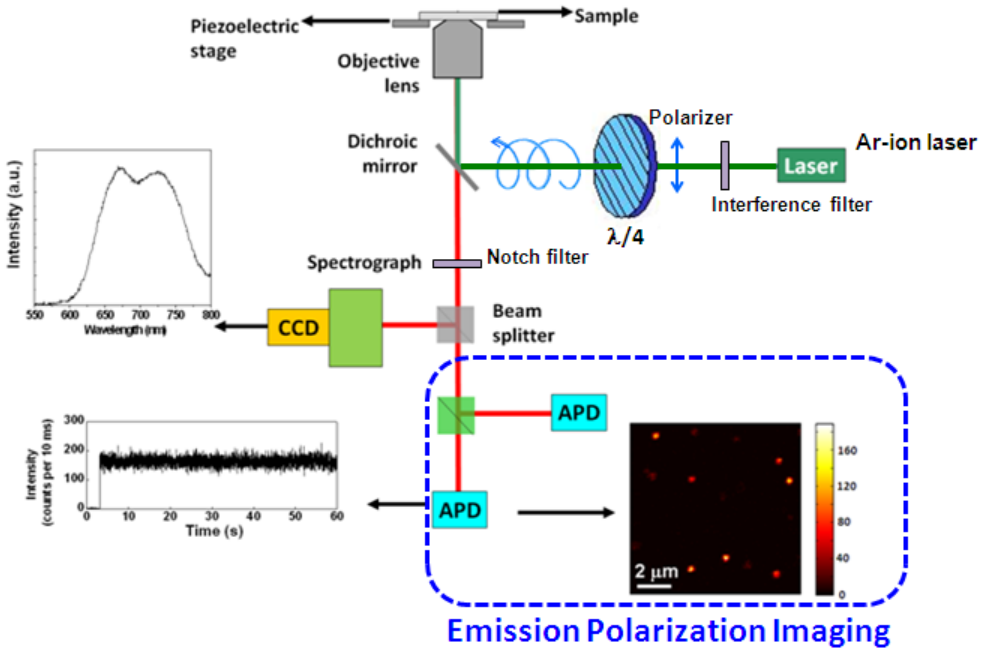

Figure 2. 2 A schematic diagram of the home-built LCSM and detection system. The excitation laser is directed to the objective lens and the emission passes through the dichroic mirror and collected by either CCD or APD detectors. The blue frame encompasses the fluorescence polarization anisotropy imaging set up under circularly polarized laser excitation. Basically, by using a polarizing cube beam splitter, the fluorescence signal is split to two orthogonal directions where fluorescence images were obtained simultaneously with two APD detectors.

2.1.3 Single Molecule Polarization Imaging

For fluorescence polarization measurements, circularly polarized excitation laser light was used through a quarter wave plate (Newport). As shown in Figure 2. 2, the fluorescence signal was split into two orthogonal directions by a broadband polarizing cube beam splitter (Newport, 05FC16PB.3) and detected with avalanche photodiodes (Perkin Elmer SPCM-AQR-14). The G-factor for this setup was determined to be 0.79 using a TransFluoSpheres bead sample (carboxylate-modified microspheres, 0.1 μm, 488/560, Invitrogen) at 488 nm excitation. Reported polarization ratios were calculated calculated using image analysis software home-written in MatLab.

2.2. Single Molecule Spectroscopy Sample Preparation

2.2.1 Materials

Table 2. 1 summarizes the source, number average molecular weight (M_n) and polydispersity (PDI) of six conjugated polymers that we have studied using SMS in this dissertation research. Thermal deposition of an Aluminum protecting layer was performed in a thermal evaporator incorporated in a MBraun N_2 glove box system. Alumina coated Mo boats (ME3-AO-Mo, R.D Mathis) were used for Aluminum deposition and Aluminum canes (99.99%) was bought from CERAC Inc.

Table 2. 1 Summary of conjugated polymers investigated with SMS in this dissertation research. Corresponding structures are shown in Figure 3. 1 and Figure 4. 2. The M_n values were measured with gel permeation chromatography (GPC).

Source	**Dr. Lei Zhai's group**		**BASF**	**Merck**	**Dr. Richard D. McCullough's group**	**American Dye Sources**
Material	P3HT	P3HT-PS-C_{60}	P3HT	PBTTT-14	PTzQT-12	PQT-12
M_n	7,500	15,400	35,700	28,000	18,000	21,000
PDI	1.2	1.6	1.4	1.9	1.9	2.2

2.2.2 SMS Sample Preparation

To have an ultra clean cover slide is a prerequisite in performing SMS experiments. The slides used for SMS/SPS experiments were ultrasonically cleaned sequentially in acetone, 10 wt% sodium hydroxide (NaOH, semiconductor grade, 99.99%, Sigma Aldrich) aqueous solution, and twice in DI H_2O, for 20 min each, and finally stored in fresh DI H_2O. The slide was blow-dried with N_2 and then cleaned in a UV/Ozone cleaning system (T10X10 OES, UVOCS Inc.) for 15 min before use for SMS/SPS sample preparation.

All the studied polythiophene conjugated polymers received are used directly without any purification. The polymer solution in chloroform (OmniSolv, 99.80%, EMD) with a concentration of ~ 0.1 mg/ml was prepared in the ambient atmosphere. To dissolve the polymer fully the polymer solution was heated on top of a hot plate at ~ 100 ℃ for about 30 min and then cooled down to room temperature in 30 min. The polymer

solution was further diluted to a concentration of about 10^{-10} M by a 2 wt% PMMA (M_w: ~ 97,000), secondary standard, Sigma Aldrich) solution in chloroform, and then was spin coated onto a clean cover slide at 2000 rpm for 1 min. The PMMA film with a thickness of ~ 200 nm serves as an inert matrix for dispersed individual molecules of conjugated polymer. The spin coated sample was then immediately transferred in to the thermal evaporator inside the glove box and deposited with ~ 200 nm thick Al film to prevent fast photobleaching during the SMS experiments carried out in the ambient atmosphere.

2.2.3 Molecular Solution Bulk Characterization

UV-Vis absorption

The UV-Vis absorption spectra were collected with a Varian Cary 300 Bio UV-Vis scanning spectrometer using a quartz cuvette with 1 cm path length.

Fluorescence

Fluorescence emission spectra were taken with a NanologTM HoribaJobin Yvon fluorimeter using the same cuvette used in UV-Vis absorption measurements. The excitation wavelength was set at 488 nm.

2.3. Single Particle Spectroscopy Sample Preparation

2.3.1 Materials

P3HT (> 99%, regioregular), $PC_{60}BM$ (> 99.5%), polyvinyl alcohol (PVA, cold water soluble) and anhydrous tetrahydrofuran (THF) (> 99.9%, anhydrous, inhibitor free)

were all from Sigma Aldrich and used directly (see chemical structures in Figure 2. 3). DI H_2O (18 MΩ·cm) at room temperature was obtained from an Milli-Q deionized water purifying system (Barnstead Nanopure Diamond).

2.3.2 SPS Sample Preparation

The nanoparticle suspension was prepared using a reprecipitation method developed by Nakanishi's group.[104,105] Herein, we extend this method to prepare conjugated polymer/fullerene composite nanoparticle suspensions as depicted in Figure 2. 3. Briefly, 1 mg P3HT with 0 mg $PC_{60}BM$ (0 wt% $PC_{60}BM$ doped), 0.05 mg $PC_{60}BM$ (5 wt% doped), 1.0 mg $PC_{60}BM$ (50 wt% doped) and 3mg $PC_{60}BM$ (75 wt% doped), respectively, were dissolved in 10 ml THF at 100 ℃ and then cooled down to room temperature. 1 ml THF solution was injected rapidly to 9 ml deionized water while simultaneously stirring the mixture at ~ 1000 rpm. After injection, the suspension was removed from the magnetic stage and clear pink colored suspensions were obtained. A photograph of one polymer THF solution and nanoparticle suspensions under UV illumination are shown in Figure 2. 3. Since THF can be mixed with water completely, when the hydrophobic polymer molecule in THF solution are injected into water, a high interfacial surface tension between the polymer and water molecules and a strong intrachain hydrophobic attraction in polymer molecule result in supersaturation, nucleation and growth to form NPs. The long term stability of nanoparticle suspension lies in a repulsive electrostatic force between the charged surface of the NPs, which

generally can be predicted according to Coehn's empirical rule.[106] SPS sample preparation consisted of first mixing an appropriately diluted nanoparticle suspension with 4 wt% PVA in DI water. The resulting solution was then spin coated onto a glass cover slide. A 200 nm aluminum or gold film was subsequently deposited on top of the sample to keep oxygen from penetrating the sample.

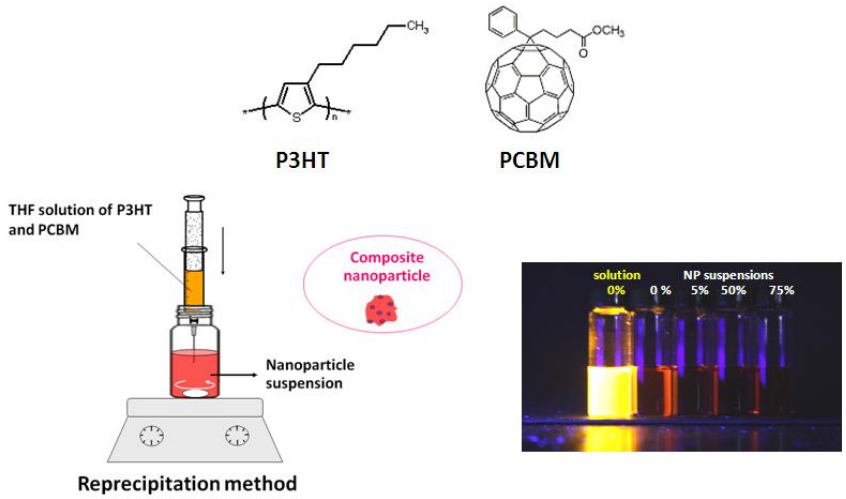

Figure 2. 3 Schematic illustration of the revised reprecipitation method in making composite nanoparticle suspension. The chemical structure of P3HT and $PC_{60}BM$ are shown on top. Basically, the polymer and fullerene were dissolved in a good solvent, i.e., THF, and then a small volume of the blend solution was rapidly injected into a bad solvent, i.e., H_2O. The right photograph was taken under UV irradiation (UVL-21, UVP) for an undoped solution and the composite nanoparticle aqueous suspensions with different $PC_{60}BM$ contents.

2.3.3 Nanoparticle Bulk characterization

Absorption and fluorescence

The bulk absorption and fluorescence spectra were collected using the same

instruments as for the polythiophene molecular solutions.

TEM

The diameter of prepared NPs was characterized by transmission electron microscopy (TEM, JOEL 1011). To prepare TEM samples, one drop (~ 1.5 μl) of a NPs suspension was directly place don a TEM copper grid coated with carbon film (400 mesh, Electron Microscopy Sciences), and dried in vacuum for 15 min.

AFM

The height of the prepared NPs was characterized by an atomic force microscopy (AFM, Digital Instruments Dimension 3100) in tapping mode. The samples were prepared by dropping ~ 6 μl of a nanoparticle suspension - after diluting five times- on clean mica substrates (V-4 grade, SPI Supplies) followed by vacuum drying for 15 min.

2.4. Hole-injection Device for Nanoparticles

2.4.1 Materials

The nanoparticle suspensions prepared in Section 2.3 were used directly for hole-injection device. ITO cover-slides with a sheet resistance of 50 Ω/□ were home-designed and processed by Evaporated Coating, Inc. Before utilization, ITO slides were cleaned sequentially in acetone, 10 wt% NaOH aqueous solution, DI H_2O and finally in UV/Ozone cleaning system. SiO_2 pellets (99.99%) were bought from ACI Alloys and N,N'-bis(3-methylphenyl)-N,N'-diphenylbenzidine (TPD) was from

Sigma Aldrich. Silver paste (325 Part A and B) and UV curing epoxy (3013, 170 ml) were obtained from Dynaloy Inc and Dymax, respectively. Au pellets (99.99%) were bought from CERAC Inc.

2.4.2 Device Fabrication

The hole-injection device used in the fluorescence-voltage/single particle spectroscopy (F-V/SPS) study was assembled bottom up with a metal-insulator-semiconductor geometry as shown in Figure 2. 4 (left). Basically, on top of a clean ITO cover slide, a 200 nm-thick SiO_2 insulating layer was deposited in an electron beam evaporation system (Thermionics). Then, a 100 nm thick PMMA film was spun cast from a 4 wt% toluene (> 99.96%, Sigma Aldrich) solution at 2000 rpm on top of SiO_2 to prevent direct contact between the NPs and the SiO_2 layer, which was suspected to cause instability of NPs.[70] On top of PMMA, a thin layer of 10 nm of polyvinyl alcohol (PVA) was spin-coated from a 0.5 wt% PVA aqueous solution to form a hydrophilic surface favorable for further spin-coating of the aqueous nanoparticle suspension. It should be noted that the PVA film thickness must be less than the height of the NPs so that TPD deposited hereafter can make close contact with the NPs for charge transfer at the interface. After the spin coating of NPs from a 5 times diluted suspension, the device was transferred into a N_2 filled glove box and exposed to the N_2 atmosphere for two days. A TPD layer was then deposited in the thermal evaporator at a rate of 0.5 Å/s with a final thickness of 50 nm. An Au electrode was finally deposited in the thermal

evaporator under high vacuum (<10^{-6} Torr) with a thicknesses of 100 nm. Devices were wired with copper wires (Magnet wire, 28 AWG Insulated, Marvac Electronics) using silver paste inside the N_2 glove box and finally encapsulated with a UV-curing epoxy and a top protective cover slip under UV irradiation to ensure the long term photostability of the NPs.

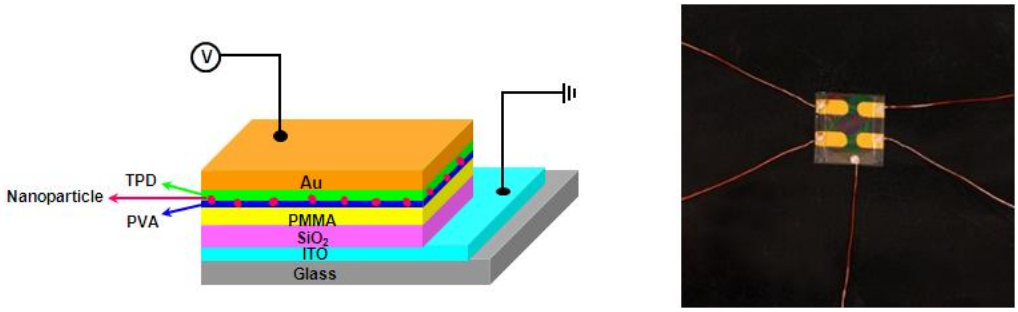

Figure 2. 4 Device structure of nanoparticle based hole-only capacitor device (left) and a laser confocal scanning image (right, 10×10 μm^2) of 50 wt% $PC_{60}BM$ doped P3HT nanoparticles in hole-only capacitor device at zero bias collected under 488 nm excitation from an Ar^+ laser with a power of 7.2 W/cm^2. The scale bar indicates counts per 5 ms.

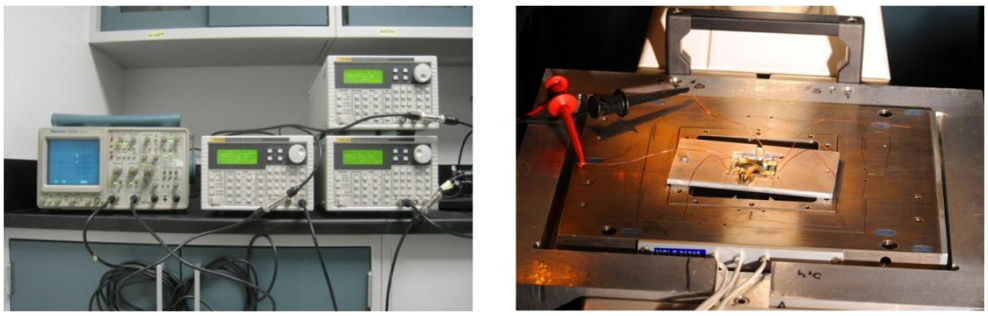

Figure 2. 5 (a) Three wave-function generators are used in obtaining the bias modulation for the device. Basically, one is used to send trigger and gate signals to the other two generators. The trigger then applies bias to the device and the modulated fluorescence was recorded by APD. At meantime, the gate generator generates a reference signal to another APD detector. (b) A hole-injection device placed in LCSM and connected with two terminals from the function generator.

2.4.3 Fluorescence-Voltage/Single Particle Spectroscopy

The F-V/SPS measurement was carried out on a home-built laser confocal scanning microscope (LCSM), which has been described previously in Section 2.1.2. Briefly, the fluorescence image was first collected with LCSM under 488 nm excitation when the sample was raster scanned across the focused laser beam (Figure 2. 4, right). The fluorescence vs. time traces for individual NPs were obtained by positioning a chosen NP into the laser beam and recording the fluorescence transients while under continuously laser excitation, with a power of 0.7 W/cm^2 for the undoped P3HT NPs and 7 W/cm^2 for the 50 wt% $PC_{60}BM$ doped P3HT NPs. Then, the fluorescence-voltage modulation experiment was conducted by applying repeatedly triangular waveform of bias voltage, achieved with a programmable wave function generator (Fluke, Figure 2. 5), while acquiring the single particle fluorescence time transient. The data acquisition was in turn synchronized to the applied bias cycles, allowing for the synchronously averaging of the data as a function of time and bias over many cycles.

2.5. Solar Cell Performance Characterization

The J-V curves of the solar cells were characterized under Air Mass 1.5 Global illumination condition using a Newport Oriel 96000 solar simulator with a 150 W ozone free xenon lamp and a 1.3-inch (33 mm) diameter collimated beam. The

illumination density was calibrated with a standard monocrystalline silicon reference solar cell (Newport, 91150V) with KG-5 visible color filter certificated by NIST (National Institute for Standards and Technology) to the ISO-17025 standard and is traceable to the National Renewable Energy Laboratory (NREL). The current density-voltage (J-V) curves were collected using a Keithley 2635 source measurement unit. The ITO and Aluminum electrodes were connected to the positive and negative terminal, respectively. External quantum efficiency (EQE) data was taken using the QE/IPCE Measurement kit (QE-PV-SI) from Newport. In this characterization system, a 300 W Xe Arc light source is coupled to a CS260 monochromator to create the scanning light. A dual channel Merlin lock-in amplifier with a built-in chopper controller is utilized for the sensitive optical power and current measurements. All the devices were test in air without encapsulation. Note that in this EQE setup the calibration Si detector and the solar cells measured are not in the same position. A rough estimation indicates that the real EQE data should be about 1.5 times higher than the data given in this dissertation.

It has been reported that the device layout has a significant effect on the accuracy of device performance measurements.[107] The nominal device area of a solar cell shown in Figure 2. 6(a) is region I, i.e. the overlapped area of Al and ITO electrodes. Although PEDOT:PSS (Clevios P VP AI 4083) has a very low conductivity (10^{-3} S/cm),[5] investigations indicate that region II in Figure 2. 6(a) has non-negligible photocurrent

output if no mask is used when measuring the device element with nominal device area of region I.[107] Figure 2. 6(b) shows the device layout employed in this dissertation research. To carry out J-V or EQE measurement accurately, a device mask was applied for every device measured. The mask size is 0.33 cm × 0.33 cm, which can effectively remove the influence of the overlap regions between PEDOT:PSS and Al electrode.

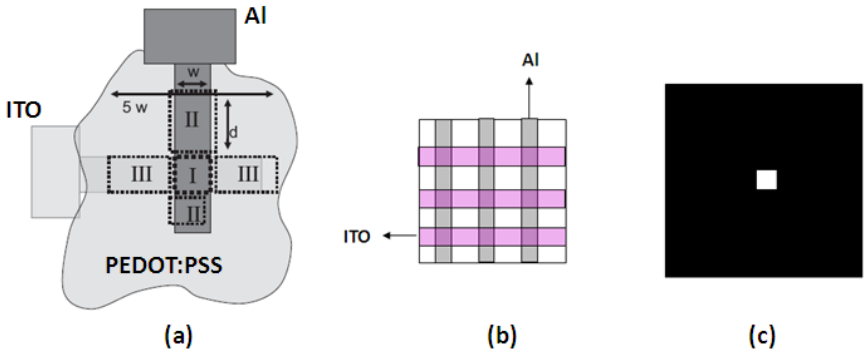

Figure 2. 6 (a) OPV device element with a crossed layout. Region I is usually taken as device area, which is the overlapped region of two electrodes. However, region II contains the overlapping area between PEDOT:PSS, the active layer and Al electrode. Although PEDOT:PSS is not highly conductive, if not masked this region can generate certain amount of photocurrent. Since region III is not covered with Al, it can not contribute to photocurrent when measuring region I without mask. (b) Device layout used in this work. The slide size is 1 inch × 1 inch. ITO strip width is 0.33 cm and effective metal electrode width is about 0.2 cm. (c) Device element mask used in the J-V measurement. (Figure 2. 6(a) is adapted from reference[107])

2.6. Solar Cell Devices Fabrication

2.6.1 Materials

Patterned indium-tin-oxide (ITO) (sheet resistance: 15 Ω/□) coated glass slides were

home-designed and processed by Evaporated Coating Inc. Poly(3,4-ethylenedioxythiophene):poly(styrenesulfonate) (PEDOT:PSS) aqueous suspension was obtained from HC Starck (Clevios P VP AI 4083). The PEDOT:PSS was filtered through a 0.450 μm PTFE filter before use. Di-chlorobenzene (DCB, 99%) and 1,8-diiodooctane (DIO, 98%) were both from Sigma Aldrich. Ca and Al pellets were obtained from CERAC, Inc. P3HT was bought from Rieke Metals (Sepiolid P100, electronic grade, ~95% regioregular) and used directly as received. $PC_{60}BM$ were bought Sigma Aldrich (99.5%) and Nano-C (99.5%). Low band gap polymer PTB-7 was obtained from 1-Material Chemscitech Inc. The small molecule dye (SMD) was provided by Dr. Yi Liao in the Department of Chemistry at the University of Central Florida. The chemical structures of the materials used are shown in Figure 2. 7.

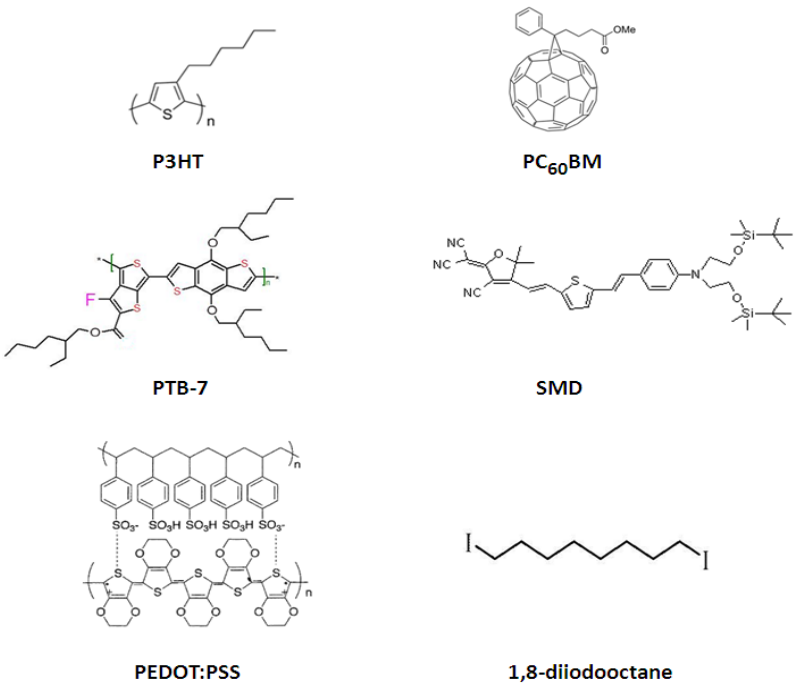

Figure 2. 7 Chemical structures of materials used in the fabrication of solar cells.

2.6.2 P3HT/PC_{60}BM Solar Cell Devices Fabrication

The organic solar cell devices were fabricated on the top of pre-cleaned ITO coated glass slides. Before device fabrication, the ITO coated slides were ultrasonically cleaned with detergent, DI H_2O, acetone (99.89%, OmniSolv, EMD) and isopropyl alcohol (HPLC grade, 99.9%, Sigma Aldrich) sequentially for 20 min each. The ITO substrate was blow-dried under N_2 and then cleaned in the UV/ozone system for 15 min. PEDOT:PSS was spin cast from an aqueous solution at 4000 rpm to form a film of 30-40 nm thickness. The substrate was then dried for 10 min at 140 ℃ in an oven and then transferred into the N_2 glove box for further spin casting of the photoactive layer.

A. PTB-7 Sensitized P3HT/PC_{60}BM Solar Cell

The solution of P3HT/PC_{60}BM (1:1 weight ratio) (P3HT: Sepiolid P100, Regioregularity (rr) ≈ 94%, Rieke Metals; PC_{60}BM, 99.5%, Nano-C) in dichlorobenzene was prepared with a concentration of (31.25 mg + 31.25 mg)/ml in the N_2 glove box, heated at 150 ℃ for about 2 hours under stirring and then was stirred overnight at 50 ℃ in the N_2 glove box. The low band gap polymer solutions were prepared separately with a concentration of 37.5 mg/ml (corresponding with the highest LBG doping level i.e. 30 wt% and taking into account solubility of the different materials) and submitted to similar heating and stirring treatment as P3HT/PC_{60}BM solutions. All these solutions were filtered with a 0.2 μm PTFE filter before blending.

According to the doping level of PTB-7 in the P3HT/$PC_{60}BM$ cells and using the precursor DCB solutions of P3HT/$PC_{60}BM$ and PTB-7, the ternary blend solutions were prepared with final concentrations of (25 mg: 25 mg: *x* mg)/ml for P3HT, $PC_{60}BM$ and PTB-7, respectively. Here, *x* is 1.25 mg, 2.5 mg, 5.0 mg and 7.5 mg, respectively, for devices with P3HT:$PC_{60}BM$:PTB-7 weight ratio of 1:1:0.05 (5 wt% PTB-7 doped), 1:1:0.1 (10 wt% doped), 1:1:0.2 (20 wt% doped) and 1:1:0.3 (30 wt% doped). For samples processed with solvent additive DIO, the spin coating solutions were prepared by adding 2.56 μl of DIO into 100 μl DCB solutions containing different PTB-7 doping levels. For devices prepared with DCB solutions and with DCB/DIO mixed solutions, 100 μl of these solutions were drop cast one time on top of PEDOT:PSS coated ITO slide and then spin coated at 800 rpm for 1 min. The film thickness remains at about 200-220 nm for all the active layers prepared measured with AFM. After active layer spin coating, the wet films were naturally dried in the N_2 glove box in 5 min and then loaded in the thermal evaporator system incorporated in the glove-box for cathode deposition of Ca (25 nm) and Al (80 nm). Note that all the devices herein were prepared in the same run so they can be used for comparison.

The absorption spectra of P3HT/$PC_{60}BM$ cells with various doping levels of PTB-7 (with or without DIO additive), were measured directly with the prepared device using the region without ITO pattern. A PEDOT:PSS covered slide was used as a reference sample. The UV-vis spectra for the active layer of these devices were measured with a

UV-vis spectrophotometer from Agilent Technologies Inc (Model 8453). The samples used for photoluminescence experiments were prepared on top of clean cover slides. Pure P3HT film was spin coated from a DCB solution with a concentration of 25 mg/ml at 800 rpm in a N_2 glovebox and dried in the nitrogen atmosphere. The P3HT/PTB-7 (wt ratio: 1:0.2) film was prepared with a solution concentration of (25 + 5) mg/ml under the same condition. Pure PTB film was spin cast from a solution of 5 mg/ml. The photoluminescence experiment was carried out in air with a NanologTM HoribaJobin Yvon fluorimeter. Topography and phase imaging experiments were conducted for the active layers by an atomic force microscopy (AFM, Digital Instruments Dimension 3100) in tapping mode.

B. Small Molecule Dye (SMD) Sensitized P3HT/$PC_{60}BM$ Solar Cell

The solution of P3HT/$PC_{60}BM$ was prepared similarly as described in **A**. The SMD solution was prepared separately with a concentration of 44.9 mg/ml. According to the doping level of the dye in the P3HT/$PC_{60}BM$ cells, the blend solutions were prepared with final concentrations of (25 mg: 25 mg: *x* mg)/ml for P3HT, $PC_{60}BM$ and dye, respectively. Here, *x* is 1.25 mg, 2.5 mg, 5.0 mg and 7.5 mg, respectively, for devices with P3HT:$PC_{60}BM$:SMD weight ratio of 1:1:0.05 (5 wt% SMD doped), 1:1:0.1 (10 wt% doped), 1:1:0.2 (20 wt% doped) and 1:1:0.3 (30 wt% doped). 100 μL of the ternary solutions were drop cast one time on top of a PEDOT:PSS coated ITO slide and then spin coated at 800 rpm for 1 min. Immediately after film spin coating, the wet films

were covered with a petri dish with a volume of about 15 cm^3 for 20 min. The purpose of this is to slow down the solvent evaporation rate and therefore producing an ordered structure of P3HT domains in the active layer.[34] The film thickness remains at about 200-220 nm for all the active layers prepared as measured with AFM. The samples were finally loaded in the thermal evaporator system for cathode deposition of Ca (25 nm) and Al (80 nm). Note that all the devices herein were prepared in the same run so they can be used for comparison.

The UV-vis spectra for the active layer of these devices were measured with a Varian Cary 300 Bio UV-Vis scanning spectrometer. The films used for photoluminescence experiments were spin coated from chloroform solutions since pure SMD solution in DCB cannot yield a continuous film. The concentration of pure P3HT solution is 5 mg/ml, the 10 wt% SMD doped P3HT sample has a concentration of (5 + 0.5) mg/ml and pure SMD solution is 0.5 mg/ml. All the films were prepared on clean cover slides with a spin coating rate of 800 rpm. No post-annealing experiments were done with these films. Topography and phase imaging experiments were conducted for the active layers by an atomic force microscopy (AFM, Digital Instruments Dimension 3100) in tapping mode.

CHAPTER 3. SINGLE MOLECULE SPECTROSCOPY AND MORPHOLOGY STUDIES OF A DIBLOCK COPOLYMER CONSISTING OF P3HT AND C_{60}*

3.1 Introduction

Bulk heterojunction-organic photovoltaic devices (BHJ-OPVs) with active layer consisting of a conjugated polymer as an electron donor and a fullerene derivative as an acceptor have been proven to be a very promising cost-effective technology to harvest solar energy.[20,22,24,57,59] Morphology with a balanced nanoscale phase separation and an interpenetrating donor-acceptor structure in the photoactive layer is crucial for exciton dissociation and transport due to the strongly electrostatically bound photogenerated electron-hole pairs (excitons) and short exciton diffusion length (5-20 nm).[85,108,109] Various approaches including thermal annealing, solvent annealing, solvent additives, or manipulation of the weight ratio of polymer and fullerene have been employed to achieve such nanometer scale morphology.[35,110] However, long term morphological stability poses a major challenge for these approaches.[57,111] For example, morphology studies on devices fabricated from blends of poly(3-hexylthiophene) (P3HT) and [6,6]-phenyl-C_{61}-butyric acid methyl ester ($PC_{60}BM$) demonstrate that the long term device efficiency and stability decrease due to macroscale phase separation between P3HT and $PC_{60}BM$.[112]

---

* This chapter has been published in Hu, Z. J.; Zou, J. H.; Deibel, C.; Gesquiere, A. J.; Zhai, L. *Macromolecular Chemistry and Physics* **2010**, *211*, 2416.

Donor-acceptor block copolymers have emerged as an exciting alternative to physically blended donor-acceptor materials in realizing optimal and controlled nanoscale morphology due to the inherent covalent linkage, the ability for chemically directed self-assembly and ease of tuning of the chemical structure of donor and acceptor moieties during synthesis.[113-119] These donor-acceptor block copolymers include poly(p-phenylenevinylene)-$C_{60,}$[113] poly(9,9-dialkylfluorine)-b-poly(2-alkyl- aniline)[117] and polytriphenylamine-b-polyperylene.[118] Among them, block copolymers containing P3HT and fullerene[120] are of particular interest since these two materials combined together have generated cells with power conversion efficiencies as high as 4-5%.[35,110] Block copolymers containing P3HT and fullerene derivatives have been demonstrated to stabilize the P3HT/PC_{60}BM system from destructive macroscale phase separation and improve the interfacial morphology.[120,121] Self-assembly and charge transport studies on polythiophene-fullerene triblock copolymers suggest that their optoelectronic properties are similar to that of P3HT/PC_{60}BM BHJ films.[49] However, molecular level studies on P3HT-fullerene block copolymers to investigate the effect of the fullerene block on the conformation of the P3HT block have not been performed. Such information is important to understand exciton migration and charge generation of the P3HT-fullerene block copolymers. In this chapter, we focus on the single molecule spectroscopy (SMS) and atomic force microscopy (AFM) morphology studies of poly(3-hexylthiophene)-b-poly(styrene-stat-4-vinylbenzylfullerene)

(P3HT-*b*-P(S-*stat*-VBCC_{60})), a block copolymer containing P3HT and C_{60}. This block copolymer was synthesized through a modified Grignard metathesis method (GRIM) and reversible addition-fragmentation chain transfer polymerization (RAFT) (Figure 3. 1) in Dr. Lei Zhai's lab at the University of Central Florida. The emission properties and their relation to molecular conformation were investigated by single molecule spectroscopy. The SMS investigations indicate that the P3HT homopolymer and the block copolymer both show "blue" (high energy chromophores) and "red" (low energy chromophores) site emissions, analogous to the previously studied MEH-PPV[69] and poly(3-octylthiophene) (P3OT)[122] conjugated polymers. However, owing to the rigid backbone and the small amount of chromophores of the P3HT moiety in the present polymers, the "blue" form emission dominates the single molecule ensemble spectra in this case. Attachment of the P(S-stat-VBCC_{60}) block slightly reduces the occurrence of the "red" sites but does not significantly affect the conformation of the backbone of the P3HT block according to simultaneous single molecule spectroscopy and single molecule emission polarization studies. The morphological studies by atomic force microscopy on spun-cast films of the block copolymer as well as the physical blend film of poly(3-hexylthiophene)-b-poly-(styrene-stat-4-vinylbenzyl-chloride) (P3HT-*b*-P(S-*stat*-VBC)) and $PC_{60}BM$ before and after thermal annealing indicate that the former is stable while the latter undergoes macroscale phase separation when subjected to identical thermal annealing times.

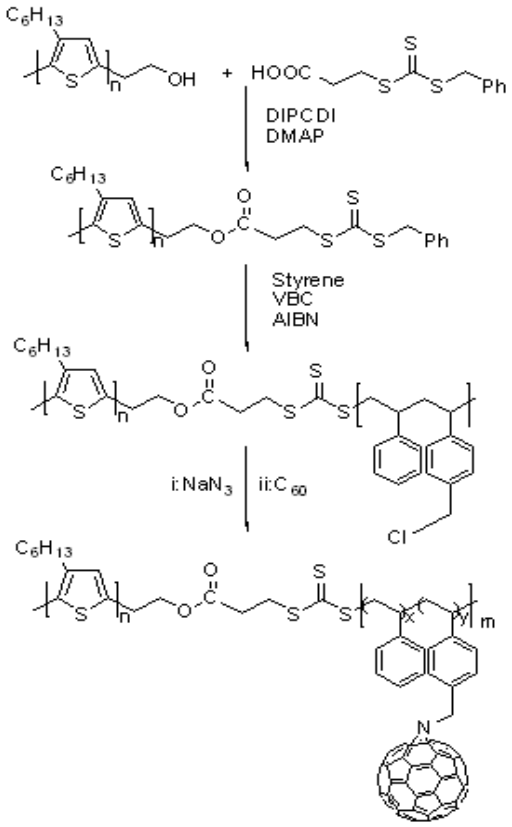

Figure 3. 1 Synthetic route of the block copolymer P3HT-*b*-P(S-*stat*-VBCC_{60}). P3HT: M_n=7500 (M_n: number average molecule weight), PDI=1.21; P3HT-*b*-P(S-*stat*-VBCC_{60}): x:y = 4.47:1, n:m = 1:3.01, M_n = 15400, PDI = 1.55.

3.2 Results and Discussion

3.2.1 Solution Spectroscopy

Figure 3. 2 shows the absorption and emission spectra of P3HT and P3HT-b-P(S-stat-VBCC_{60}) in chloroform. As shown in the absorption spectra, the absorption peak at 330 nm demonstrates the presence of the fullerene moiety in the copolymer P3HT-*b*-P(S-*stat*-VBCC_{60}). The absorption maxima for the P3HT and

P3HT-*b*-P(S-*stat*-VBCC_{60}) polymers are located at 449 nm and 445 nm, respectively, while the emission maxima are located at 573 nm. These observations indicate that the C_{60} block does not lead to additional ground state interactions that can be observed in the visible region of the spectrum. As depicted in Figure 3. 2, with respect to the P3HT emission spectra, an obvious fluorescence quenching (30%) is observed in P3HT-*b*-P(S-*stat*-VBCC_{60}) when these two solutions are adjusted to have the same absorbance at 449 nm. This quenching in the block copolymer is primarily attributed to photoinduced charge transfer from P3HT to fullerene portion, which has been extensively documented.[22,113,114] Contributions of energy transfer from the conjugated polymer block to the fullerene block in the copolymer also need to be considered.[20]

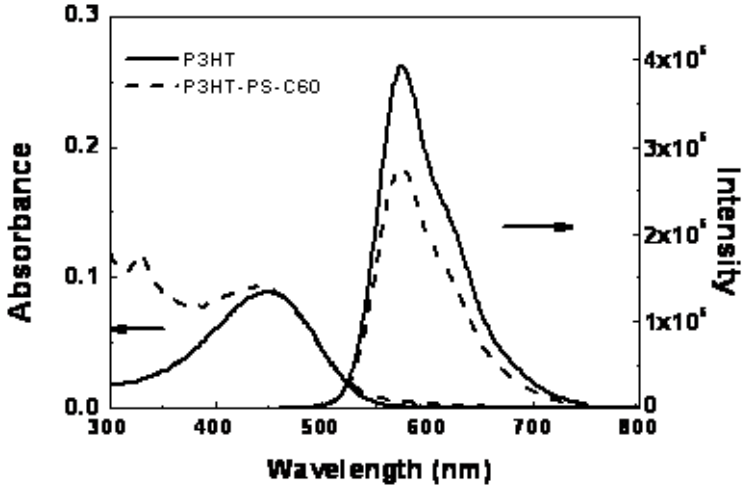

Figure 3. 2 Absorption (left) and emission (right) spectra of P3HT (solid) and P3HT-b-P(S-stat-VBCC_{60}) (dashed) chloroform solutions. These two solutions have same absorbance at 449 nm, which is the excitation wavelength for the emission spectra.

3.2.2 Single Molecule Spectroscopy

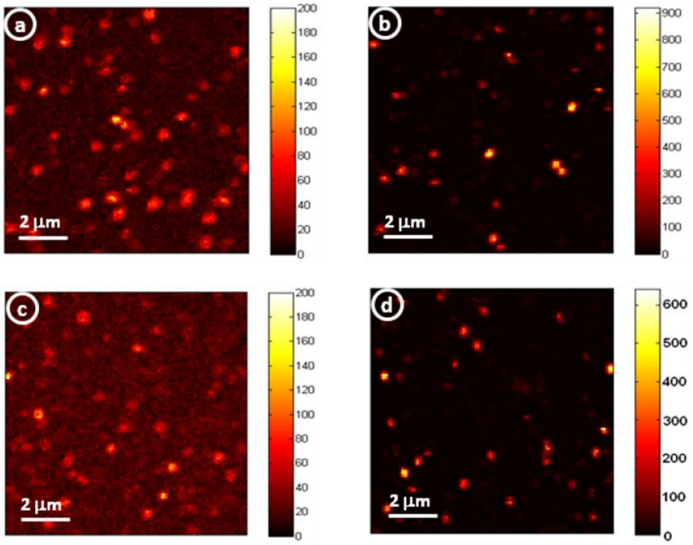

Figure 3. 3 Laser confocal microscopy images (10×10 µm^2) taken at 70 W/cm^2 under 488 nm excitation for P3HT single molecule sample (a) coated with 200 nm thick Al film and (b) without Al film, and for P3HT-*b*-P(S-*stat*-VBCC_{60}) single molecules (c) coated with 200 nm thick Al film and (d) without Al film. Scale bars indicate photon counts per dwell time (20 ms).

Figure 3. 3(a) and (b) present P3HT single molecule images with and without protective Al coating film, respectively. The molecules exposed to air show much higher fluorescence intensity with respect to those covered with an Al film. It has been shown that a high triplet concentration is produced under moderate to high excitation conditions in conjugated polymer molecules such as MEH-PPV.[123] Furthermore, there is a strong intersystem crossing in poly-alkylthiophene polymers due to increased spin-orbit coupling with the presence of sulfur atom.[124] The triplet state is a very well-known efficient quencher for the singlet state in multichromophoric molecules.[123,125] Therefore, a relatively low fluorescence emission intensity is observed

for P3HT single molecules in Al coated polymer samples. In contrast, when the polymer molecules are exposed to air, the triplet state population is decreased by O_2, an effective quencher for the triplet state, leading to increased fluorescence intensity in uncoated samples. Identical observations were made for P3HT-*b*-P(S-*stat*-VBCC_{60}) molecules (Figure 3. 3(c) and (d)), illustrating that aside from the charge transfer process, the basic photophysics of the P3HT block in the P3HT-*b*-P(S-*stat*-VBCC_{60}) block copolymer is similar to that of the P3HT homopolymer.

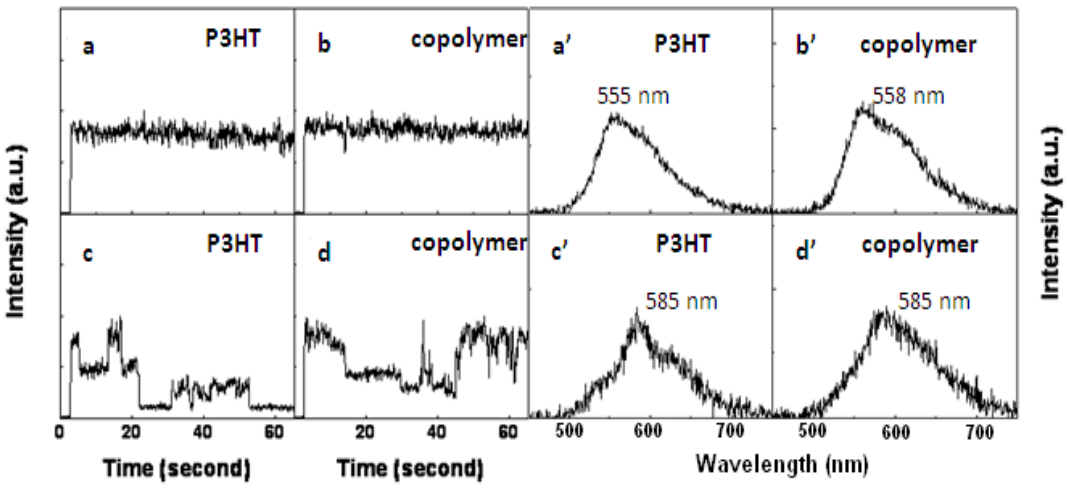

Figure 3. 4 Representative fluorescence transients of polymer molecules sealed with 200 nm thick Al film are shown in (a) and (b) for P3HT and P3HT-*b*-P(S-*stat*-VBCC_{60}), respectively. Figure 3(c) and (d) represent typical fluorescence transients of molecules in Al coated samples after longer duration of exposure to ambient air for P3HT and P3HT-*b*-P(S-*stat*-VBCC_{60}), respectively. All the transients were taken under 488 nm excitation with a power density of 70 W/cm^2 and dwell time of 100 ms. Corresponding single molecule spectra for transients (a-d) are shown as (a'-d'), respectively, for which the emission peak wavelengths are indicated.

Two typical single molecule fluorescence trajectories of P3HT and

P3HT-*b*-P(S-*stat*-VBCC$_{60}$) coated with a 200 nm thick aluminum film (to remove effects of presence of air) are presented in Figure 3. 4(a) and (b), respectively. The fluorescence intensity approximately remains stable over measured time without strong intensity flickering in both polymer molecules. Although ultrafast forward electron transfer processes (less than 100 fs) and much slower backward electron transfer processes (~ 1 μs)[126] exist in the P3HT-*b*-P(S-*stat*-VBCC$_{60}$) block copolymer upon photo-excitation, the time scale of both processes is much smaller than the time resolution of our experimental setup (1 ms), and are therefore not observable in these data. Several molecules in the Al coated samples show fluorescence blinking in fluorescence intensity time traces of both the P3HT homopolymer (Figure 3. 4(c)) and the block copolymer (Figure 3. 4(d)). Such observation provides evidence for the formation of low energy "red" aggregate sites in these single conjugated polymer molecules,[71,127] which is confirmed by their corresponding emission spectra shown in Figure 3. 4(c'-d'), respectively.

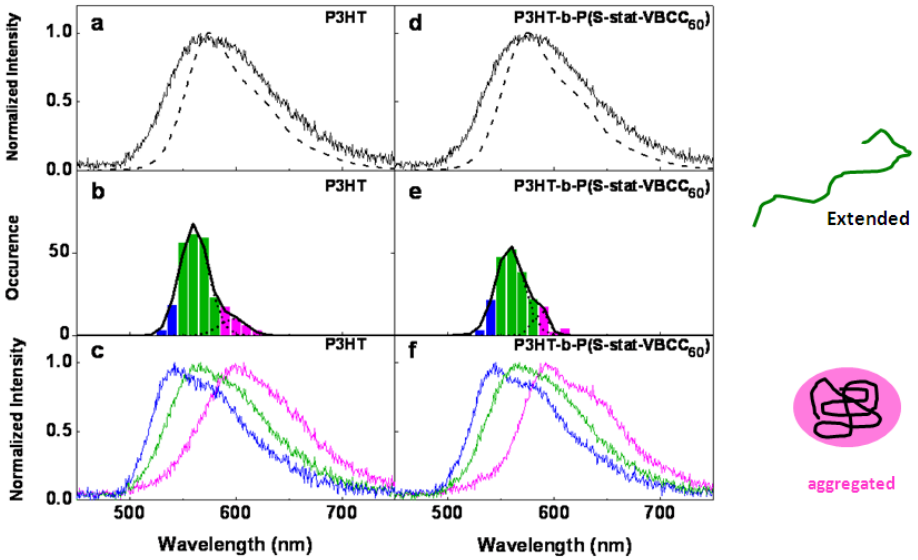

Figure 3. 5 Single molecule ensemble spectra of P3HT and P3HT-b-P(S-stat-VBCC60) are presented as back solid curves in (a) and (d), respectively. The corresponding solution emission spectra are shown as dashed curves in (a) and (d). (b) and (e) depict corresponding distribution histograms of single molecule emission peak wavelength, which are fitted to Gaussian curves (dotted). Based on the fitting, the ensemble distributions were split into sub-ensemble distributions, indicated with different colors. *Note that the blue edge was split from the bulk of the histogram (green) due to its large blue shift compared to the bulk solution emission maximum.* Panels (c) and (f) depict the sub-ensemble spectra constructed by adding up single molecule spectra with peak wavelengths indicated by the color scheme in the corresponding peak wavelength histograms (panels (b) and (e)). For both the homopolymer and the block copolymer, the sub-ensembles were constructed by using 545 nm to distinguish between blue and green spectra, while 585 nm was used to distinguish between green and purple spectra. The cartoons shown in the right depict extended and loosely aggregated conformations that the polymer molecules might take.

Figure 3. 5 shows the single molecule ensemble spectra ((a) and (d)) and emission peak emission wavelengths distribution histograms ((b) and (e)) of the P3HT homopolymer and P3HT-*b*-P(S-*stat*-VBCC$_{60}$) block copolymers. The ensemble emission spectra of these two polymers are similar to their chloroform solution emission counterparts (Figure 3. 2), with the emission maxima of the ensembles at 571 nm and 574 nm for

P3HT and P3HT-*b*-P(S-*stat*-VBCC$_{60}$), respectively. Both P3HT and P3HT-*b*-P(S-*stat*-VBCC$_{60}$) show a wide peak wavelength distribution as shown in Figure 3. 5(b) and (e), respectively. A comparison with previously studied molecules such as MEH-PPV and P3OT can provide more detailed information about the observed spectral distribution. SMS studies on MEH-PPV have revealed a bimodal distribution in their peak wavelength histograms corresponding due to "blue" and "red" sites in polymer chain.[69] In contrast, only a single broad distribution was observed for P3OT single molecules,[122] which resembles our results in the presently investigated conjugated polymers. A detailed Frank-Condon vibronic analysis has clearly revealed the presence of "blue" and "red" chromophores in P3OT, similar to MEH-PPV. However, this bimodal distribution was masked due to the greater energy disorder in the chromophores and the dominance of "red" forms.[122] For both conjugated polymers in present work, analogous "blue" and "red" spectra were also detected. Figure 3. 5(c) and (f) show the sub-ensemble spectra constructed according to the peak wavelengths depicted in histograms in Figure 3. 5(b) and (d). The spectra in the bulk of the histogram are marked green, with their correspondingly color coded sub-ensemble emission spectra shown in Figure 3. 5(c) and (f). The short-wavelength edge (marked with blue) and the long-wavelength edge (marked with purple) of the histogram were evaluated in the same way. Obvious spectral differences between the spectra in the bulk of the histograms, and the short-wavelength and long-wavelength edges of the

histograms can be observed from the resulting sub-ensemble emission data. Specifically, the peak emission wavelengths of the sub-ensembles of P3HT are strikingly different, at 543 nm, 566nm, and 603 nm for the blue, green, and purple sub-ensembles, respectively. A similar phenomenon was observed at 544 nm, 567 nm, and 593 nm for P3HT-*b*-P(S-*stat*-VBCC$_{60}$) for the blue, green, and purple sub-ensembles, respectively. The emission maximum of the green sub-ensemble spectra is comparable to that of the molecular solutions. The difference in emission maxima of about 30 nm between the green and purple sub-ensemble spectra is analogous to that found for the "blue" and "red" spectra in MEH-PPV[69] and P3OT.[122] These observations suggest the presence of "red" sites in the subset of molecules that makes up the purple sub-ensemble. In contrast, the spectra on the short-wavelength edge of the histograms, which are severely blue-shifted with respect to the molecular solution and green sub-ensemble data, are most likely due to emission of molecules with high energy, short conjugation length P3HT chromophores that may be indicative of the polydispersity of the measured samples. In addition, an approximately 10 nm blue shift in the peak wavelength of the purple sub-ensemble spectra was observed in the block copolymer (593 nm) with respect to the P3HT homopolymer (603 nm). This can be explained by the interruption of the stacking in the "red" sites in the block copolymer with the attachment of the fullerene block of P(S-stat-VBCC$_{60}$).

Finally, based on the large number of single molecules that show emission spectra

similar to the emission spectra found for molecular solutions, it can be assumed that the single molecules embedded in a PMMA film to a large extent remain in a conformation analogous to that in solution, which is a reasonable assumption given the low molecular weight and rigidity of the P3HT segment in both the homopolymer and block copolymer. Indeed, this is in contrast with the observations made for P3OT, for which a strong red shift of ~ 60 nm has been observed in single molecule ensemble spectra of a high molecular weight P3OT (M_w: 142 kDa) with respect to corresponding molecular chloroform solution.[122] This substantial red shift was ascribed to the increased occurrence of "red" sites in single polymer chains due to the formation of a collapsed conformation in the solid state of the large molecular weight P3OT. Such an observation is not made in our case, suggesting that the polymers in the study presented here maintain an extended conformation similar to the conformation found in solution. Thus, this is a clear difference from the previously reported work on high molecular weight P3OT. In our case, a large number of molecules occur in the green sub-ensemble, which are molecules that show solution-like emission spectra, whereas for P3OT almost all single molecule spectra are red shifted with respect to solution irrespective of the presence of "blue" or "red" type emitters. Furthermore, while P3HT and P3HT-b-P(S-stat-VBCC_{60}) have a similar distribution of single molecule peak emission wavelengths compared to P3OT, much less "red" sites (i.e. molecules with collapsed conformation) are observed. This can again be explained by the low molecular weight

and the rigidity of P3HT moiety which reduces the probability to form "red" sites in polymer chains or coiled chains. This was investigated further by fluorescence polarization studies as described below. In addition, the difference in peak emission wavelengths of the "red" sites in the block copolymer with respect to the homopolymer indicates that the fullerene block has the potential to disturb intramolecular folding interactions, although the effect is only minor in this particular case.

3.2.3 Single Molecule Fluorescence Polarization Imaging

For conjugated polymer molecules, the polymer chain conformation can be related to its emission anisotropy, which is determined by the molecular transition dipole moment(s).[11,75] To better understand the molecular conformation in relation to the observed fluorescence properties, fluorescence polarization anisotropy imaging was also conducted for P3HT and P3HT-b-P(S-stat-VBCC_{60}). Figure 3. 6(a) and (b) depict two fluorescence images of a P3HT homopolymer single molecule sample taken simultaneously at two orthogonal polarization directions under circularly polarized excitation. It is obvious that most of molecules with high intensity in one detector channel are hardly observable in the other (see, for instance, molecules A and B). A similar phenomenon was observed for the block copolymer (see Figure 3. 6(d-f)). For each single molecule, the emission polarization ratio was calculated by Equation 3.1

$$P = \frac{I_1 - GI_2}{I_1 + GI_2}, \tag{3.1}$$

where I_1 and I_2 are components of emission intensity split into two orthogonal polarization directions, and G is a correction factor for the sensitivities of the two orthogonally polarized emission channels.[15,71,128]

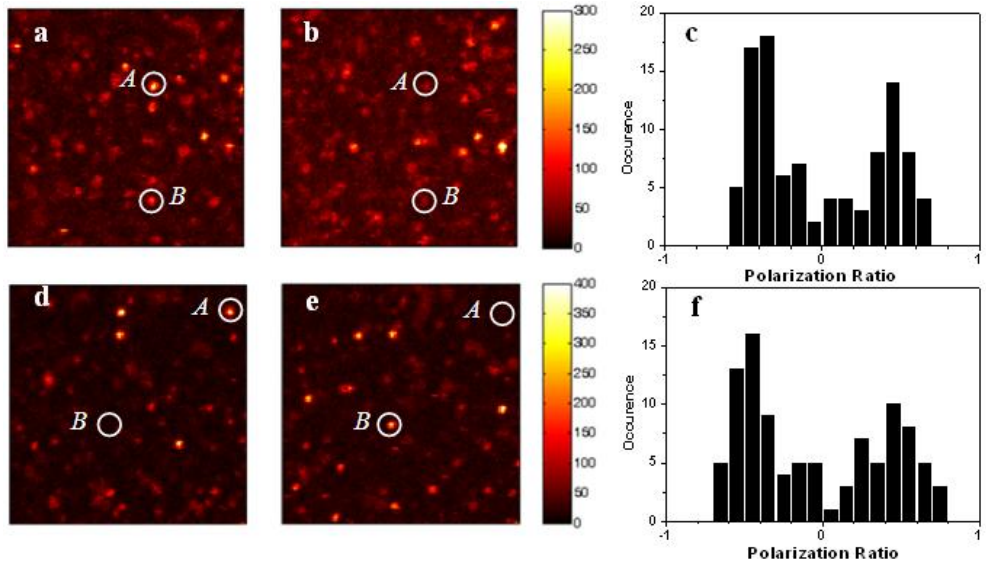

Figure 3. 6 Fluorescence images (scan range: 10 × 10 μm^2) obtained simultaneously at two orthogonal polarization directions under circularly polarized laser excitation at 488 nm are shown in (a) and (b) for the P3HT homopolymer, and (d) and (e) for the P3HT-b-P(S-stat-VBCC$_{60}$) block copolymer, respectively. Scale bars indicate photon counts per dwell time. The polarization ratio distribution histograms constructed from about 100 single molecules in each polymer are given in (c) and (f) for the P3HT homopolymer and the block copolymer, respectively.

Polarization ratio histograms were constructed for the P3HT polymer and the block copolymer. As shown in Figure 3. 6(c) and (f), the polarization ratio indicates a moderate polarization ratio that is centered at about ± 0.5 with a minimum at 0 in both cases, indicative of an extended conformation (Figure 3. 5) containing rigid rod-like polymer segments connected by conformational defects such as twisted backbone

(σ-bond rotation) and chemical defects such as imperfect thiophene rings (presence of saturated carbon atoms).[129-131] Close inspection of the polarization data and the simultaneously acquired fluorescence spectra for individual molecules reveals that, for both the homopolymer and the block copolymer, molecules with "red" site emission show polarization values in the range of ± (0.5-0.7) as displayed in Figure 3. 7(a) and (d). This strong polarization again substantiates the fact that only one or a

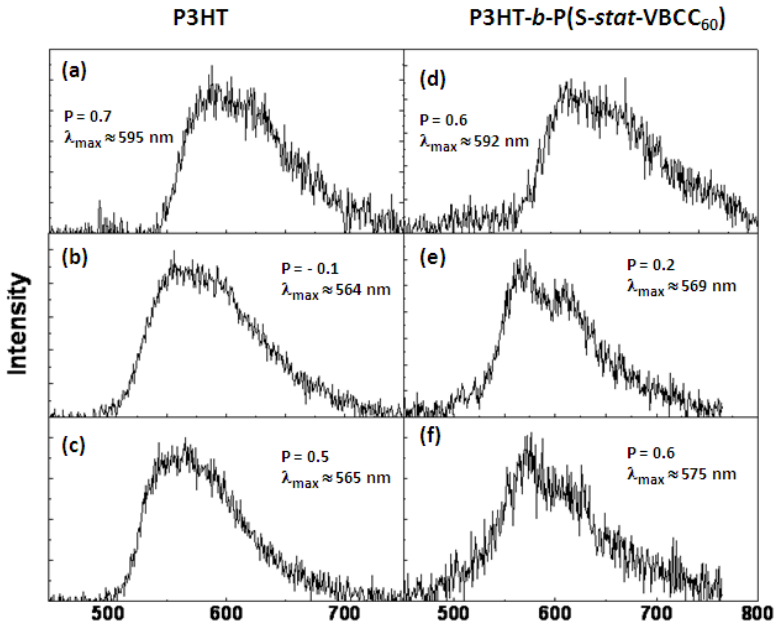

Figure 3. 7 Single molecule spectra with for P3HT (left column, (a)-(c)) and P3HT-b-P(S-stat-VBCC$_{60}$) (right column, (d)-(f)). The polarization anisotropy values (P) and fluorescence emission maxima are indicated in each panel.

few chromophores emit in molecules with "red" sites, caused by efficient energy transfer in an aggregated molecular conformation (Figure 3. 5) to a localized lower energy chromophore. In comparison, molecules with blue and green spectra (higher energy emission) also show high polarization but with a relatively broader range, i.e.

from 0 to ± 0.6 (see Figure 3. 7(b)-(c) and (e)-(f)). These observations indicate that even in the potential presence of exciton migration along the polymer backbone, emission depolarization is not considerable. Furthermore, based on the comparison of polarization ratios of the P3HT homopolymer and the donor-acceptor block copolymer, the grafting of a block of P(S-stat-VBCC_{60}) to P3HT does not pronouncedly change the conformation of the P3HT block, i.e. it mostly remains in an extended conformation and occasionally shows folding of rigid extended segments onto themselves in a single molecule. This is a new observation originating from the rigidity of the P3HT block, which is clearly distinct from previously reported observations made for a DMOS-co-MEH-PPV copolymer [DMOS=2-dimethyloctylsilyl-1,4-phenylene-vinylene; MEH=2-methoxy-5-(2'-ethyl-hexyloxy)-1,4-phenylenevinylene].[132] For the latter it was found that the presence of the DMOS block in the DMOS-co-MEH-PPV copolymer caused ordering of the MEH-PPV blocks, which lead to a significantly larger fraction of "red" emitting MEH-PPV sites in the block copolymer compared to the MEH-PPV homopolymer as shown in Figure 3. 8. In other words, the presence of the DMOS block caused a collapse and folding of the MEH-PPV block onto itself, presumably due to the flexibility of the MEH-PPV block.

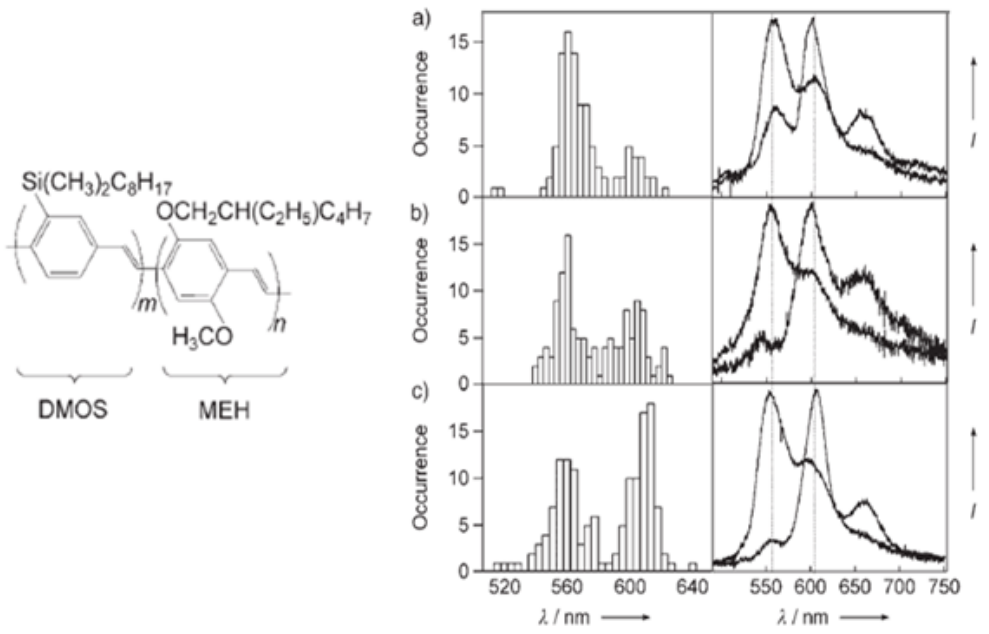

Figure 3. 8 Histograms of peak wavelengths (left) and sorted subensemble spectra (right) for a) MEH (M_w: 186 kDa), b) MEH (M_w: 1000 kDa), and c) DMOS-co-MEH (MEH block M_w: 186 kDa), excited at 488 nm at around 20 K. The dotted vertical lines show the peak wavelength positions of the "red" and "blue" emitting forms of MEH in the diblock polymer as well as the polymers of different molecular weights. (Reproduced from reference[133])

3.2.4 Phase Separation of P3HT-b-P(S-stat-VBCC$_{60}$)

The morphology of a P3HT-*b*-P(S-*stat*-VBCC$_{60}$) thin film drop cast from toluene solution (2 mg/ml) was characterized by AFM. In the topography image (Figure 3. 9(a)), nanofibrils formed by the P3HT block can be clearly identified. The simultaneously acquired phase image shown in Figure 3. 9(c) reveals a microphase separation. According to previous investigations by Dante et al,[33,49,134] the light regions are assigned to P3HT-containing rod block while the dark areas can be assigned to the C_{60}-containing block. As can be observed, the microphase separation of the as-cast

sample was not well developed with ill-defined features whose domain size ranges from tens to hundreds nanometer. To allow the microphase separation to become fully developed, the P3HT-*b*-P(S-*stat*-VBCC_{60}) film was annealed at 140 ℃ for 30 min. A well-defined microphase separation is observed in Figure 3. 9(e). The domain size of the phase separation is around 10-50 nm which is comparable to the exciton diffusion length (5-20 nm).[85,108,109] The phase separation of a P3HT-*b*-P(S-*stat*-VBC) and $PC_{60}BM$ mixture (weight ratio equals to P3HT-*b*-P(S-*stat*-VBC)/C_{60} ratio in P3HT-*b*-P(S-*stat*-VBCC_{60})) was studied for comparison. Figure 3. 9(b) and d illustrate the topography and phase images of the blended sample before annealing, respectively. Clearly, P3HT nanofibrils are found to accumulate at the film surface, implying a vertical phase separation of P3HT-*b*-P(S-*stat*-VBC) and $PC_{60}BM$. A similar phenomenon has been reported for the P3HT/$PC_{60}BM$ system and attributed to the differences in solubility and surface energy of the components as well as the dynamics of the film processing.[27,112,135] After 30 min of thermal annealing at 140 ℃, the phase image (Figure 3. 9(f)) reveals microphase separation of P3HT-*b*-P(S-*stat*-VBC) and $PC_{60}BM$ due to the diffusion of $PC_{60}BM$ to the surface of the film. However, the phase separation is not as well-defined as P3HT-*b*-P(S-*stat*-VBCC_{60}). Moreover, the microphase separation is not thermodynamically stable. Increasing annealing time to 1 hour leads to macrophase separation with the $PC_{60}BM$ aggregation size increasing to ~ 1 μm (Figure 3. 9(g)). In contrast, the microphase separation of

P3HT-*b*-P(S-*stat*-VBCC$_{60}$) is stable against identical thermal annealing.

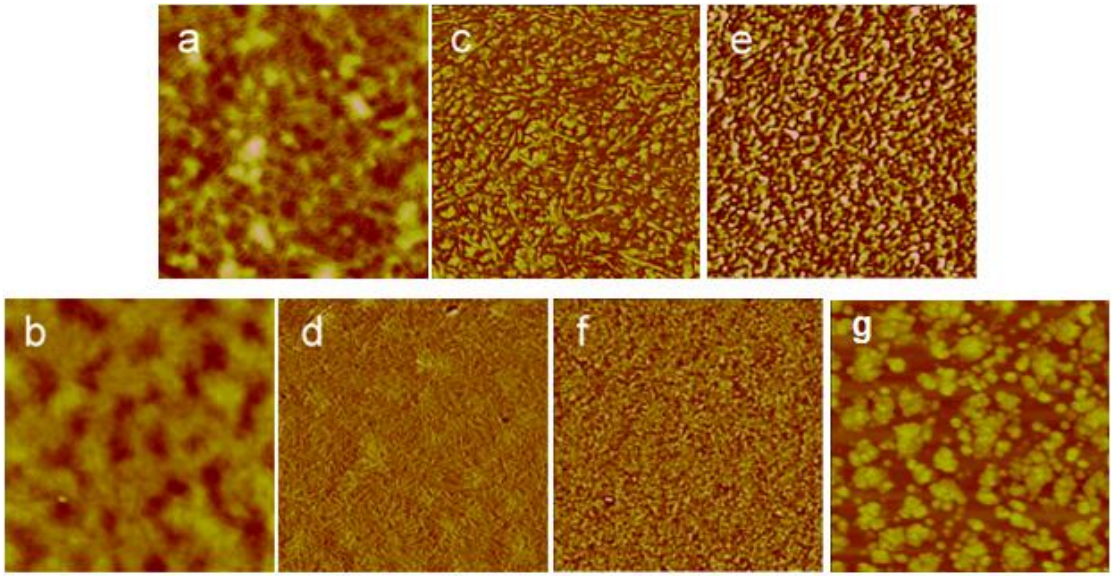

Figure 3. 9 AFM images of P3HT-*b*-P(S-*stat*-VBCC$_{60}$) (top) and the blend P3HT-*b*-P(S-*stat*-VBC)/PC$_{60}$BM (bottom) thin films. (a) and (b): topography image before annealing; (c) and (d): simultaneously acquired phase image of topography images in (a) and (b); (e) and (f): phase images after thermal annealing at 140 ℃ for 30 min. (g): topography image of the blend P3HT-*b*-P(S-*stat*-VBC)/PC$_{60}$BM films after annealing at 140 ℃ for 1 hour. Topography image area is 2.0 × 2.0 μm^2 with z-scale of 50 nm. Phase angle scale of the phase images is 50 °.

3.3 Conclusion

The effect of molecular structure on the molecular conformation of a block copolymer P3HT-*b*-P(S-*stat*-VBCC$_{60}$) was investigated and compared to the corresponding P3HT homopolymer by solution and single molecule spectroscopy. It was observed that the fluorescence emission of the P3HT homopolymer and the P3HT-b-P(S-stat-VBCC$_{60}$) block copolymer can be categorized into “blue” and “red” forms, in analogy with

previously studied MEH-PPV and P3OT. However, in contrast to the dominant “red” form found for those conjugated polymers, the “blue” form dominates in the present work for both the homopolymer and block copolymer due to the low molecular weight and rigidity of the P3HT portion. The latter was confirmed by a single molecule polarization analysis, which suggests extended P3HT segments in both polymers. Both spectroscopy and polarization investigations indicate that the grafting of the C_{60}-containing block does not strongly change the conformational structure of the P3HT moiety. AFM morphological studies on the block copolymer and the blend of (P3HT-*b*-P(S-*stat*-VBC)) and $PC_{60}BM$ thin films before and after thermal annealing reveal that the block copolymer is stable upon thermal annealing while the blend undergoes macroscale phase separation.

CHAPTER 4. SINGLE MOLECULE SPECTROSCOPY ON THIOPHENE-BASED POLYMERS SHOWING DIFFERENT MACROSCOPIC CRYSTALLIZATION BEHAVIORS

4.1 Introduction

In organic opto-electronic devices such as OFET, OPVs and sensors based on conjugated polymers, these polymers form ordered structures from the nano- to macro-scale that are of critical importance in determining device properties, function and performance.[136] Typically, highly ordered (quasi-)crystalline structures are desired since the performance of these devices correlates strongly with the charge mobility in the polymer materials that make up the active layer in the device.[136,137] These highly ordered structures exhibit an intimate contact between adjacent conjugated polymer backbones that facilities efficient and rapid migration of charge through the conjugated polymer material. Investigations on the crystallization behavior of conjugated polymers are therefore imperative for studying intrinsic charge transport properties, understanding the fundamental structure-property relations and designing novel polymers with optimized properties. Like most of the other materials, the crystallization behavior at different length scales largely depends on the chemical structure (architecture) and morphology of the individual chains.[136,138-140] Figure 4. 1 shows scanning tunneling microscope (STM) data providing a direct observation of polymer chain folding as a function of architecture of the polymer. STM imaging on two-dimensional poly (3-alkylthiophene) (P3AT) crystal reveals significant folding of

these conjugated polymer chains, while no obvious chain folding was detected for the conjugated polymer poly[(5,5'-(3,3'-di-*n*-octyl-2,2'-bithiophene))-*alt*-(2,7-fluoren-9 -one)] (PDOBT) that has a more rigid backbone.[139] These molecular structure-dependent folding properties are expected to dominate the crystallization behaviors in three dimensions as sketched in Figure 4. 2(a). Besides polymer backbone folding the crystallization behavior is also driven by the intermolecular pi-pi stacking forces. These non-covalent interactions can lead to the formation of fibrillar structures with the pi-pi stacking along the long axis (i.e. propagation direction) of the fibril while the alkyl side chain stacking is along the cross-section of the fibril. This arrangement is illustrated in Figure 4. 2(a).

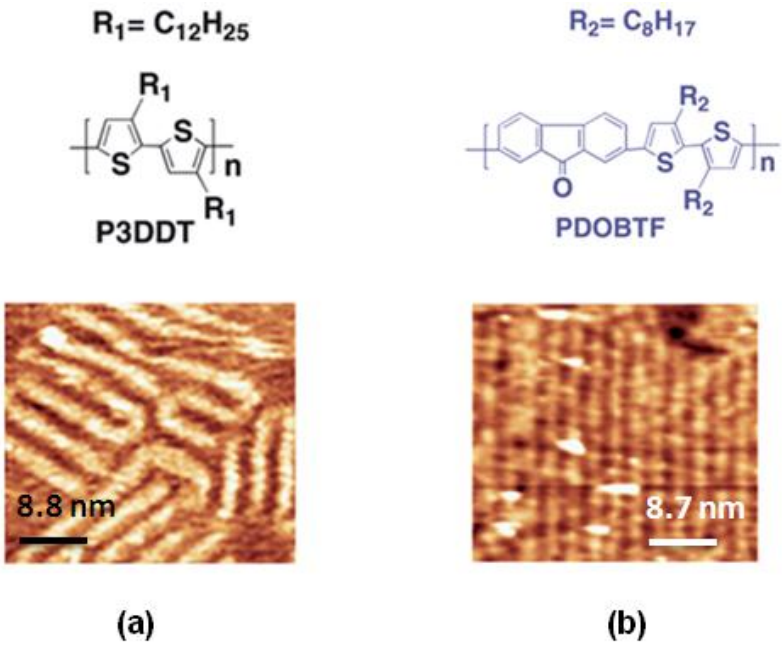

Figure 4. 1 STM images for monolayers of P3DDT (a) and PDOBTF (b), respectively. The corresponding chemical structures of the polymers are shown on top of the STM images. (Adapted from reference[139])

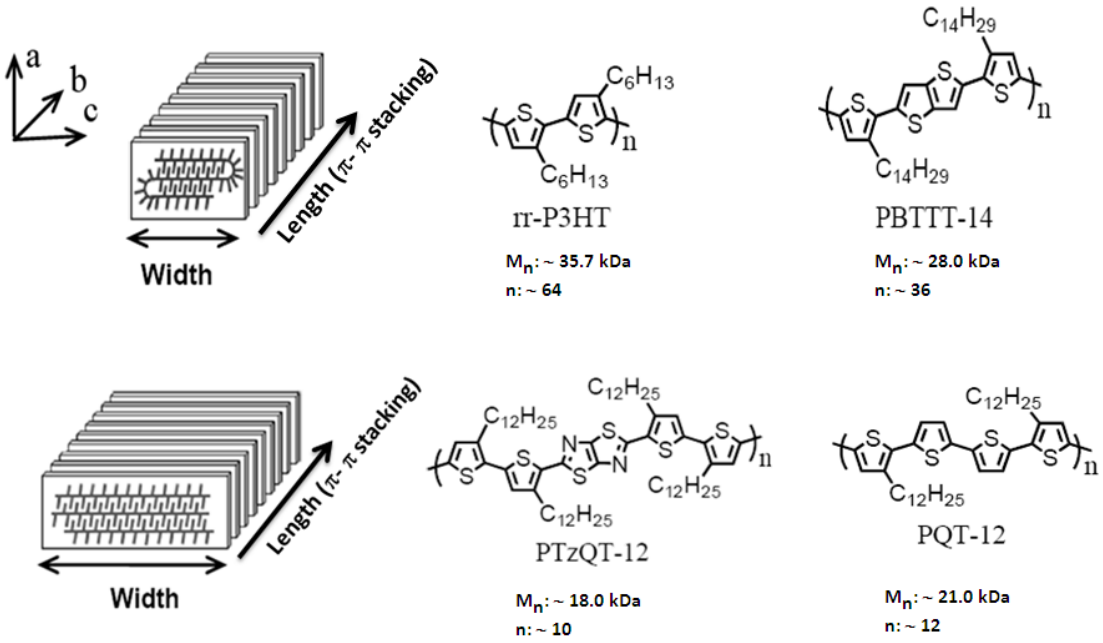

Figure 4. 2 Illustrations of crystalline structure with polymer chain folding (top) or non-folding (bottom). In the study by Liu et al, rr-P3HT and PBTTT-14 polymer chains exhibit folding while PTzQT-14 and PQT-12 show non-folding in their crystals when these polymers have a molecule weight larger than ~ 10 kDa.[141] These four thiophene-based conjugated polymers used here are shown in the left. [rr-P3HT = poly (3-hexylthiophene); PBTTT-14 = poly(2,5-bis(3-tetradecylthiophen-2-yl)-thieno [3,2-b]thiophene); PTzQT-12 = poly(2,5-bis(3-tetradecylthiophen-2-yl) thiophene-2-yl)thiophen-2-ylthiazolo[5,4-d]thiazole); PQT-12 = poly(3,3-didodecyl-quarterthiophene)]. Beneath the chemical structure of each polymer, the number average molecule weight (Mn measured with GPC) and the number of repeat units are given. Note that the numbers of repeat units were calculated from corrected values of Mn since GPC tends to overestimate the actual molecular weight of rigid-rod conjugated polymers by a factor of about 1.7.[142] (Adapted from reference[141,143])

Thiophene-based conjugated polymers have been intensively studied in organic opto-electronic devices over the past decade due to their desirable properties including the ability to self-organize into highly ordered structures that exhibit high charge mobility and broad absorbing range of visible light.[3] Recently, by studying polymer

crystals formed in dilute solutions using marginal solvents, Liu et at[141] characterized in detail the nanocrystal structures developed with the four different thiophene-based polymers as shown in Figure 4. 2, and related the crystalline features with distinct folding and non-folding properties of these polymers. Briefly, with similar number average molecule weight the conjugated polymers rr-P3HT and PBTTT-14 show polymer chain folding in the corresponding nanocrystals while PQT-12 and PTzQT-12 do not exhibit folding of the polymer chains. This experimental finding was also corroborated by a theoretical analysis with respect to the inter-ring σ bond.

Although a relationship between the chemical structures and crystallization behavior has been studied for these four thiophene-based polymers, it is not clear *1) whether this kind of folding or non-folding conformation occurs at the single molecular level (i.e. property of individual chains) or in a specific crystallization environment (i.e. property of the crystal), and 2) what are the possible different conformations at the single molecule level*. As we demonstrate in Chapter **3**, SMS has great advantages in probing the photophysics, photochemistry and conformation of individual chains of conjugated polymers.[144] Herein, we extend the SMS investigation to the spectroscopic and morphological properties of individual polymer chain of these four different thiophene-based conjugated polymers with the aim of *understanding the correlation between the polymer chain conformation and polymer architecture at the single molecule level*. These experiments will be conducted by studying the emission spectra

and polarization anisotropy of the individual polymer chains. Our results indicate that the folding and non-folding behavior of the polymers under investigation are strongly related to the chemical structure of the polymers and molecular weight. It was revealed that the chain folding properties of P3HT strongly depend on its molecular weight. High molecular weight can result in strongly folded polymer chains with strong segmental interaction. PQT-12, although with a similar polymer backbone and molecule weight as the high molecular weight (MW) P3HT, displays less chain folding relative to P3HT probably due to a higher rotation energy barrier of interring σ-bonds. With respect to the high MW P3HT, PBTTT-14 exhibits a less folding due to a more rigid polymer backbone as a result of fused thiophene rings. The PTzQT-12 polymer chain exhibits the least folding among all the four polymers studied as a result of the most rigid and planar conjugated segments. The study completed herein also illustrates that the folding properties of molecules in nanocrystals and bulk materials is also affected by interchain interactions, which needs to be considered when discussing folding and non-folding polymers.

4.2 Results and Discussion

4.2.1 Solution Spectroscopy

Figure 4. 3 summarizes the absorption and emission spectra of chloroform solutions of P3HT (with low and high MW), PBTTT-14, PTzQT-12 and PQT-12. The analogy of the

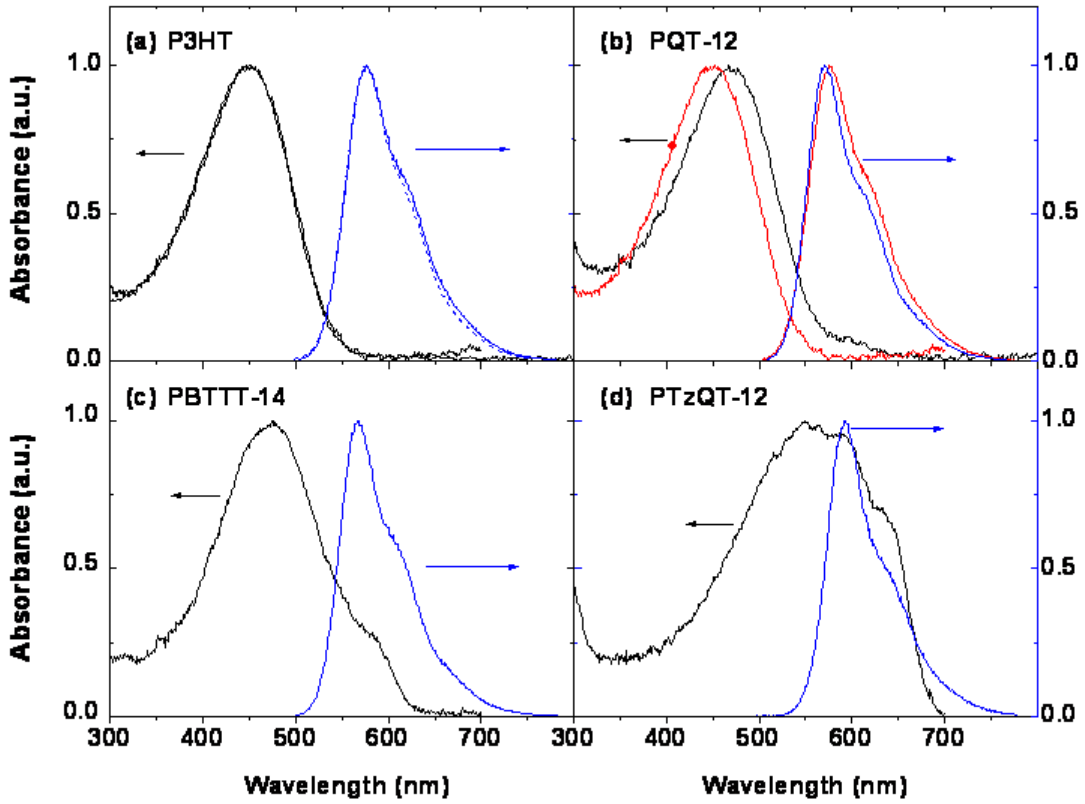

Figure 4. 3 Absorption and fluorescence emission spectra of P3HT (a), PQT-12 (b), PBTTT-14 (c) and PTzQT-12 (d) chloroform solutions, respectively. In (a), the absorption and emission spectra of P3HT with a low MW (M_n: ~ 7.5 kDa) are shown as dot curves for comparison with a high MW P3HT (M_n: ~ 37.5 kDa). All the measurements were taken under room temperature. In (b), the absorption and emission spectra of the high MW P3HT (M_n: ~ 37.5 kDa) are included as red curves for comparison with that of PQT-12 (shown as black and blue curves).

absorption and emission spectra of the high- and low-MW P3HT in chloroform indicates similar statistical distribution of chromophore energies of these two polymers in solution. In the absorption spectra of PBTTT-14, the absorption maximum is red shifted to 474 nm compared with 452 nm for P3HT, due to a rigid backbone caused by the fused thiophene ring and the presence of the highly delocalized thienothiophene aromatic rings in PBTTT-14.[137,145,146] The appearance of a shoulder at ~ 590 nm in the

absorption spectrum is probably caused by the intrachain pi-pi association.[147] The absorption spectrum of PTzQT-12 peaks at 545 nm (2.28 eV) and exhibits two pronounced vibronic features at ~ 590 nm (2.11 eV) (with stronger intensity than observed for PBTTT-14) and 640 nm (1.94 eV). The energy differences of about 0.17 eV between the absorption maximum and shoulder, and between shoulder and shoulder can be associated to the C=C stretching vibration of the thiophene ring which has an energy of 0.18 eV.[148,149] The red shifted maximum and structured vibronic features of PTzQT-12 absorption spectrum compared with the other three polymers are attributed to a very rigid and coplanar backbone, and an enhanced intramolecular charge transfer in the donor-acceptor type backbone due to the introduction of thiazolothiazole unit.[150,151] Figure 4. 3(b) presents the absorption and emission spectra of PQT-12 (black and blue curves) in comparison with P3HT (M_w: ~ 37.5 kDa, red curves) since these two polymers have the same polymer backbone. As can be seen, the absorption of PQT-12 is red shifted by ~ 25 nm while the emission spectra are very similar. This red-shifted absorption is due to a longer conjugation length in chromophores presumably resulting from a more planar backbone PQT-12. The similarity in emission spectra indicates a similar polymer backbone conformation in the molecular solution despite of the distinction of the side chains in these two polymers. Compared with the Stokes shift value of 125 nm for P3HT, the values of Stokes shift for PQT-12, PBTTT-14 and PTzQT-12 are 104 nm, 94 nm and 43 nm, respectively. These reduced

Stokes shift values for PQT-12, PBTTT-14 and PTzQT-12 can be attributed to reduced degrees of freedom and conformational reorganization in the excited state as a result of polymer backbone rigidity.[152,153]

4.2.2 Single Molecule Spectroscopy

Single molecule images and transients. Figure 4. 4 displays the SMS fluorescence images for single molecules of P3HT (high MW), PBTTT-14, PTzQT-12 and PQT-12, respectively. All the samples are coated with a 200 nm thick Al film to ensure the photostability of the conjugated polymer molecules. These polymer molecules when studied in ambient air (not coated with Al overlayer) display much higher fluorescence intensities with respect to those samples covered with an Al film, which is similar to what we found for the low MW P3HT as discussed in Chapter **3**, and is related to the formation of triplets.[144] As can be seen from the images in Figure 4. 4, most fluorescence spots (individual molecules) do not exhibit fluorescence flickering. This observation is corroborated by the stable fluorescence intensity time trajectories of individual molecules of each polymer as shown in Figure 4. 5.

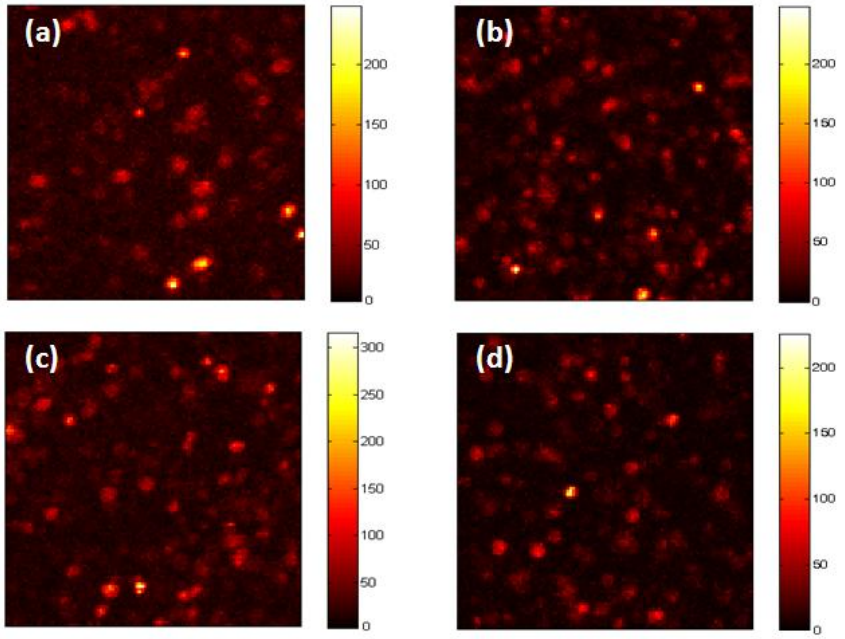

Figure 4. 4 SMS images (scan range: 10 × 10 μm^2) taken at 70 W/cm^2 under 488 nm excitation for (a) P3HT (high MW); (b) PQT-12; (c) PBTTT-14 and (d) PTzQT-12, respectively. Scale bars indicate photon counts per 10 ms.

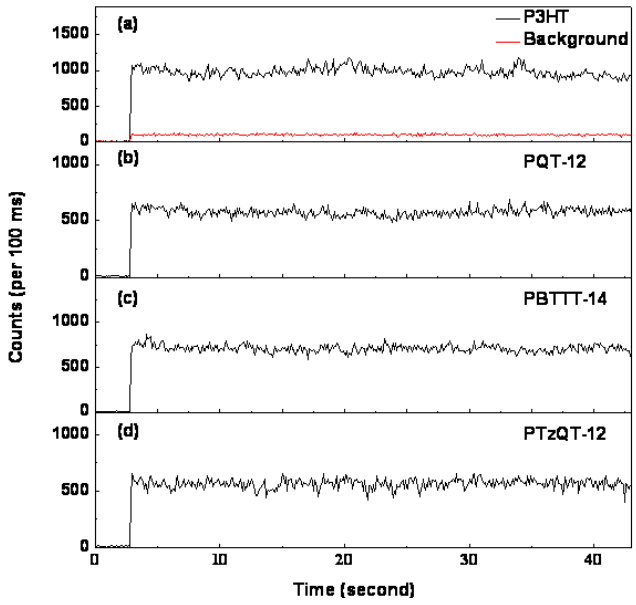

Figure 4. 5 Fluorescence intensity trajectory of a single molecule for (a) high MW P3HT, (b) PQT-12, (c) PBTTT-14 and (d) PTzQT-12 coated with 200 nm thick Al film. In panel (a), the background transient of PMMA film is included as a red curve. All the transients were taken under 488 nm excitation with a power density of 70 W/cm^2 and dwell time of 100 ms.

P3HT single molecule ensemble spectra. Figure 4. 6(a) and (d) shows a comparison of single molecule ensemble spectra of the low MW (investigated in Chapter **3**) and high MW P3HT (investigated herein). Together with each SMS ensemble spectrum, the solution fluorescence spectra are also included as dashed curves. For the low MW P3HT, it is found that the SMS ensemble spectrum has a similar peak wavelength as the solution emission spectrum, which implies that the majority of these single molecules embedded in the inert PMMA film retain the polymer chain conformation in $CHCl_3$ solution, presumably due to the low molecular weight and rigidity. The broad and unstructured SMS ensemble spectra of the low MW P3HT can be attributed to an inhomogeneous broadening of the π-π^* transition due to a wide distribution of emission energies as can be seen in the peak wavelength distribution histogram in Figure 4. 6(b). However, for the high MW P3HT, a strong red shift in the emission of ~ 43 nm has been observed in single molecule ensemble spectra with respect to the corresponding molecular chloroform solution. Similar results also have been observed for poly-3-octylthiophene (P3OT) with a molecule weight of 143 kDa[122] and have been ascribed to the planarization of the polymer backbone and the dominant occurrence of low energy site emission of aggregated conformation in the solid state. As discussed before, these low energy sites are believed to be due to conjugated chain contacts or longer conjugated segment in the collapsed conformation, which cause a local lowering of the exciton energy.[13,69,72]

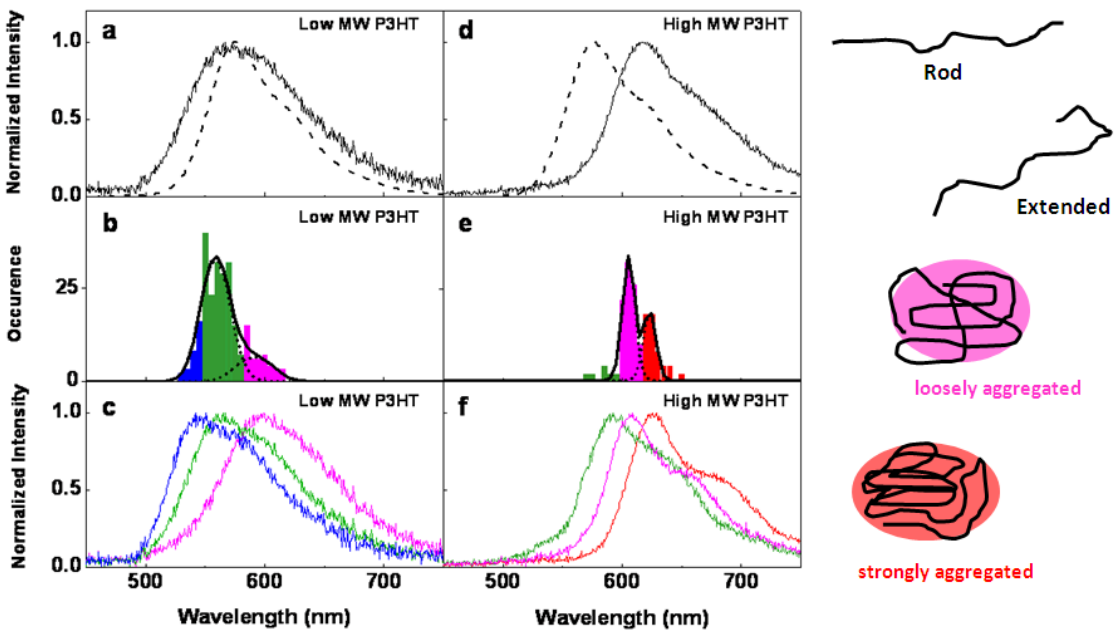

Figure 4. 6 Normalized single molecule ensemble spectra of low MW P3HT (M_n: ~ 7.5 kDa) and high MW P3HT (M_n: ~ 37.5 kDa) are presented as solid curves in (a) and (d), respectively. The dashed lines in (a) and (b) are solution fluorescence spectra used for comparison. Corresponding distribution histograms of SMS peak emission wavelength are shown in (b) and (e), which are fitted with Gaussians (dotted curve). Based on the Gaussian fitting results, the ensemble distributions were split into sub-ensemble distributions, indicated with different colors. *Note that the blue edge for the low MW P3HT sample was split from the bulk of the histogram (green) due to its large blue shift compared to the bulk solution emission maximum.* Panels (c) and (f) depict the normalized sub-ensemble spectra constructed by adding up single molecule spectra with peak wavelengths indicated by the color scheme in the corresponding peak wavelength histograms (panel b and e). For the low MW P3HT, the sub-ensembles were constructed by using 547.5 nm to separate blue and green spectra, while 582.5 nm was used to distinguish between green and purple spectra. While for the high MW P3HT, the sub-ensembles were constructed by using 597 nm to distinguish between green and purple spectra, and 617 nm between purple and red spectra. The cartoons shown in the right depict rod-like, extended, loosely and strongly aggregated conformations that the polymer molecules might take.

P3HT single molecule peak wavelength histograms. Figure 4. 6(b) and (e) display the SMS peak wavelength distribution histograms for low and high molecular weight

P3HT, respectively. For the low MW P3HT, it can be seen that the peak wavelength distribution is broad, which can be explained by a large distribution of emission energies for individual polymer chains. The majority of molecules have their emission peak wavelength close to the emission maximum of the bulk molecular solution. This observation suggests a similar polymer chain conformation in both solution and PMMA film for these molecules. The appearance of SMS spectra on the short-wavelength edge, which are severely blue-shifted with respect to the molecular solution and green sub-ensemble SMS data, is most likely due to emission of molecules with high energy (short conjugation length) P3HT chromophores that may be indicative of the polydispersity of the measured samples. In contrast to the low MW P3HT, the high MW P3HT demonstrates a much narrower peak wavelength distribution (Figure 4. 6(e)), presumably indicative of emissions from a limited number of chromophores due to efficient intramolecular energy transfer. It can be found that a small fraction of molecules (marked with green in Figure 4. 6(e)) are still peaked at ~ 577 nm (peak wavelength of molecular solution). The unexpected presence of this small number of molecules with solution-like emission spectra might be a result from a random and rapid "freezing" of molecular conformation from solution into PMMA film during the spin coating process. As discussed in Chapter **3**, the broad peak wavelength distribution of low MW P3HT actually represents a bimodal distribution of peak wavelengths that is masked by the greater energy disorder in the chromophores[122,144] compared to for

instance MEH-PPV.[69,72] With molecular weight increase in P3HT, more chain packing would be expected therefore leading to more occurrence of lower energy site emission because of intramolecular energy transfer. For the high MW P3HT, a bimodal distribution of peak emission wavelengths corresponding to solution-like (green) and loosely aggregated (purple) chains can be observed, similar as for low MW P3HT. However, the occurrence of molecules with solution-like conformations has significantly decreased, as discussed above. In addition, a third peak in the histogram (red) can be observed that is assigned to emission from polymer chains with strongly aggregated conformation as illustrated in Figure 4. 6.

P3HT single molecule sub-ensemble spectra. The sub-ensemble spectra for low and high MW P3HT shown in Figure 4. 6(c) and (f) are constructed by adding up the single molecule spectra with peak wavelengths indicated by the different colors in the corresponding peak wavelength histograms in (b) and (e), respectively. The ensemble and sub-ensemble spectra of low MW P3HT have been discussed in Chapter **3**, Figure 3. 5(a-c). The data were ascribed to the majority of the molecules retaining a solution-like extended conformation, while a small fraction of the molecules exhibit folding into loosely aggregated chains. In addition, a small fraction of the molecules have blue-shifted spectra compared to the solution-like molecules, which is most likely due to emission of molecules with high energy (short conjugation length) P3HT chromophores. The data for high MW P3HT reveal that only a few molecules exhibit

solution-like emission properties, thus only a few molecules adopt an extended or rod-like conformation (Figure 4. 6). No blue-shifted molecules with short conjugation length chromophores were found. For the red and purple sub-ensemble spectra of the high MW P3HT, we can see that the 0-1 electronic transition intensity distinctly decreases in comparison with the green sub-ensembles of the high MW P3HT as well as all the sub-ensembles of the low MW P3HT. This reminds us of the Huang-Rhys factor ***S***, a measure of the electron-vibration coupling between the ground and excited states, associated to the *n*th active mode. Usually, in the case of a single emitting species ***S*** can be empirically calculated from the ratio of fluorescence intensity of the 0–1 transition to that of the 0–0 transition,[72] i.e.

$$S = \frac{I_{0-1}}{I_{0-0}} \tag{4.1}$$

Previous investigations indicate that ***S*** has been correlated with the conformational disorder of polymer chains and exciton migration in bulk materials, where *smaller* S *indicates longer conjugation length and larger extent of exciton migration in the conducting polymers*.[72,154] It can be clearly seen that for the high MW P3HT single molecules, the ***S*** value decreases for the red and purple sub-ensemble compared with the green sub-ensemble, indicative of a more effective exciton migration and longer conjugation length, i.e. a collapsed and ordered structure (chain folding). Effects of H-aggregation in the partial extinction of the vibronic shoulder for the purple and red sub-ensembles can be ruled out. First, the red and purple spectra do not show a

fluorescence intensity drop compared to the green spectra as would be expected for H-aggregates. Second, both the purple and red sub-ensembles show nearly identical vibronic progression and S factors. However, it has previously been postulated that even the slightest variations in aggregation can lead to significant changes in S factors in the case of H-aggregates.[155] A final observation that warrants discussion is that the data in Figure 4. 6(c) and (f) clearly illustrate that the emission spectra originating from molecules with collapsed conformation have a well-defined vibronic structure compared to the solution-like and low MW P3HT single molecule emission spectra. This observation suggests that emission from molecules with collapsed conformation occurs from only one or a few specific chromophores in the polymer chain. A similar observation has been previously reported for MEH-PPV single molecules.[69]

To further identify the spectral properties of the sub-ensemble spectra at long wavelength range for both the low and the high MW P3HT molecules, additional analysis on the purple sub-ensembles assigned in Figure 4. 6 was completed. As one can see in Figure 4. 7, sub-ensemble spectra of both the low and the high MW P3HT molecules (Figure 4. 7(b)), built with single molecule spectra peaked in the wavelength range of 582.5 to 597 nm, exhibit analogous emission profiles. A slightly broader emission in the short wavelength range for the low MW P3HT is observed, probably due to energetic disorder in chromophores. This observation indicates that the high MW P3HT molecules with emission peaking in the wavelength range of 582.5 to 597

nm (green distribution in Figure 4. 7(d)) probably take on loosely aggregated conformations as opposed to solution-like conformations, especially considering there is a red shift in the sub-ensemble spectrum relative to the solution spectrum. The sub-ensemble spectra collected in the wavelength of 597 to 617 nm of both the low and the high MW P3HT molecules are also similar in terms of spectral shape and vibronic structure, although the former is broader in the short wavelength due to a wider distribution of chromophore energies. This analysis indicates that for the high MW P3HT, the green spectra peaked in the wavelength range of 582.5 to 597 nm (Figure 4. 6(e)) actually belongs to loosely aggregated conformations.

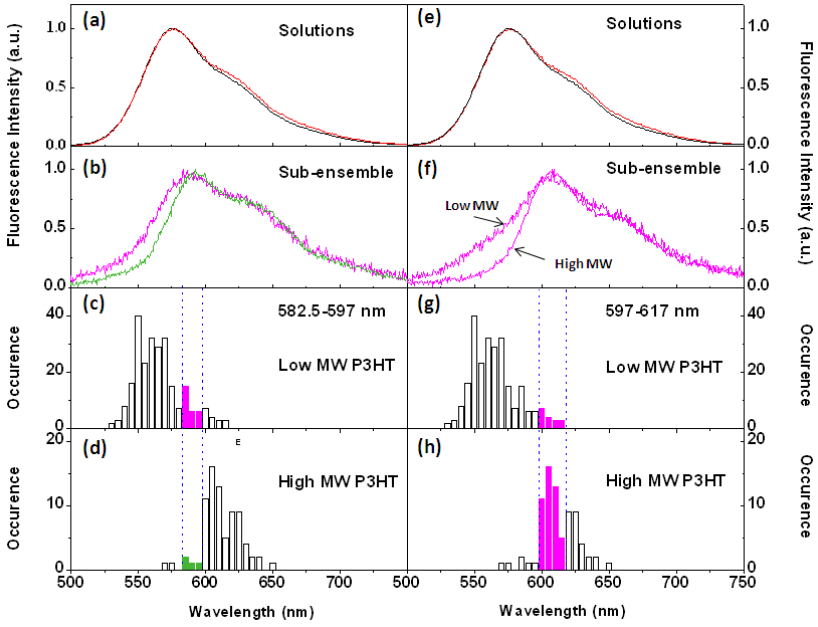

Figure 4. 7 (a) and (e) show the fluorescence spectra of chloroform solutions of the low MW P3HT (black) and the high MW P3HT (red). (b) and (f) display sub-ensemble spectra constructed based on the filled bars indicated in the peak wavelength distribution histograms in (c-d) and (g-h). In (b), the purple and green curves represent the sub-ensembles of the low and the high MW P3HT, respectively. In (f), the sub-ensembles of the low and the high MW P3HT are indicated.

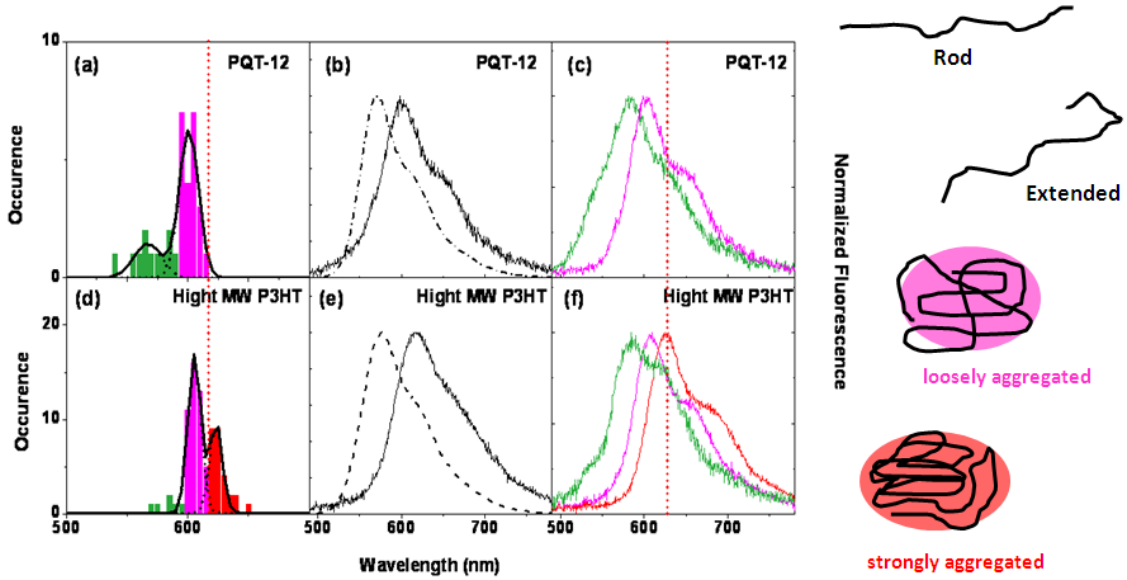

Figure 4. 8 The single molecule spectral data comparison for PQT-12 and P3HT (high MW). (a) and (d) demonstrate the peak wavelength distribution histograms for PQT-12 and P3HT, respectively. The distributions are fitted to Gaussian shapes (dotted curves in (a) and (d)). In (b) and (e), the normalized single molecule ensemble spectra for both polymers are depicted with solid curves while their solution emissions are presented with dashed curves for comparison. Panel (c) and (f) displays the normalized sub-ensemble spectra created according to color schemes indicated based on the Gaussian fitting shown in (a) and (d). The sub-ensembles were constructed by using 593 nm to distinguish between green and purple spectra for PQT-12, while for the high MW P3HT 597 nm and 617 nm were used to distinguish between green and purple spectra, and between purple and red spectra, respectively,. The cartoons shown in the right depict rod-like, extended, loosely and strongly aggregated conformations that the polymer molecules might take.

PQT-12 single molecule (sub-)ensemble spectra. Although PQT-12 and P3HT have analogous thiophene backbone and solution fluorescence spectra, these two polymers exhibit dissimilar single molecule emission features, as depicted in Figure 4. 8(b) and (e). As can be seen, the peak emission wavelength of the high MW P3HT SMS ensemble spectrum is ~ 25 nm red shifted relative to that of the PQT-12 ensemble

spectrum. In comparison with the bi-modal distribution of peak wavelengths for high MW P3HT over the wavelength range of 597 nm to 650 nm (Figure 4. 8(d)), there is only a narrow single modal distribution of peak emission wavelengths from 593 nm to 615 nm in PQT-12 data (Figure 4. 8(a)). This observation can be explained by a possible inhibition of forming a strongly aggregated conformation by PQT-12 chains, while the formation of strongly aggregated chain conformations is believed to be responsible for the red sub-ensemble found for high MW P3HT.[122] In addition, from the peak wavelength distribution histogram of PQT-12, one can see that ~ 33% of single molecules still assume solution-like conformation, i.e. extended or rod-like conformation. This reduction of the occurrence of folded molecules when comparing PQT-12 with high MW P3HT can be explained by a higher rotation energy barrier of inter-ring σ-bond proposed by Liu et al.[141]

PBTTT-14 and PTzQT-12 single molecule (sub-)ensemble spectra. Figure 4. 9(a) and (d) present respective SMS ensemble spectra for PBTTT-14 and PTzQT-12. The molecular solution fluorescence spectra are included as black dashed curves for comparison. As seen for PBTTT-14, the peak wavelength of the single molecule ensemble spectrum is red shifted to ~ 605 nm with an obvious shoulder at ~ 560 nm. The corresponding peak wavelength distribution histogram (Figure 4. 9(b)) exhibits a maximum at ~ 565 nm, which is close to the molecular solution emission maximum at ~ 568 nm, as well as a broad red shifted distribution above 583 nm. These data indicate

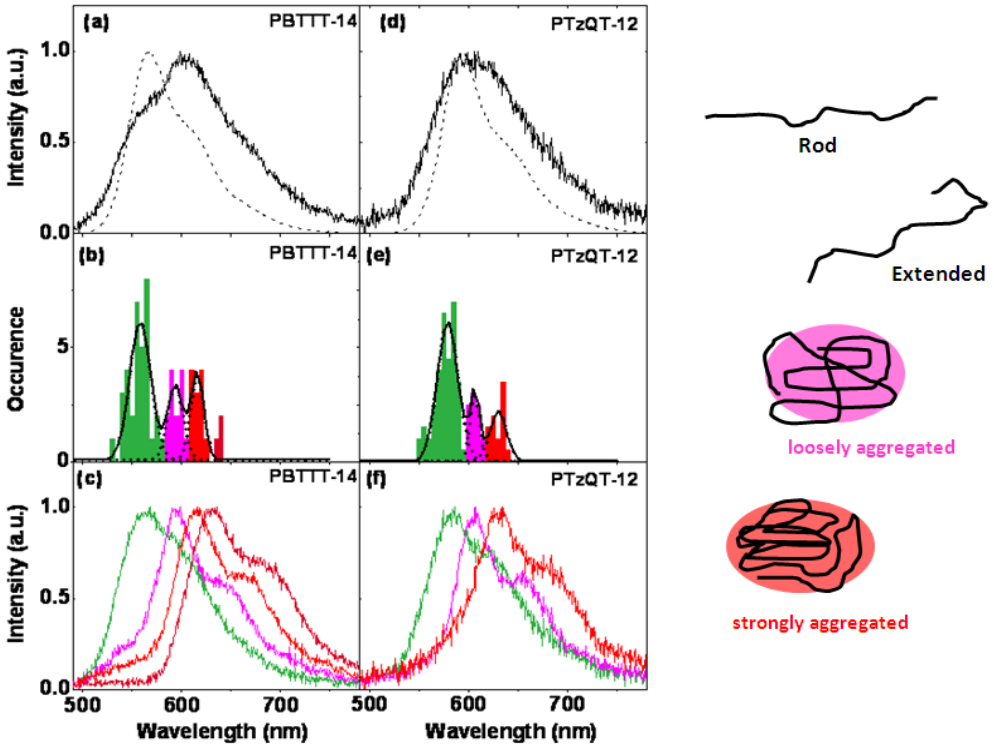

Figure 4. 9 Normalized single molecule ensemble spectra of PBTTT-14 and PTzQT-12 are shown as solid curves in (a) and (d), respectively. The dashed lines in (a) and (b) show solution fluorescence spectra used for comparison. (b) and (e) display corresponding SMS emission peak wavelength distribution histograms, which are fitted to Gaussian curves (dotted). Based on the fitting and the distribution occurrence, the ensemble distributions were split into sub-ensemble distributions with different colors indicated in the histograms (see (b) and (e)). The bottom panels (c) and (f) display the normalized single molecule sub-ensemble spectra constructed according the color schemes in (b) and (e). For PBTTT-14, the sub-ensembles were constructed by using 582.5 nm to distinguish between green and purple spectra, while 607.5 nm was used to distinguish between purple and red spectra. For PTzQT-12, the green and purple sub-ensemble spectra were sorted by 597.5 nm, while the purple and red spectra 617.5 nm was used to distinguish between. The cartoons shown in the right depict rod-like, extended, loosely and strongly aggregated conformations that the polymer molecules might take.

that the single molecule ensemble spectrum of PBTTT-14 is formed by the contribution

from solution-like and aggregated polymer chains. This finding is evident from the sub-ensemble spectra (Figure 4. 9(c)) that were constructed according to the peak wavelengths distribution histogram (Figure 4. 9(c)). As one can see, the green sub-ensemble spectrum is very similar to the solution fluorescence spectrum. Due to a more rigid backbone in PBTTT-14 as a result of a fused thiophene ring, the PBTTT-14 molecule has less conformational freedom compared to high MW P3HT molecules.[108,109] This could explain the strong presence of the green sub-ensemble showing molecular solution like emission characteristics in the SMS data. In addition, as discussed in section 4.2.3 (below), less PBTTT-14 molecules show moderate anisotropy values (0 to ± 0.5), indicating that most molecules have strongly anisotropic rod-like conformations. The appearance of red shifted emission from PBTTT-14 single molecules indicates collapsed conformations for these particular PBTTT-14 single molecules (~ 46% in this case) in the SMS samples. The distribution within the long wavelength range (583-630 nm) can be fitted to two Gaussian shapes (Figure 4. 9(b)). This bimodal distribution resembles that found in high MW P3HT molecules and can be described as loosely and strongly aggregated conformations. Interestingly, the sub-ensemble spectra built from the purple and red distributions exhibit a markedly well defined vibronic structure in which the ratio of fluorescence intensity of the 0–1 transition to that of the 0–0 transition (Equation 4.1) is significantly smaller compared with molecular solution data. The latter observation is analogous to that found for high

MW P3HT, indicating a more effective exciton migration and longer conjugation length, i.e. a collapsed and ordered structure (chain folding). The appearance of defined vibronic structure for the purple and red sub-ensemble spectra is indicative of emission occurring from a limited number of emitters on the chains, again indicating exciton migration to low energy trap sites.[69] A few (three) spectra peaked above 630 nm (deep red distribution in Figure 4. 9(b)) were also found. Close inspection of the individual spectra reveals an absence of vibronic structure in these spectra, while the spectra are dim in intensity and strongly red shifted. Therefore, these spectra are probably originating from nanoparticles rather than strongly aggregated single molecules. Based on the experimental observations discussed herein, PBTTT-14 appears to have a more rigid molecular structure than the high MW P3HT investigated here. The nature of PBTTT-14's molecular conformations is addressed further when discussing polarization anisotropy data in section 4.2.3.

With regard to PTzQT-12, as can be seen in Figure 4. 9(d), the emission maximum of the single molecule ensemble spectrum at ~ 600 nm is close to that of its molecular solution at ~ 593 nm. This observation is very analogous to that demonstrated by the low MW P3HT in Figure 4. 6(a-c). The peak wavelength distribution histogram shown in Figure 4. 9(e) can be fitted to three Gaussians. Corresponding sub-ensemble emission spectra were constructed and are displayed in Figure 4. 9(f). The green sub-ensemble spectrum has its emission maximum at 586 nm which is close to the

solution spectrum emission peak at 593 nm. The bimodal distribution for the red shifted single molecule spectra again is similar to that found in the high MW P3HT and indicates the formation of loosely and strongly aggregated conformations. This finding implies that the majority of PTzQT-12 single molecules adopt a molecular solution conformation with extended or rod-like conformation without low energy sites, while ~ 35% of the molecules form low energy emission sites. For the PTzQT-12 studied herein, the polymer chain consists of approximately 10 repeat units and consequently ~ 50 rings in the backbone (Figure 4. 2). The molecular weight of PTzQT-12 is thus sufficient to observe low energy sites that can be ascribed to π-π stacking between chromophores as shown for single chains of flexible and high molecular weight conjugated polymers.[13] Finally, again the appearance of defined vibronic structure for the purple and red sub-ensemble spectra is indicative of emission occurring from a limited number of emitters on the chains.[69]

To sum up, from the above discussion it is clear that P3HT (high MW) exhibits the highest tendency to form a collapsed (loosely or strongly aggregated) conformation. PQT-12, with a relative rigid polymer backbone due to a higher σ-bond rotation barrier compared with P3HT,[141] displays an absence of emission from strongly aggregated conformations as found in P3HT (high MW), which implies a less collapsed (loosely aggregated) conformation in relation to high MW P3HT. While a planar backbone conformation and a high σ-bond rotation barrier is expected for PBTTT-14[141] SMS data

show that one half of the molecules retain solution-like spectra and the other half exhibit aggregate (loosely and strongly) emission. PTzQT-12, which based on crystal and modeling data exhibits the most rigid polymer backbone, has ~ 65% molecules assuming molecular solution-like spectra and ~ 35% with aggregated emission.

4.2.3 Single Molecule Polarization Anisotropy

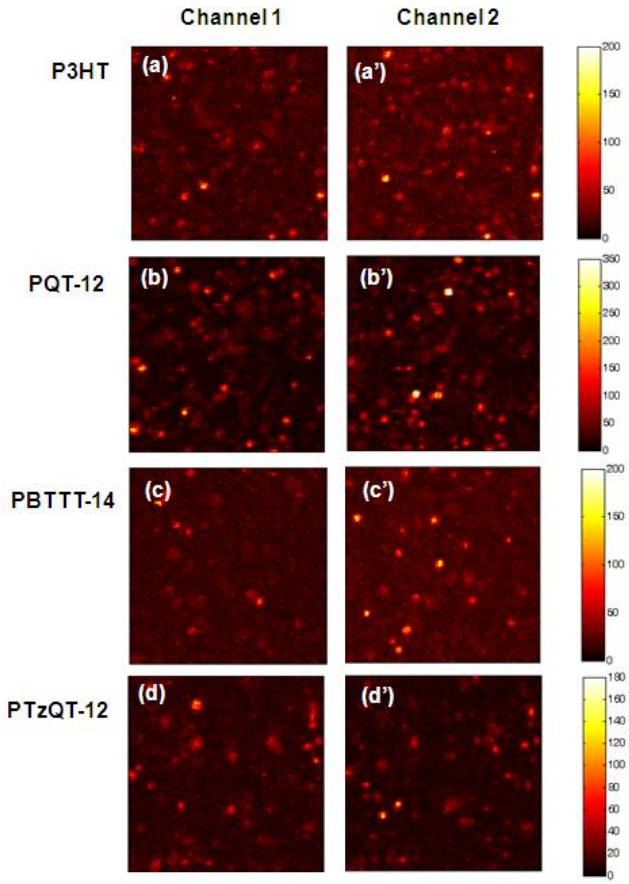

Figure 4. 10 Simultaneously acquired fluorescence images (scan range: 10 × 10 μm^2) at two orthogonal polarization channels under circularly polarized laser excitation at 488 nm for single molecules of the high MW P3HT (a and a'), PQT-12 (b and b'), PBTTT-14 (c and c') and PTzQT-12 (d and d'), respectively. Scale bars indicate photon counts per 10 ms.

In addition to the spectroscopy data fluorescence polarization anisotropy imaging was

also carried out to further understand the conformation of single molecules of these four polymers.[11,75] Figure 4. 10 shows the polarization anisotropy images collected simultaneously at two perpendicular polarization channels for single molecules of the four polymers studied. The corresponding distribution histograms of polarization anisotropy values measured for a statistical ensemble of the polymer molecules are plotted in Figure 4. 11. As can be seen in Figure 4. 11(a), the high MW P3HT molecules exhibit higher polarization ratios with a maximum in the distribution around ± 0.65 compared to ± 0.40 for the low MW P3HT molecules. In addition, the occurrence at low anisotropy values (absolute values less than 0.3) are significantly reduced for the high

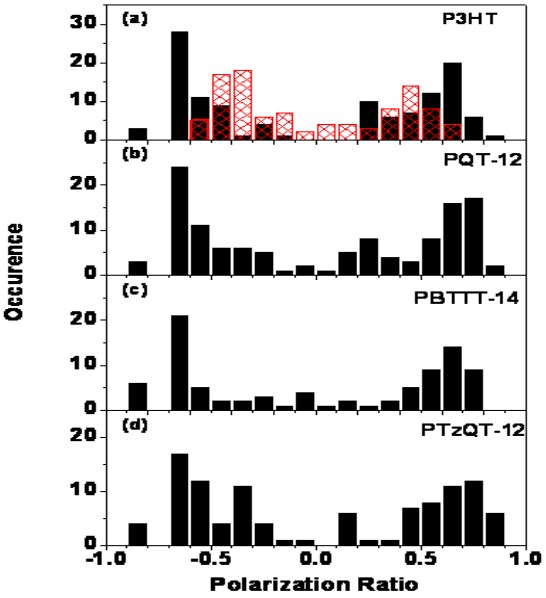

Figure 4. 11 The polarization ratio distribution histograms for (a) P3HTs with high MW (black filled) and low MW (red mesh filled), (b) PQT-12, (c) PBTTT-14 and (d) PTzQT-12, respectively.

MW P3HT molecules with respect to the molecules with low MW. Meanwhile, strongly polarized fluorescence with P value of ± 0.9 was detected for a few molecules in the high MW P3HT sample. The moderately to highly polarized fluorescence can be assigned to emission from single or few chromophores as a result of an efficient energy funneling process, or emission from a chain with a small number of well-defined chromophores.[15] This observation fits well with the single molecule spectroscopic data discussed above, which indicate that nearly all high MW P3HT chains exhibit folding of the polymer chain into loosely and strongly aggregated conformations. Furthermore, this finding of highly polarized emission stemming from limited number of chromophores due to energy funneling also corresponds well with the red shifted single molecule spectra relative to its molecular solution spectrum. The moderate to low polarization values of the low MW P3HT molecules, as discussed in Chapter **3**,[144] have been ascribed to an extended conformation of the polymer chain in which rod-like segments are connected by defects in the polymer backbone.

As shown in Figure 4. 11(b) PQT-12 molecules also exhibit high polarization ratio, analogous to high MW P3HT molecules, but with a slight increase in the distribution in the low polarization ratio range (- 0.45 - + 0.45) relative to the high MW P3HT and PBTTT-14 (Figure 4. 11(c)). The high polarization values observed for PQT-12 can be ascribed to the aggregated polymer chain conformation, as discussed above for high MW P3HT. However, in the case of PQT-12, the single molecule emission

spectra indicate that only loosely aggregated conformations are formed. Furthermore, as can be seen from Figure 4. 8(a), about 33% of PQT-12 single molecules in the SMS sample still retain solution like emission. This observation can explain the presence of low polarization values in the polarization distribution histogram.

PBTTT-14 single molecules also exhibit highly polarized fluorescence. As can be found in Figure 4. 11(c), the polarization anisotropy distribution displays a low occurrence of P values in a broad range of -0.5 to + 0.5, while a large number of occurrences are found towards high polarization values above 0.6. This result together with the red shifted emission observed in the SMS data (Figure 4. 9(a) and (b)) implies an aggregated chain conformation (loosely or strongly aggregated). However, the high polarization ratios are surprising when a 54% occurrence of solution like spectra in the single molecule spectra data is taken into account (Figure 4. 9(a) and (b)). Considering a rigid polymer backbone and a limited number of repeat units, the high polarization anisotropy might mean that PBTTT-14 molecules in the SMS sample showing solution like spectra probably have a rod-like polymer chain with aligned rigid segments connected with a limited number of defects such as σ-bond rotation or imperfect thiophene rings (presence of saturated carbon atoms in thiophene ring).[129-131] This assignment is further supported when taking into account the data obtained for low MW P3HT. In that case, a large number of single molecules

exhibiting solution-like spectra were also observed, but with moderate to low polarization anisotropy values, indicative of kinked polymer chains due to a large number of defects in the backbone and/or rotations around inter-ring sigma bonds. This rod-like conformation of PBTTT-14, however, is distinct from the folded conformation observed in PBTTT-14 nanocrystals growth investigation.[141] This result indicates that backbone rigidness is not the only factor in determining structure of nanocrystals, for which other factors including intermolecular interaction and solvent effects should also be considered.

As shown in Figure 4. 11(d) PTzQT-12 molecules also exhibit high polarization anisotropy but with a small fraction of distribution occurring in the low polarization ratio range. Although the majority (~ 65%) of PTzQT-12 retains a solution like conformation according to the single molecule spectra, the dominant high and moderate polarization anisotropy of PTzQT-12 molecules indicate, for molecules with solution like spectra, a rod-like polymer chain conformation. This observation matches up well the bulk crystal structure analysis result, which revealed that PTzQT-12 chains exhibit non-folding characteristics.

Table 4. 1 summaries and compares the polymer chain folding properties of these four polymers in nanocrystal structure and at the single polymer chain level. These data show that the rigidity and planarity of conjugated polymers can be directed through chemical design and synthesis, however, the non-negligible fraction of rigid and planar

polymer as inferred from crystal and modeling data indicates that conjugated polymer folding is also a function of intermolecular interactions. In other words, an additional factor that needs to be considered are the intermolecular interactions in the solid state that lead to planarization during stacking into crystals and apparent non-folding behavior.

Table 4. 1 Summary of polymer chain folding properties in nanocrystals[141] and at the single chain level based on SMS analysis of the four polymers studied in this dissertation.

Conformation \ Polymers		P3HT (high MW)	PQT-12	PBTTT-14	PTzQT-12
Nanocrystal	Folding	Folding	-	Folding	-
	Non-folding	-	Non-folding	-	Non-folding
SMS	Extended or rod-like	8%	33%	54%	65%
	Loosely aggregated	58%	67%	21%	18%
	Strongly aggregated	34%	-	25%	17%

4.3 Conclusion

The molecular level folding properties of four thiophene-based conjugated polymers including low MW P3HT (non-folding in crystals), high MW P3HT (folding in crystals), PBTTT-14 (folding in crystals), PTzQT-12 (non-folding in crystals) and PQT-12 (non-folding in crystals) were studied and correlated to the chemical structure and rigidness of the polymer backbones using SMS. Single molecule spectra and single molecule polarization anisotropy imaging was completed, and allowed for the

assignment of different conformations to the investigated polymers at the single molecule level. Low molecular weight (M_n: ~7.5 kDa), single P3HT polymer chains in the solid state mostly retain an extended conformation, while high molecular weight P3HT (M_n: ~37.5 kDa) chains almost exclusively fold into aggregated conformations, consistent with the observations made for their respective crystals. PQT-12, although bearing a similar polymer backbone and molecular weight as the high molecular weight P3HT, displays less chain folding relative to P3HT. The polymer PBTTT-14, compared to the high molecular weight P3HT, also exhibits less folding due to a more rigid polymer chain. This finding is in contrast with the observations made for PBTTT-14 in its crystals, which may be due to additional factors aside from chemical architecture, including intermolecular interactions and solvent effects during crystal growth. On the other hand, PTzQT-12 appears to be the most rigid and planar conjugated polymer of these four polymers. However, while PQT-12 and PTzQT-12 exhibit less folding than high MW P3HT, there is still a significant occurrence of chain folding for the polymers at the single molecule level. These findings thus clearly illustrate that the folding properties of crystalline conjugated polymers are not only determined by chemical architecture, but also by stacking interactions in their respective crystals. These single molecule spectroscopy results provide a single molecule level insight into conjugated polymer chain folding properties as a function of chemical architecture and are important for understanding macroscale crystallization behavior.

CHAPTER 5. CORRELATION BETWEEN SPECTROSCOPIC AND MORPHOLOGICAL PROPERTIES OF COMPOSITE P3HT/$PC_{60}BM$ NANOPARTICLES STUDIED BY SINGLE PARTICLE SPECTROSCOPY*

5.1 Introduction

Conjugated polymers have been studied extensively for their application in plastic electronic technologies such as Polymer Light Emitting Diodes (PLEDs), Organic Field Effect Transistors (OFETs) and Organic Photovoltaic Devices (OPVs).[39,57,156-159] Significant progress has been made towards developing commercial products, particularly for PLEDs. OFETs and OPVs, however, have progressed less because these applications depend strongly on the conductivity of the polymer material, which only under specific conditions reaches acceptable values.[39,158,160,161] In the past decades, OPVs with a bulk heterojunction architecture consisting of a blended active layer of conjugated polymer (electron donor) and fullerene derivatives (electron acceptor) have been extensively studied to address such issues.[39,53,57] The bulk heterojunction concept is based on an interpenetrated network of materials at the interface of which ultrafast photoinduced charge transfer can occur, resulting in the formation of free charge carriers.[22,162]

Bulk studies on the active layer of bulk heterojunction OPVs can provide an overall

* This chapter has been published in Hu, Z. J.; Gesquiere, A. J. *Chemical Physics Letters* **2009**, *476*, 51. and Hu, Z. J.; Tenery, D.; Bonner, M. S.; Gesquiere, A. J. *Journal of Luminescence* **2010**, *130*, 771.

evaluation of material properties, but can lead to complex data sets that can be difficult to interpret. For example, impurity trap states in the organic active layer have been shown to mask the true OPV characteristics under certain conditions.[163,164] In addition, ensemble-averaging effects can wash out detailed information on the physical properties and mechanisms that drive material function. The optoelectronic properties of conjugated polymers are highly dependent on polymer chain morphology and polymer chain interactions. On the nanoscale, variations in conjugated polymer chain conformation, packing or aggregation can result in complex heterogeneous materials. Due to the high complexity and heterogeneity of conjugated polymers, it is impossible to achieve a detailed understanding of optoelectronic processes occurring in bulk conducting polymer films. By using Near Field Scanning Optical Microscopy (NSOM) in spin-cast MEH-PPV films, Nguyen et al. revealed a direct relationship between the local optical properties of the film and the nanoscale topography.[84] The investigators demonstrated that the spatially resolved photoluminescence of nanometer-scale topographic features (clusters or bumps) exhibit an enhancement of the red portion of emission relative to spectra of the flat regions, which was attributed to enhanced interchain interactions in these topographic features. Strikingly, since then it has become clear that even the superior optical resolution of NSOM is not sufficient to access all the material's detailed features at the nanoscale. While no significant changes in the spectral properties of different locations in the flat region of the polymer films

were observed with NSOM (typical optical resolution: ~ 50-100 nm), there are now recent reports proving that such areas are made up by domains on the scale of 10 to 30 nm.[109,165,166] Since optical resolution at those length scales cannot be attained on a routine basis, the alternative is to develop NPs of similar size as domains in the materials of interest as samples for in depth studies. These NPs are an intermediate system between bulk films and single molecules, and limit the number of molecules (a few to a few tens of molecules) under investigation while maintaining the required functionality as found for the bulk material. This results in a material system that is representative of the bulk, but simplified enough to be able to complete studies that relate material function to properties at the molecular level.[167-171]

By dispersing these NPs in inert non-fluorescent host polymers at picomolar concentrations these NPs can easily be spatially separated by several microns. This length scale is readily accessible by laser confocal microscopy (typical optical resolution ~ 300 nm), which can be designed to achieve highly efficient photon collection allowing for the detection of fluorescence from single molecules.[13,172-176] Single Molecule/Particle Spectroscopy (SMS/SPS) has proven to be an effective tool to investigate chemical and physical processes of heterogeneous and nanostructured systems. SMS has in fact offered extraordinary insight into the conformational and optoelectronic properties of conjugated polymers as also discussed in Chapters **3** and **4**.[13,68,177,178] By combining the nanoparticle approach with single molecule/single

nanoparticle fluorescence detection we can address one or a few domains at a time compared to bulk films and reveal the domain to domain heterogeneity of properties.

In present work, we developed polymer/fullerene composite NPs consisting of poly-3-hexylthiophene (P3HT) and [6,6]-phenyl C61-butyric acid methyl ester ($PC_{60}BM$) by means of the reprecipitation method.[104,179] This material system was chosen since it represents the current state-of-art in OPVs.[39,57,110] Even though these NPs do not directly relate to the thin film active layers found in bulk heterojunction OPVs, the study of this nanoparticle system with SPS provides us a unique window to probe the properties of conjugated polymers at the nanometer scale upon doping with fullerenes. A particle-by-particle SPS analysis has revealed variations in molecular conformation and aggregation of the conducting polymer chains upon doping with different weight percentages of fullerene, which has implications for the current understanding of the morphological and spectral properties of conducting polymer active layers that find application in bulk heterojunction OPVs.

5.2 Results and Discussion

5.2.1 Results

A. Nanoparticle Morphology and Size

TEM (Transmission Electron Microscopy) and AFM (Atomic Force Microscopy) images of the NPs are shown in Figure 5. 1 and Figure 5. 2, and corresponding diameter

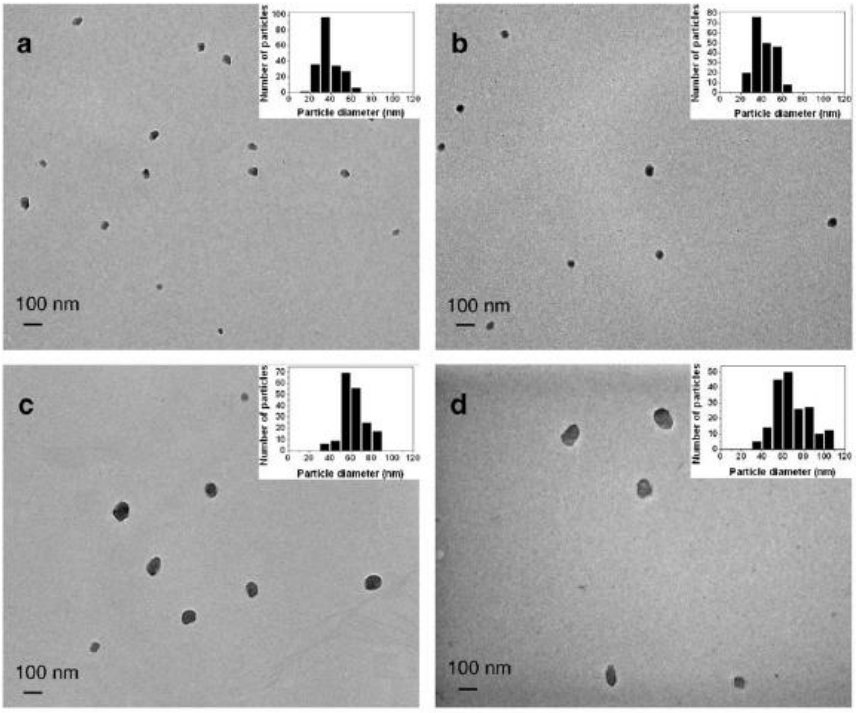

Figure 5. 1 TEM images of (a) undoped P3HT NPs, and composite NPs with (b) 5 wt% $PC_{60}BM$, (c) 50 wt% $PC_{60}BM$ and (d) 75 wt% $PC_{60}BM$ doping levels are shown. The inset in each panel shows the distribution of particle diameters for each sample. Each histogram comprises data for over 150 particles.

Table 5. 1 Summary of data on the size and spectral characteristics of 0 wt%, 5 wt%, 50 wt% and 75 wt% $PC_{60}BM$ doped composite P3HT/$PC_{60}BM$ NPs.

	P3HT nanoparticles with different PCBM content			
	0 wt%	5 wt%	50 wt%	75 wt%
TEM (diameter, nm)	37 ± 9	41 ± 9	62 ± 12	68 ± 17
AFM (height, nm)	8 ± 5	21 ± 10	33 ± 19	36 ± 19
Bulk absorption (λ_{max}, nm)	501	501	498	482
Bulk emission (λ_{max}, nm)	654	652	650	649
SPS excitation power (W/cm^2)	0.72	0.72	3.6	3.6
SPS emission maxima occurrence ratio[a]	3:1	2.5:1	1.4:1	1:1

[a] The ratio of the number of particles with emission maximum at 660 nm to those at 720 nm.

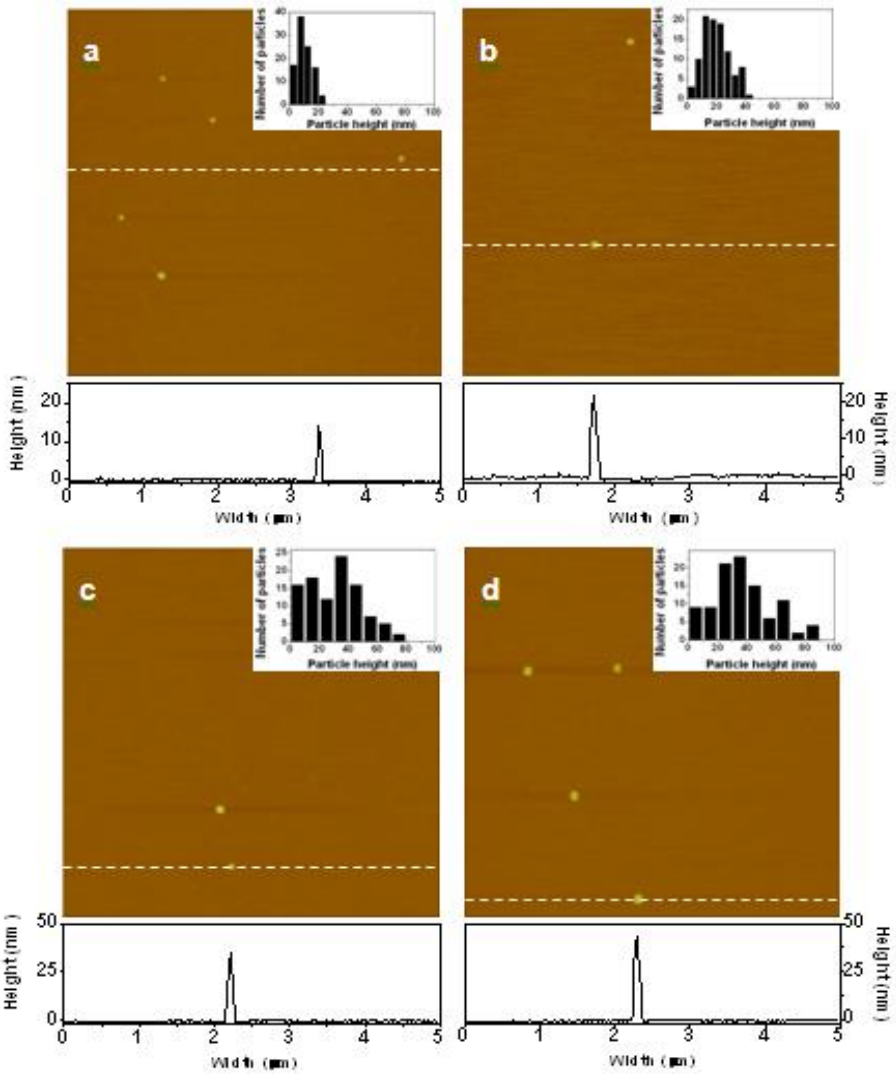

Figure 5. 2 AFM images (scan range 5×5 μm2) of (a) undoped P3HT NPs, and composite NPs with (b) 5 wt% $PC_{60}BM$, (c) 50 wt% $PC_{60}BM$ and (d) 75 wt% $PC_{60}BM$ doping levels are shown. The inset in each panel shows the distribution of particle heights. Each histogram comprises data for over 100 particles. At the bottom of each image, a line scan graph of one of the particles in the image is shown.

and height data for the studied nanoparticle compositions is summarized in Table 5. 1. TEM data indicate an increase in the nanoparticle diameter with increasing $PC_{60}BM$ doping level while a concomitant increase in NP height is also observed in AFM data.

This size increase is attributed to increasing $PC_{60}BM$ aggregation at higher doping levels. The nanoparticle diameter obtained from AFM data is larger than observed in TEM data, which can be attributed to AFM tip convolution.[180] TEM provides a more accurate account of particle diameter and therefore was used to determine particle diameters. Comparing nanoparticle diameter and height, it is clear that the NPs do not appear to be perfectly spherical. Since these NPs consist of soft matter, the aspect ratio could be exaggerated by AFM tip-nanoparticle interactions even when acquiring data in tapping (intermittent contact) mode.[181] Possible deformation caused by the drying process on the mica substrate could be another factor contributing to this observation. Based on the TEM and AFM data the estimated volume of these particles is ~10,000 nm^3. A rough estimate of the volume of collapsed polymer chains of single P3HT molecules is ~ 300-2000 nm^3 given the molecular radii of a collapsed polymer chain in the range of 4-8 nm.[182] Therefore, there are only about 5-40 molecules in each particle. The limited number of molecules makes the NPs an excellent sample for the study of the properties and interactions between molecules in a material at the nanoscale.

B. Bulk solution spectroscopy

Figure 5. 3 presents the UV-vis absorption spectra for P3HT/$PC_{60}BM$ molecular solutions in THF and aqueous nanoparticle suspensions with different weight ratios of conducting polymer and fullerene. The spectra are normalized at the peak absorbance in the visible region of the spectrum. For P3HT molecular solutions in THF, the

absorption maximum is located at 446 nm. $PC_{60}BM$ addition to this solution results in the appearance of an absorption peak at 330 nm that increases in intensity with increasing $PC_{60}BM$ concentration. Compared to molecular THF solutions, there is a strong red-shift of the P3HT absorption maximum for aqueous nanoparticle suspensions (Figure 5. 3). In addition, the absorption maximum of $PC_{60}BM$ doped

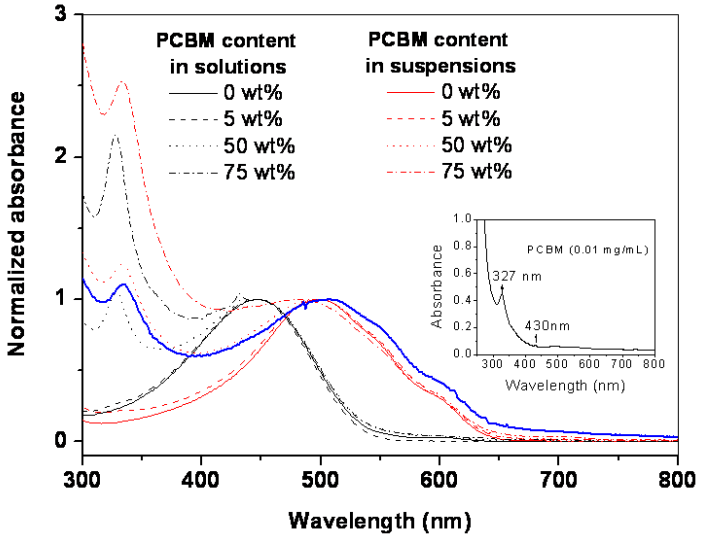

Figure 5. 3 UV-vis absorption spectra of P3HT solutions in THF (black curves) mixed with different concentrations of $PC_{60}BM$ and the corresponding aqueous nanoparticle suspension (red curves) absorption spectra are shown. All THF solutions show the typical P3HT absorption peak at 446 nm, while the characteristic absorption peak of $PC_{60}BM$ appears at 330 nm. For the 5 wt % $PC_{60}BM$ data the $PC_{60}BM$ absorption peak is weak due to lack of sensitivity of the measurement at this low concentration. For clarity an absorption spectrum of neat $PC_{60}BM$ at higher concentration is shown in the inset. An absorption spectrum of a 50 wt% $PC_{60}BM$ doped P3HT film spin cast from DCB solution (taken from Figure 7. 2(a)) is included as a blue curve. This spin cast film exhibits a very similar absorption profile compared with the 50 wt% $PC_{60}BM$ doped nanoparticle suspension, although the former exhibits about 10 nm red shift in absorption maximum relative to the 50 wt% suspension. This comparison indicates that, although the nanoparticle is an intermediate system in between single molecule and bulk film, nanoparticles closely represent the bulk films.

nanoparticle suspensions undergoes a slight blue shift at high $PC_{60}BM$ content with respect to undoped NPs. The shape of the absorption spectra of the mixed P3HT/$PC_{60}BM$ THF solutions and composite nanoparticle suspensions is the superposition of the spectral shape of $PC_{60}BM$ and P3HT, implying that there are no detectable ground state interactions between them. In addition, the absorption spectra of all nanoparticle suspensions exhibit a faint shoulder at 560 nm and a pronounced shoulder at 610 nm, which have also been reported for cast films of polythiophene.[183] It is well-known that the spectroscopic properties of conducting polymers are closely related to the conformation and aggregation of the polymer chains.[184-186] In dilute THF solution, a coil-like conformation of P3HT is present,[187] which is caused by distortion and bending at the C-C bond between adjacent thiophene rings, making the conjugation length shorter and its distribution broad. In fact, this bending at C-C bonds was visualized through STM imaging,[138] However, in the solid state (films or particles), interchain interactions among polymers force the polymer chains to adopt a rather planar conformation that leads to efficient π-π stacking between adjacent polymer chains.[188] As a result, polymer chains become more extended, have limited flexibility and rotations, and thus show an increased conjugation length with corresponding red shifted absorption spectrum as well as the appearance of vibronic structure. In addition, the composite NPs with 50 wt% and 75 wt % $PC_{60}BM$ doping levels show a slight blue shift of the absorption maximum with respect to the absorption maximum of undoped

(0 %wt $PC_{60}BM$) NPs. This observation is attributed to the presence of $PC_{60}BM$ molecules resulting in a reduction of P3HT interchain interactions, and inducing coiled polymer chain conformations with increased kinking and bending of the backbone.[184,189-191]

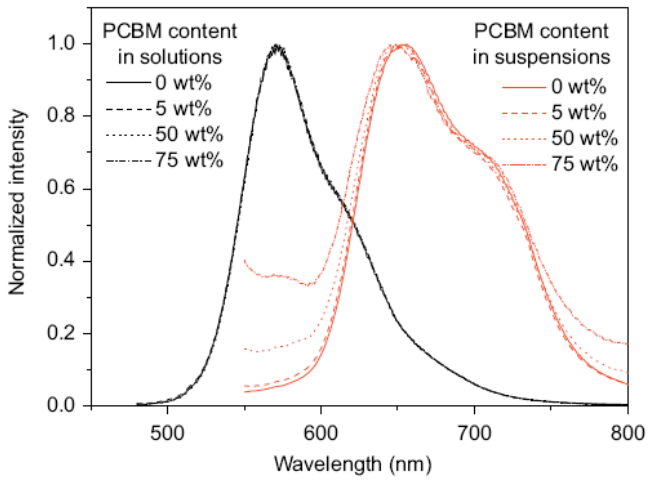

Figure 5. 4 Normalized bulk solution fluorescence spectra of THF solutions of P3HT mixed with different concentrations of $PC_{60}BM$ and the corresponding nanoparticle fluorescence spectra in water are shown in this graph. THF solutions are represented with black curves, nanoparticle suspensions in water with red curves.

Figure 5. 4 shows normalized fluorescence spectra for the THF solutions of P3HT with different $PC_{60}BM$ concentrations, excited at the absorption maximum. All the spectra have emission maxima located at 570 nm and show identical vibronic structure. Since the emission intensity of all these THF solutions remains unchanged at constant P3HT concentrations, we conclude that there is no detectable charge transfer interaction between P3HT and $PC_{60}BM$ at the concentrations used in the reported experiments. A

large red shift (~ 80 nm) in the emission maxima is observed for nanoparticle suspensions with respect to the THF solutions. This red shift can be ascribed to both intra- and interchain interactions leading to fast energy transfer to low-energy chromophores,[122] which is also extensively reported in spectroscopic studies of the conjugated polymer MEH-PPV.[192-194] The emission peak for undoped NPs is located at 654 nm with a shoulder visible at 720 nm. For composite NPs with varying $PC_{60}BM$ content the fluorescence spectral shape remains unaffected, but $PC_{60}BM$ induced fluorescence quenching occurs. Compared to undoped (0 wt% $PC_{60}BM$) P3HT NPs, the fluorescence intensity of composite NPs with 5 wt%, 50 wt% and 75 wt% $PC_{60}BM$ is quenched by factors of 1.6, 4.9 and 8.5, respectively. This quenching can be attributed to efficient charge transfer from P3HT to $PC_{60}BM$ leading to fast non-radiative decay of the optically excited state. Light-induced electron spin resonance studies have shown that spin signal from electrons present in charge separated states can be detected in conjugated polymer/fullerene blends.[22,195] Besides charge transfer quenching of fluorescence we also observe aggregation quenching for the NPs. The fluorescence intensity of undoped P3HT nanoparticle suspension decreases two orders of magnitude compared to that of THF solutions that were prepared to have the same P3HT absorbance at the 488 nm excitation wavelength (Figure 5. 5). This observation is ascribed to the low fluorescence quantum yield (~ 0.02 for P3HT film[148,196]) of the interchain excitations formed in P3HT aggregates.

Polaron formation from a higher excited state upon light absorption could also contribute to the observed quenching of P3HT in nanoparticle form. The latter mechanism has been suggested to work in direct competition to the formation of an emissive state, rather than as an indirect formation of quenchers through a charge separated state.[148]

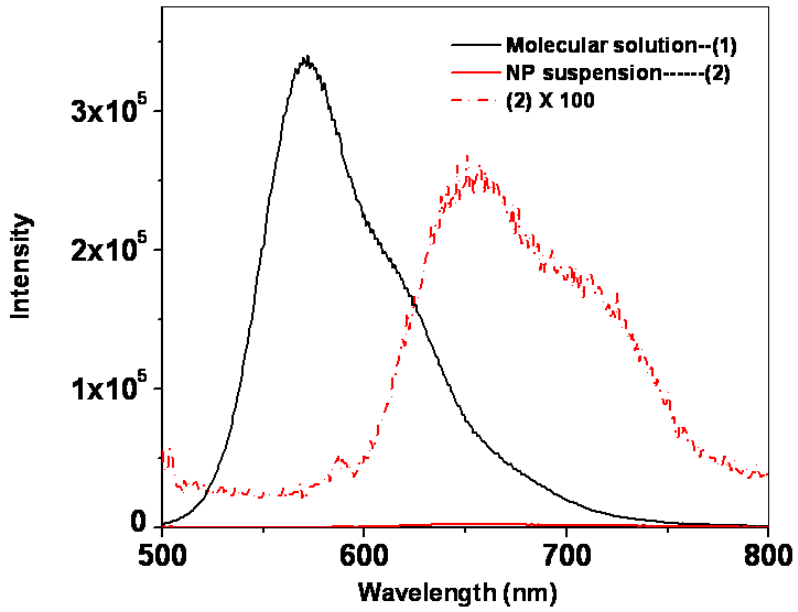

Figure 5. 5 Fluorescence spectra of THF solution of P3HT (black curve, (1)) and aqueous suspension of P3HT nanoparticles (solid red curve, (2)) collected under 488 nm excitation. Note that at 488 nm, these two samples have similar absorbance. The dashed red curve shows the fluorescence spectrum of the nanoparticle suspension multiplied by 100 times for guidance and comparison.

C. Single particle imaging and spectroscopy

The single particle fluorescence properties were investigated by sample scanning laser confocal fluorescence microscopy. Figure 5. 6 shows typical single particle fluorescence images of undoped and 50 wt% $PC_{60}BM$ doped P3HT NPs acquired with

excitation of the sample by 488 nm laser light. For undoped (0 wt% $PC_{60}BM$) and 5 wt% $PC_{60}BM$ doped P3HT NPs ~ 0.72 W/cm^2 of laser excitation was applied for data collection (with slightly lower detected count rates for the 5 wt% doped NPs) while the 50 wt% and 75 wt% $PC_{60}BM$ doped NPs required a five-fold increase in excitation

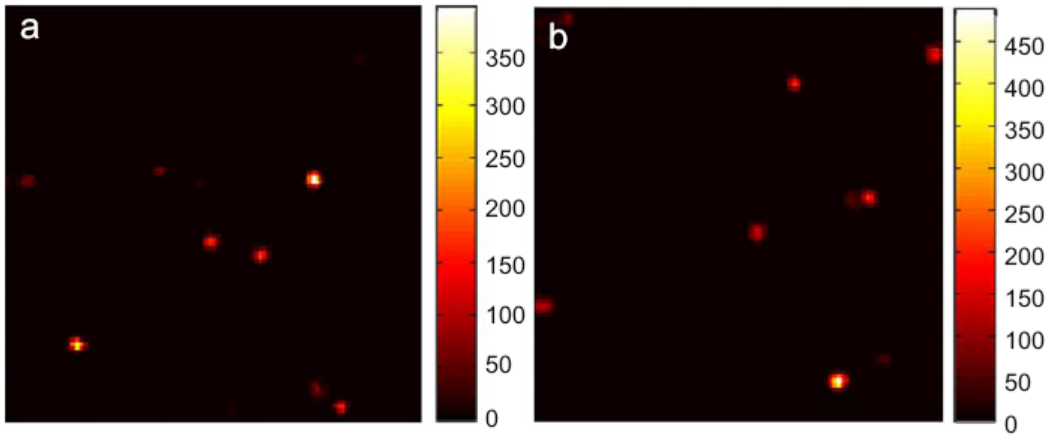

Figure 5. 6 Single particle fluorescence images (10 × 10 μm^2) collected under 488 nm excitation from an Ar^+ laser are depicted. (a) Single particle fluorescence image of undoped (0 wt% $PC_{60}BM$) P3HT NPs under 0.72 W/cm^2 laser excitation. (b) Single particle fluorescence image of 50 wt% $PC_{60}BM$ doped NPs under 3.6 W/cm^2 laser excitation. The excitation intensity was increased by a factor of five to obtain similar photon count rates for 50 wt% $PC_{60}BM$ doped NPs compared to undoped (0 wt% $PC_{60}BM$) NPs, suggesting effective quenching of the P3HT fluorescence due to charge transfer from P3HT to $PC_{60}BM$ in the composite NPs.

power to achieve comparable emission count rates as the undoped (0 wt% $PC_{60}BM$) NPs, indicative of effective quenching of P3HT fluorescence by $PC_{60}BM$ present in the composite NPs. It is however important to realize that the fluorescence of conjugated polymers is quenched by $PC_{60}BM$ due to ultrafast charge transfer from the conjugated polymer (electron donor) to the fullerene (electron acceptor). Previous studies by

Heeger et al.[22,197,198] have shown that this is a dynamic quenching process. Piris et al. have shown that the fluorescence lifetime reduces from 660 ps in pure P3HT to 40 ps for P3HT/$PC_{60}BM$ (weight ratio: 1:1) composite film.[199] These reports indicate that P3HT molecules near $PC_{60}BM$ that are being quenched still contribute to the detected fluorescence signal, given that every time a molecule is cycled to the excited state it has some probability of decaying radiatively as opposed to transferring an electron to $PC_{60}BM$. In addition, at high doping levels such as 50 and 75 wt% $PC_{60}BM$ it is reasonable to assume that only few polymer molecules will not be interacting with $PC_{60}BM$, especially considering that there is no observable phase separation in as-cast P3HT/$PC_{60}BM$ (weigh ratio: 1:2) film according to the work reported by Nguyen et al.[200]

Single particle fluorescence spectra were collected by moving individual NPs into the focused laser beam by means of a piezoelectric stage. Figure 5. 7 depicts the single particle ensemble spectra normalized at 660 nm for NPs with 0, 5, 50, and 75 wt% $PC_{60}BM$ doping levels. For the four nanoparticle compositions reported in this manuscript the "single particle ensemble spectra" shown in Figure 5. 7(a) were constructed by averaging ~900-1000 nanoparticle spectra (spectra were taken and averaged for ~900-1000 individual NPs for a given composition). Two emission maxima of nearly equal intensity located at 660 nm and 720 nm can be observed. For all samples the ensemble spectrum emission maxima remains at 660 nm, however, the

intensity of the emission peak located at 720 nm approaches that of the 660 nm peak with increasing $PC_{60}BM$ doping levels.

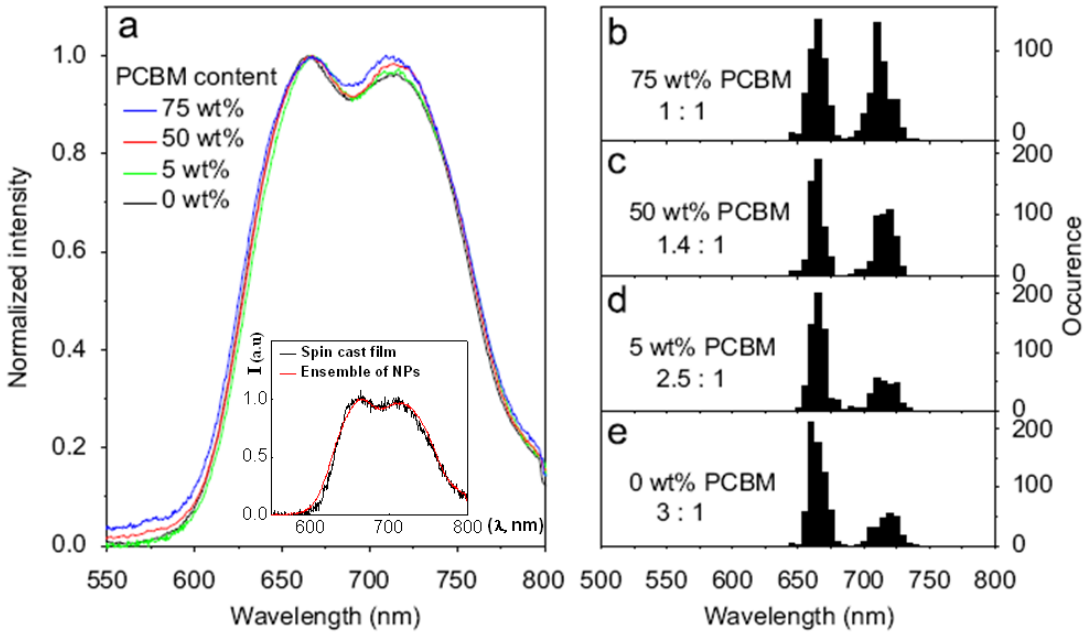

Figure 5. 7 (a) Single particle ensemble fluorescence spectra are shown for the different nanoparticle compositions that were studied. The spectra are normalized at 660 nm. (b)-(e) Histograms representing the distribution of peak emission wavelengths for individual NPs are shown for samples with different $PC_{60}BM$ doping levels. The inset figure in (a) depicts the ensemble fluorescence spectra (taken with LCSM) of the undoped P3HT nanoparticles (red) and a pure P3HT film (spin cast from 2.5 mg/mL THF solution at 1000 rpm for 1 minute). As can be seen, these two spectra almost overlap, indicating that nanoparticles closely represent the bulk films.

Peak wavelength histograms for the ensembles of individual NPs were constructed and reveal a bimodal distribution with peaks at 660 nm and 720 nm (Figure 5. 7(b-e)). Bimodal distributions of peak emission wavelength histograms haven previously been reported for single molecule studies of single dye and single conjugated polymer molecules.[69,122,201-204] In these cases the observations came about due to conformational

changes of the single molecules themselves. The bimodal distributions of peak emission wavelengths reported here are however dominated by changes in intermolecular interactions. Interestingly, as can be seen in Figure 5. 7(b-e) with increasing $PC_{60}BM$ doping levels the occurrence of single particle emission spectra with maximum at ~720 nm increases. The occurrence ratio of spectra with 660 nm peak wavelength to those with 720 nm peak wavelength changes from 3:1 for undoped (0 wt% $PC_{60}BM$) NPs to 2.5:1, 1.4:1 and 1.1:1 for 5 wt%, 50 wt% and 75 wt% $PC_{60}BM$ doped NPs, respectively. Since these data show a clear effect of the $PC_{60}BM$ doping level on the P3HT spectral properties, but only present a simple binary counting of which of the two local maxima is greater than the other we also completed an analysis where the relative intensities of the emission peaks are taken into account. We considered both the 720 nm versus 660 nm peak ratio (denoted as ISP_{720}/ISP_{660}, with ISP the Intensity of a Single Particle at the respective peaks, see Figure 5. 8) of emission spectra for each individual nanoparticle spectrum in the four samples (0, 5, 50, and 75 wt% $PC_{60}BM$), as well as the 720 nm versus 660 nm peak ratio of sub-ensemble emission spectra for the four samples (denoted as ISE_{720}/ISE_{660}, with ISE the Intensity of a Sub-Ensemble at the respective peaks, see Figure 5. 9). The results for the ISP_{720}/ISP_{660} analysis are shown in Figure 5. 8 as ISP720/ISP660 intensity ratio histograms. Given our choice of definition, for spectra peaked at 660 nm the ratios are less than 1, while for spectra peaked at 720 nm the values are larger than 1. The histograms show that the peak of the

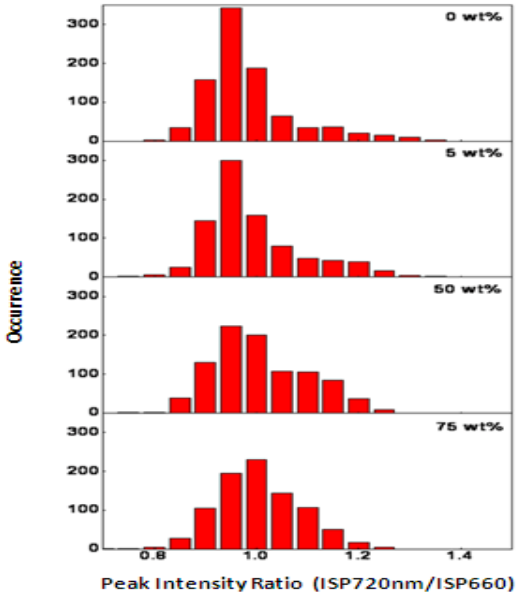

Figure 5. 8 Peak intensity ratio (ISP720/ISP660) histograms of NPs are presented for 0, 5, 50, and 75 wt% $PC_{60}BM$ doped composite NPs.

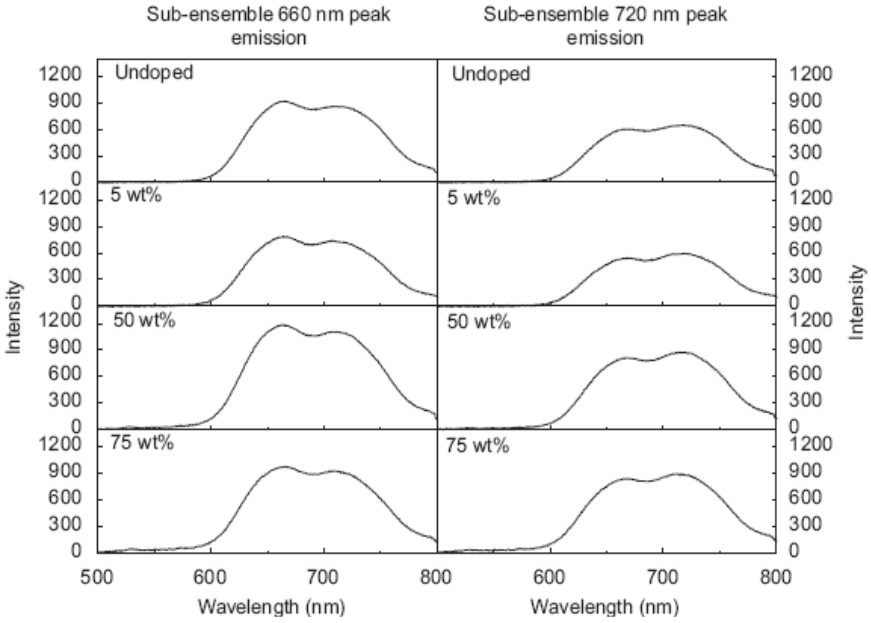

Figure 5. 9 For a given nanoparticle composition the emission spectra of the NPs in an ensemble were sorted according to the emission maximum (660 nm (left column) and 720 nm (right column)). The sub-ensembles with peak emission at 720 nm increase in intensity with increasing $PC_{60}BM$ doping level with respect to the sub-ensembles with peak emission at 660 nm. The ISE_{720}/ISE_{660} ratios are 0.70, 0.77, 0.74, and 0.91 for 0, 5, 50, and 75 wt% $PC_{60}BM$ doped composite NPs, respectively.

distribution shifts from less than one to one, confirming the increasing occurrence of emission with maximum at 720 nm. This observation obviously corresponds with the peak wavelength histograms in Figure 5. 7(b-e). An additional observation however, although the effect is small, is that for samples with low weight percent of $PC_{60}BM$ there are a number of occurrences of the ISP_{720}/ISP_{660} ratio above 1.2, while there are only few for the high weight % $PC_{60}BM$ samples, especially at 75 wt % $PC_{60}BM$, indicative that the variation of $PC_{60}BM$ concentration may play a role in the observed phenomena. This is confirmed unambiguously when considering sub-ensemble spectra. The sub-ensemble spectra were constructed by averaging the individual nanoparticle spectra as described above for a given sample after first sorting the individual nanoparticle spectra based on their emission maximum by using 690 nm as the sorting criterion to distinguish between the spectra peaked at 660 nm and 720 nm. It is important to realize that the sub-ensemble spectra in Figure 5. 9 as such represent the averaged single particle spectral shape and intensity under identical optical conditions for both types of spectra for a particular nanoparticle sample. These unnormalized data show that the contribution at 720 nm increases with $PC_{60}BM$ doping levels relative to the 660 nm emission, an observation that becomes particularly pronounced at high $PC_{60}BM$ doping levels.[205]

5.2.2 Discussion

NPs as a simplified model system for bulk films

The conjugated polymer/fullerene composite NPs in this study have a limited number of molecules (a few to a few tens of molecules). This leads to a material system that is representative of the bulk, but simplified enough to be able to complete studies that relate material function to properties at the molecular and nanometer scale. It is important to know to what extent these NPs are representative of the bulk films. In Figure 5. 3, an absorption spectrum of a 50 wt% $PC_{60}BM$ doped P3HT bulk film is presented in comparison with the absorption spectra of the 50 wt% $PC_{60}BM$ doped P3HT NP suspension. As can be seen, the NP suspension exhibits a very similar absorption profile as the bulk film despite, although there is a slightly red shift (~ 9 nm) in the absorption emission maximum for the bulk film relative to the NP suspension. In addition, as shown in Figure 5. 7, the ensemble spectra collected for both the bulk P3HT film and the pure P3HT NPs using the LCSM are almost overlapped. These observations indicate that the ensemble properties of the NPs are very close to those of the corresponding bulk films. As discussed above, the unique advantage of the NPs material system relies on simplifying the investigations that can relate material function to properties at the nanometer level.

Single particle spectra data interpretation

Changes in relative spectral peak intensities have been extensively considered in the conducting polymer field for the PPV and polythiophene family of conducting polymers and have been related to polymer chain packing and intermolecular

interactions. For PPV type polymers the assignment of the observed spectral shape to vibronic structure has been clearly invalidated.[206-209] Instead, the spectral shape has been shown to be a superposition of two emitters, an excitonic (intrachain singlet) emitter and an aggregate emission at lower energy that has its vibronic 0-0 origin near the 0-1 transition of the excitonic emitter. For polythiophenes the discussion in the field has been whether the PPV description (superposition of excitonic and aggregate emission) also holds true in this case. Brown et al. [210] have reported that modeling of polythiophene spectra based solely on a single intrachain exciton coupled to a single phonon mode does not correctly fit with spectra of highly ordered P3HT. Instead, the investigators invoke the PPV description to explain the absorption and emission spectral features of ordered P3HT. In contrast, recent reports have shown for highly organized oligomers and regioregular polymers that the excitonic emission is forbidden from the lowest energy state, and occurs from an allowed higher energy state where the energy difference with the lower state is given by the Davydov splitting, in other words the molecules form H-aggregates with perfect alignment of the molecules in a parallel face-to-face fashion.[155,211,212] For these particular systems it was suggested that the emission spectra present pure vibronic progression for which differences in relative intensities are related to the sensitivity of the 0-0 vibronic transition to long-range order given that the 0-0 vibronic transition is forbidden for an H-aggregate state, but becomes partially allowed if disorder appears.[155,211,212] The investigators thus conclude that

spectra for highly organized thiophene oligomers and regioregular polymers consist of a single emitter, which is the aggregate and not the intrachain singlet. Here, it is critical to realize that in this description a crystal structure with a single molecule per unit cell is considered.

The situation is most likely quite different for composite P3HT/$PC_{60}BM$ materials such as the composite NPs under investigation here. First, we are dealing with a blended material system. It is therefore reasonable to assume that the polymers will not show a perfect alignment of the molecules in a parallel face-to-face fashion, nor should we expect to see a single crystal type arrangement such as that observed, for example, in sexithiophene with a single molecule per unit cell throughout an entire nanoparticle. There are numerous papers reporting data showing that these materials more often than not have two or four molecules per unit cell.[213-215] The polymer structure in the nanoparticle is therefore expected to be a combination of ordered P3HT chains in domains, where in the domains there are packing defects, including polymer chain folding as opposed to perfectly stretched out polymer chain arrangements, and potentially less ordered regions at, for instance, domain boundaries. As such, the requirements imposed in order to observe strong PL emission effects on the 0-0 transition are most likely not strictly applicable to our case, which was already speculated previously.[155,211,212] Second, the data in Figure 5. 9 *show that it is the contribution to emission spectra at 720 nm that increases with $PC_{60}BM$ doping levels*

relative to the 660 nm emission, whereas the 660 nm emission would increase due to increased disorder with increasing $PC_{60}BM$ doping levels if this were a true 0-0 vibronic peak of a single H-aggregate emitter. That observation is further corroborated by Bolognesi et al., who confirmed the presence of two different crystal structures with XRD and NMR and concurrently also observed an increase in the emission intensity of the lower energy crystal structure with annealing.[205]

The most apparent explanation for the observed SPS data is then that the addition of $PC_{60}BM$ leads to a change in crystallinity of the P3HT polymer material, where two crystalline aggregates have a change in occurrence that has a concentration dependence with respect to $PC_{60}BM$ in the P3HT/$PC_{60}BM$ composite NPs. This change is reflected by the respective contributions of the two aggregate emitters to the overall emission spectrum. Indeed, Sundstrom et al.[216] have given *unambiguous experimental evidence showing that emission from two types of interchain aggregates of polythiophene polymers exists*, with energies similar to the ones we report, further supporting our interpretation of the reported data. Emission peaks in the 650-680 nm and 720-740 nm regions were previously reported for polythiophene powder and film. These emission peaks have been assigned to two distinct crystalline packing structures.[205,217] The most common crystalline structure (denoted as Type I) is the well-known lamellar structure in which the polymer backbones are stacked in a parallel fashion, and spaced by alkyl side chains that have minimal to no interdigitation. The polythiophene backbones in

this particular crystalline packing structure are spaced by approximately 3.8 Å and thus the arrangement is ideal for efficient π-π stacking. This dense pi-stacking arrangement is facilitated by the fact that the alkyl chains exhibit a strong tilt with respect to the stacking direction in Type 1 crystal structures. That arrangement precludes interdigitation of the alkyl side chains of neighboring pi-stacks. As a result, a strong red shift is observed in bulk fluorescence spectra collected for solid state material. The other emission peak corresponds with a crystalline packing structure where the polymer also forms lamellar structures (denoted as Type II). The crucial difference between Type II crystal structures and Type I crystal structures is that the alkyl side chains are tilted to a lesser degree. As a result, interdigitation between the alkyl side chains of neighboring pi-stacks occurs. This arrangement leads to an increase in π-π stacking distance between the polythiophene backbones to approximately 4.5 Å. As a result only a limited interchain π-system overlap can occur, which is reflected in a smaller observed red shift in bulk fluorescence spectroscopy. Given the strong interchain interactions and rod like features of P3HT polymer chains, we assume that intermolecular aggregates with strong interchain interactions, i.e., as described above, account for the majority of polymer chains in the NPs. However, the hydrophobic interaction between the polymer backbone and water can also yield polymer chains with a collapsed conformation (discussed further below).[218,219]

With the introduction of $PC_{60}BM$ in the P3HT NPs, the packing structures of P3HT can

be expected to be significantly affected. Literature reports have shown that the $PC_{60}BM$ molecules intersperse in between individual lamellae in crystalline P3HT aggregates.[220,221] It is therefore most likely that the presence of $PC_{60}BM$ will hinder the interdigitation of the alkyl side chains of neighboring pi-stacks, which then most likely leads to an increase in the tilt of the polymer side chains. As a result, the formation of Type I aggregation states is expected to be favored with increasing doping levels, which is feasible given that annealing of bulk films leads to similar observations.[205] It has previously been shown that Type II packing structures can be transformed to Type I packing structures while in the solid state.[205,217] Based on the discussion given above, the modification of the nanoparticle structure resulting in less Type II domains and more Type I domains can explain our experimental observations. The assignment of increasing occurrence of single particle spectra with 720 nm peak emission to a $PC_{60}BM$ induced change in polymer chain packing to an arrangement that is consistent with Type I domains is also corroborated by the observation that NPs of the same samples but with peak emission at 720 nm instead of 660 nm are dimmer. This is indicative of closer face-to-face π-stacking distances given that according to literature such a closely stacked P3HT structure can support poorly-emissive excimers that result in a lower observed quantum yield of fluorescence and thus a lower fluorescence intensity.[188]

While the model of two aggregate emitters discussed above clearly explains the

observed data, additional factors need to be considered. First, the NPs increase slightly in size as the $PC_{60}BM$ doping level increases (see Table 1). Size-dependent spectroscopic properties for NPs fabricated from substituted polythiophenes have been reported.[170] The size dependence was attributed to the surface layer containing coil-like and distorted conformation type polymer chains, while the inner region of the NPs was proposed to consist of an ordered phase with more planar conformations of the polymer chains. With increasing nanoparticle size, the relative amount of surface layer decreases but that of inner ordered region increases, therefore leading to a red-shifted emission originating from a larger contribution from the nanoparticle core. This possibility cannot be unambiguously ruled out, but for the experiments reported in this paper a more gradual red shift with increasing particle size would be expected, rather than a bimodal distribution of peak wavelengths.

Second, Geng et al. have recently reported that single-walled carbon nanotubes can enhance crystallinity of P3HT in photovoltaic devices, which is ascribed to π-stacking interactions between polymer and nanotube.[222] Given its small size and spherical shape $PC_{60}BM$ and its aggregates do not appear to have the potential to pre-orient polymer chains for growth of a highly organized material.

Finally, besides the formation of crystalline domains with extended closely packed chains, certain polymer chains may also adopt a collapsed coiled conformation. In this conformation the polymer chains can π-stack onto themselves to form intrachain

contacts. These contacts have been shown to lead to red shifted emission for single polymer molecules and are referred to as red sites.[13,72,122] This possibility is likely to occur in addition to the formation of highly organized/stacked structures.

5.3 Conclusion

Composite organic NPs composed of poly-3-hexylthiophene (P3HT) and [6,6]-phenyl C61-butyric acid methyl ester ($PC_{60}BM$) were successfully prepared via the reprecipitation method. These NPs are an intermediate system between bulk films and single molecules, but have a reduced complexity and heterogeneity compared to the bulk material by limiting the number of molecules under investigation. The NPs however maintain the expected functionality as found for the corresponding bulk material.

Based on individual nanoparticle fluorescence data obtained from SPS analysis new observations were revealed that were masked in the bulk spectroscopy. Two emission peaks are observed in single nanoparticle emission spectra located at 660 nm and 720 nm that have been assigned to crystalline aggregates of P3HT with a longer (Type II) and shorter (Type I) π-stacking distance leading to the observation of a higher and lower energy emitter, respectively. The relative intensities of the two observed emission peaks progressively change in favor of the 720 nm peak due to an increase of the intensity of the 720 nm peak (i.e. lower energy emitter) with increasing $PC_{60}BM$ doping

levels. Increasing $PC_{60}BM$ concentration in the composite P3HT/$PC_{60}BM$ NPs thus results in a favored formation of domains with close π- π stacking between thiophene units. The reported data unambiguously show that the changes in spectral shapes for the P3HT/$PC_{60}BM$ blended material system as investigated here cannot be explained by suppression of higher energy emission due to the formation of H-aggregates with increasing order of the polymer chains (i.e. not due to a change in vibronic structure of a single aggregate type emitter), but are the result of two aggregate emitters.

CHAPTER 6. CHARGE TRAPPING AND STORAGE BY COMPOSITE P3HT/$PC_{60}BM$ NANOPARTICLES INVESTIGATED BY FLUORESCENCE-VOLTAGE/SINGLE PARTICLE SPECTROSCOPY

6.1 Introduction

Since the introduction of the conjugated polymer/fullerene bulk heterojunction (BHJ) concept over a decade ago,[22] the past decade has witnessed a burgeoning of research in the field of organic photovoltaics (OPVs).[20,59,223] The BHJ structure has also been employed as the active layer in *ambipolar* organic field effect transistors (OFETs) to provide both p- and n-channel functionality in the same device.[224-226] The primary photoexcitation in conjugated polymers is a Coulombically bound electron-hole pair (exciton) due to the low dielectric constant and significant electron-phonon interaction in organic materials.[21] When blended with electron acceptors such as fullerene, an ultrafast electron transfer process from the polymer (donor) to fullerene (acceptor) generates a charge transfer state (charge-transfer exciton), which can further dissociate into free charge carriers (hole and electron polarons) or recombine back to the ground state.[21,227] Considering the many excitations under optical stimulation, a situation arises where excitons and free carriers are present at the same time in the active layer of BHJ-based devices. Investigation of the optoelectronic processes and interactions involving these excitons and polarons are crucial since they play a major role in determining device function and performance.[228] In addition, charge trapping due to

extrinsic species such as interface states and dopants, and intrinsic species such as aggregates and excimers is an important consideration as well.[229] Hence, investigation of the interactions between polarons and excited states as well as the charge tapping at interfaces within the BHJ structure and between the BHJ structure and other device layers (i.e. materials) present in a functioning device is of great significance.[230,231] However, the coexistence of excitons, polarons, charge-transfer states as well as other chemical intermediates, in combination with the nanostructured complexity and heterogeneity of conjugated polymer bulk films hampers the development of in-depth understanding of how the co-existence and interactions between these species affect device function. Single molecule and single nanoparticle spectroscopy methods have been effective tools in removing complications caused by the study of bulk materials.[10,11,13,74,232-238] In particular, Fluorescence-Voltage/Single Molecule Spectroscopy and Fluorescence-Voltage/Single Particle Spectroscopy (F-V/SMS and F-V/SPS) have proven to be very useful tools in revealing the nature of intermediate states associated with fluorescence blinking, and the interactions between excitons and polarons. Specifically, singlet and triplet exciton quenching by hole polarons in single conjugated polymer molecules and nanoparticles,[70,239-242] and quenching of singlet excitons by triplets have been investigated.[122,243] Light-assisted hole injection from hole-transporting layers into single conjugated polymer chains has recently been reported.[244] F-V/SMS and F-V/SPS involve recording single molecule/nanoparticle

fluorescence intensity transients while applying a triangular bias modulation on a device. These devices are basically hole-only capacitor devices or functioning diodes,[70,245] where the applied bias controls hole injection and removal kinetics at the interface of a hole transporting layer (HTL) and the single molecules/nanoparticles.

Herein, the F-V/SPS technique was applied for the first time to the study of undoped and 50 wt% $PC_{60}BM$ doped P3HT NPs embedded in hole-only capacitor devices. The F-V/SPS technique was specifically applied to investigate the interaction between photogenerated excitons, photogenerated holes and electrons (free charge carriers through charge transfer from P3HT to $PC_{60}BM$), and injected holes (through applied bias) on a particle-by-particle basis for both undoped P3HT NPs and composite P3HT/$PC_{60}BM$ NPs. In addition, charge trapping at the HTL/NP interfaces as well as the NP/dielectric interfaces was investigated. The devices were built on top of optically transparent ITO-glass substrates coated with dielectric layers on which the polymer NPs were deposited by spin coating. The devices were then finished by thermal deposition of (N,N'-bis(3-methylphenyl)-N,N'-diphenylbenzidine (TPD) as a hole transporting layer that forms an electrical contact between the NPs and the gold top electrode. The device is schematically represented in Figure 2. 5. In the case of these hole-only capacitor devices, with the molecules or NPs located at the dielectric interface, the fluorescence of these nanomaterials actually reports on the charging and discharging of the NPs and the NP-dielectric interface. When the hole concentration in

the NPs and at the NP-dielectric interface is high the fluorescence signal will be strongly quenched (forward bias operation i.e. accumulation mode, or zero bias in the case of the composite NPs) while for vanishing hole concentrations the fluorescence signal will be unquenched (reverse bias operation i.e. depletion mode). As such, the fluorescence-voltage signal can be interpreted as an optical derivative of a capacitance-voltage measurement, as will also be shown in the data presented herein. The distinction between undoped P3HT and composite P3HT/$PC_{60}BM$ NPs is imperative here since the composite P3HT/$PC_{60}BM$ NPs enable the continuous photogeneration of holes and electrons even under depletion mode.

The F-V/SPS data reported in this paper show that (i) undoped P3HT NPs exhibit injected-hole-induced quenching of P3HT fluorescence due to energy transfer to holes present at the TPD/P3HT interface[70,123,241] and/or hole injection into the P3HT NPs,[70,123,241,244,246-248] (ii) quenching of P3HT emission in 50 wt% $PC_{60}BM$ doped P3HT NPs can be eliminated under negative bias (hole depletion) as observed by P3HT fluorescence recovery, indicating removal of holes on the polymer backbone before exciton quenching can occur, (iii) F-V/SPS data for all undoped P3HT NPs and 50 wt% $PC_{60}BM$ doped P3HT NPs exhibiting low modulation depth do not show hysteresis, while (iv) the majority of 50 wt% $PC_{60}BM$ doped P3HT NPs exhibiting moderate to high modulation depth do show hysteresis in the fluorescence-voltage sweeps. The variability in modulation depths for observations (i), (ii), and (iii) indicates that there

are highly complex and heterogeneous energy and hole transfer processes occurring at the TPD/NP and NP-dielectric interfaces. The lack of hysteresis indicates that hole movement during hole sweep-in and sweep-out under bias is sufficiently fast and is not hampered by e.g. deep hole trapping. These observations are similar to previously studied MEH-PPV NPs and MEH-PPV single molecules.[70,242,246] However, in the presence of $PC_{60}BM$ (i.e. composite P3HT/$PC_{60}BM$ NPs) the fluorescence-voltage modulation data for single NPs clearly shows a strong hysteresis that can be attributed to significant electron trapping at the NP-dielectric interfaces. These data show that efficient photogeneration of free charge carriers in the composite P3HT/$PC_{60}BM$ NPs under illumination can actually lead to a build-up of interfacial charge (with associated interfacial dipoles) that not only strongly affects the interfacial charge transfer process at the nanometer scale but also leads to a charge-storage behavior. Our results correspond well with the memory functions (via optical programming and electrical erasing) demonstrated in bulk P3HT/$PC_{60}BM$ and P3HT/CdSe based OFET devices, which are caused by an electron trapping-detrapping mechanism.[249,250] The interfacial charge trapping also suggests possible applications in optical sensing and charge coupled devices (CCD).[251,252] Thus, the charge-storage effect reported here for the first time for the composite polymer NPs presents an opportunity for future exploration of conjugated polymer/fullerene NP applications in nanoscale memory and imaging devices.

6.2 Results and Discussion

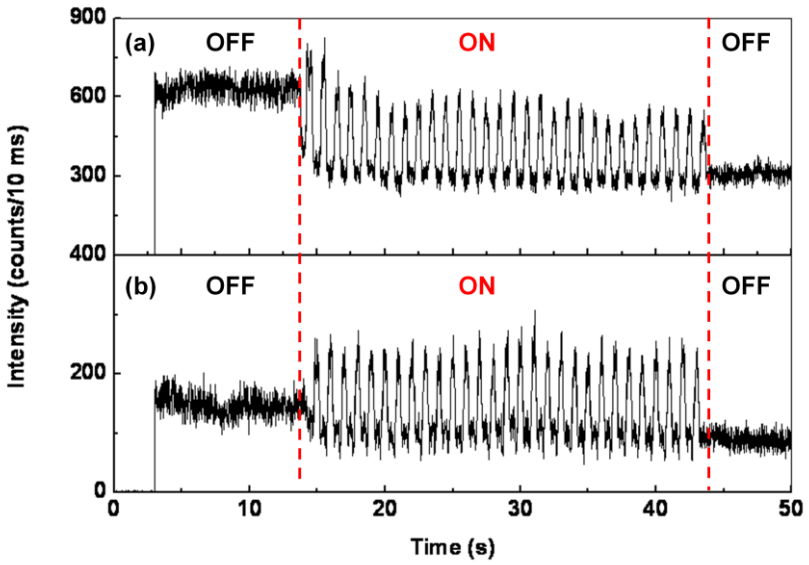

Figure 6. 1 Bias modulated fluorescence transients of an undoped P3HT NP and a 50 wt% $PC_{60}BM$ doped P3HT NP that exhibiting optoelectronic instability under triangular bias modulations from + 10 V to – 10 V at a sweep rate of 40 V/s. The bias on and off period are indicated in the figure.

The NPs studied in the present work were fabricated in aqueous environment. As is well known, moisture and oxygen can have significant adverse effects on the photostability of conjugated polymers.[253] Figure 6. 1 displays bias-modulated fluorescence emission transients of an undoped P3HT NP and a 50 wt% $PC_{60}BM$ doped P3HT NP that exhibit optoelectronic instability. As can be seen, comparing the fluorescence intensity before and after bias application, one can find that the intensity after bias modulation drops to ~ 1/3-1/2 of the initial intensity before bias modulation.

Close inspection reveals that the intensity level after bias modulation is the same as the intensity under the extreme positive bias (+ 10 V in the present case) during the modulation period. This data implies that these NPs were partially oxidized once the positive bias was applied, which is due to a (photo-)electrochemical reaction of the polymer in the presence of residual H_2O and O_2 molecules (either from NPs or PVA matrix).[253] To eliminate the perturbation of this oxidation and study NPs in the hole-injection device under pristine conditions, we made every effort to remove residual moisture and oxygen from the NPs and the devices. After spin coating of the NPs on top of the dielectric layer, the samples were evacuated in a vacuum chamber overnight and then exposed to a dry N_2 atmosphere in a glove box with O_2 and H_2O level both less than 0.1 ppm for several days. Experiments showed that this process removed damage to the NPs and device caused by (photo-)electrochemistry induced by the presence of residual H_2O and O_2.

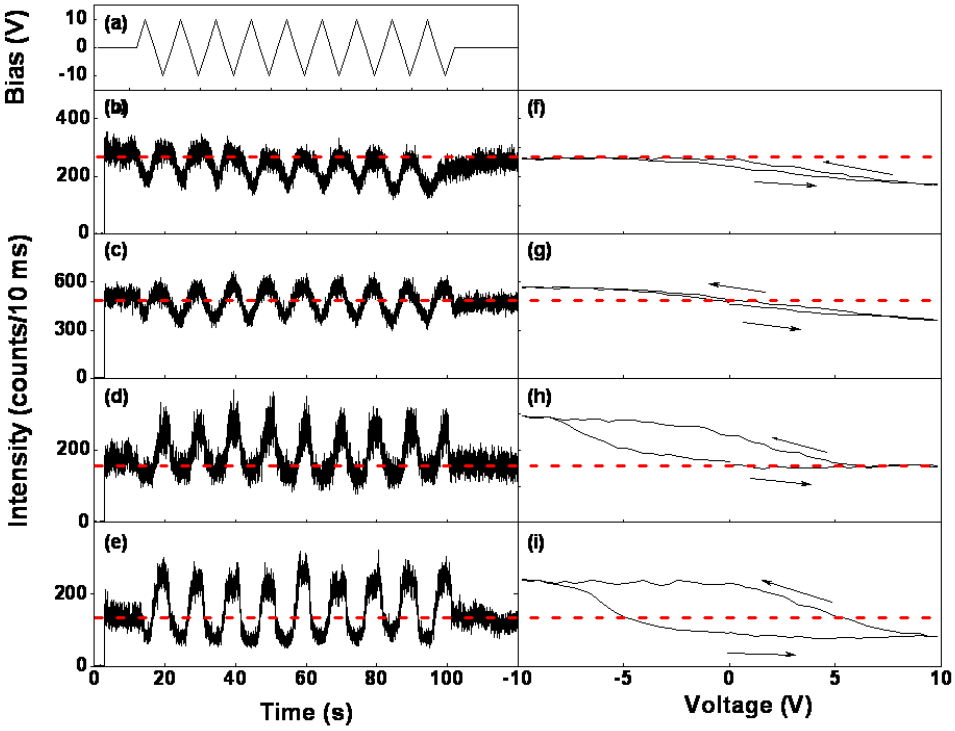

Figure 6. 2 Typical fluorescence transient modulations (dwell time: 10 ms) of the representative majority of the (b) undoped and (d) 50 wt% $PC_{60}BM$ doped P3HT nanoparticles while repeatedly applying a triangle bias sequence (a) at a sweep rate of 4.0 V/s to the device in 12-102 s. Panels (c) and (e) present the modulation of a minority of undoped and 50 wt% $PC_{60}BM$ doped nanoparticles that show both fluorescence quenching at positive bias and recovery at negative bias, respectively. Panels (f-i) depict corresponding time averaged fluorescence modulation plots as a function of applied bias voltage for the transients shown in panels (b-e). The arrows in panels (f-i) signify the direction of the bias scan. The corresponding fluorescence modulation characteristics at a higher sweep rate of 40 V/s collected for the same nanoparticles are given in Figure 6. 3. Note that the background fluorescence intensity is ~ 5 counts/10 ms under the excitation power of 0.72 W/cm^2 used for the undoped P3HT nanoparticles and ~ 15 counts/10 ms with the excitation power of 7.2 W/cm^2 for the composite nanoparticles.

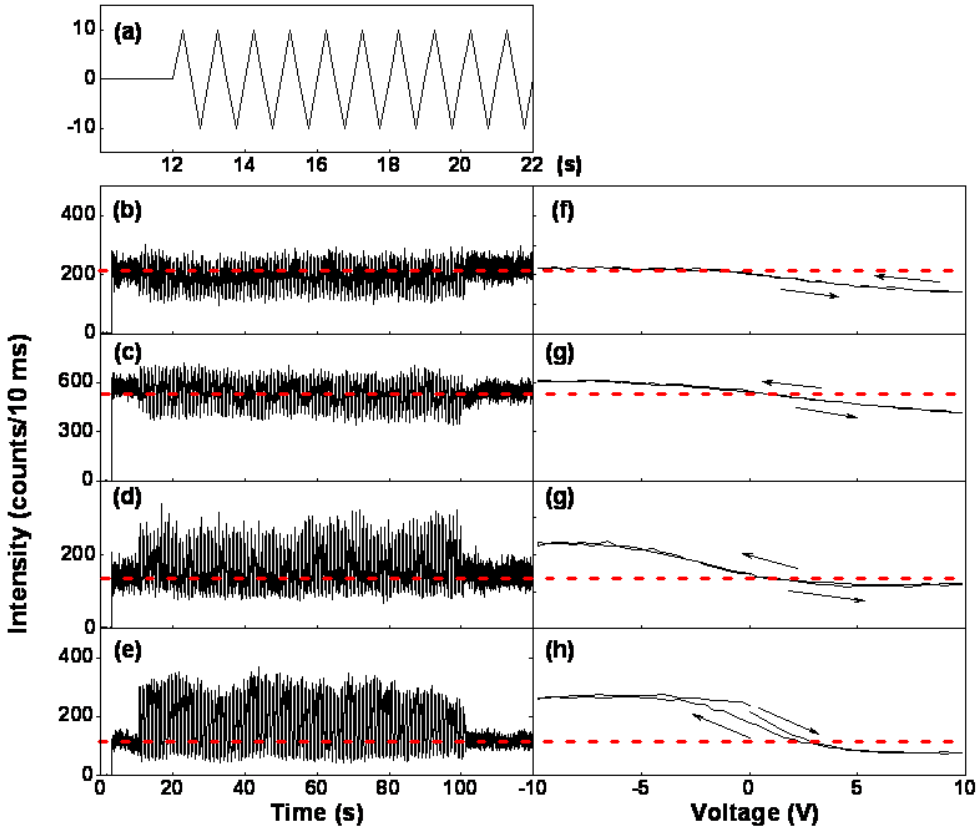

Figure 6. 3 Typical fluorescence transients (dwell time: 10 ms) and fluorescence voltage curves for (b) undoped and (c) 50 wt% $PC_{60}BM$ doped P3HT nanoparticles while repeatedly applying a triangle bias sequence from 12 to 102 s at a sweep rate of 40 V/s to the device (a). Panels (d) and (e) present the modulation of a minority of undoped and 50 wt% $PC_{60}BM$ doped nanoparticles that show both fluorescence quenching at positive bias and recovery at negative bias, respectively. Panels (f-i) depict the corresponding time-averaged fluorescence modulation plots as a function of applied bias voltage for the fluorescence transients shown in panels (b-e). The arrows in panels (f-i) indicate the direction of the bias scan (starting from 0 V). The corresponding fluorescence modulation characteristics at slow sweep rate of 4.0 V/s collected for the identical nanoparticles are shown in Figure 6. 2.

Figure 6. 2 displays the bias-induced fluorescence modulation behavior of both undoped P3HT NPs and 50 wt% $PC_{60}BM$ doped P3HT NPs acquired by applying a periodic triangular voltage sequence (Figure 6. 2(a)) on the hole-injection capacitor

device in which these NPs are embedded. During the experiments two types of modulation behavior were exhibited by each type of NPs. Undoped P3HT NPs show either only fluorescence quenching at positive bias (Figure 6. 2 (b)) or fluorescence quenching at positive bias together with fluorescence recovery at negative bias within a voltage cycle (Figure 6. 2(c)). For 50 wt% $PC_{60}BM$ doped P3HT NPs the majority only exhibits fluorescence recovery at negative bias, with a minority of NPs showing fluorescence recovery at negative bias together with fluorescence quenching at positive bias within a voltage cycle, as demonstrated in Figure 6. 2(d) and (e), respectively. These observations are discussed below. Averaging these data over a number of bias cycles and re-plotting as a function of applied bias yields the fluorescence modulation vs. bias curves displayed in Figure 6. 2(f- i). Minor or no hysteresis is observed for the undoped NPs (Figure 6. 2(f-g)) at the bias scan rates used in this study (4.0 V/s and 40 V/s) and implies rapid hole injection and removal rates. These data indicate fast reaction of mobile holes in the device to the electrical field and only shallow hole trapping (if any) near the TPD/P3HT NP interface.[246,248] In comparison, the data in Figure 6. 2(h-i) for the 50 wt% $PC_{60}BM$ doped NPs show the occurrence of significant hysteresis, as discussed further below.

The majority of the undoped NPs show the modulation behavior depicted in Figure 6. 2(b) and (f). The fluorescence intensity reduces gradually and almost linearly upon applying positive bias to the device, while no detectable intensity enhancement is

observed at negative bias. The fluorescence quenching at positive bias, ranging from 5% to 40%, is attributed to a combination of *charge transfer and energy transfer mechanisms* between holes injected in the device at positive bias and singlet excitons that are optically excited in the P3HT NPs.[70,242] The inefficient quenching of fluorescence for the undoped NPs can be attributed to the following aspects: (i) hole transfer from TPD to P3HT is isoergic in energetics rather than exoergic;[246,248] and (ii) limited quenching volume of 390 nm^3 for single excitons by holes in conjugated polymers[239,240] considering the much larger volume of NPs (diameter of ~ 30 nm in the present case). At negative bias, holes are removed from the device (depletion). The majority undoped NPs do not show obvious fluorescence recovery under these conditions, indicating negligible presence of free charge carriers in these NPs. While it is well-known that if photoinduced free charge carriers ($P3HT^+$ and $P3HT^-$) can be formed in undoped P3HT materials, a fluorescence intensity increase would be expected in the reported experiments due to hole (i.e. quencher) removal at negative bias. Only ~16% of the undoped NPs exhibit both fluorescence quenching and recovery modulations, as illustrated in Figure 6. 2(c) and (g). This observation indicates the presence of an oxidized state of P3HT (i.e. $P3HT^+$/anion) in these NPs either due to intrinsic free charge carrier formation or photooxidation. Yields of free charge carrier generation for P3HT have been reported to be in the range of 5% to 30% under photoexcitation in the absence of electron acceptors,[199,254,255] which can explain our

observations of recovery at negative bias for a fraction of undoped NPs. The occurrence of partially oxidized NPs is expected to be minimal given that care has been taken in eliminating oxygen and water from the device to ensure NP photostability.

Considering the 50 wt% $PC_{60}BM$ doped P3HT NPs, the majority does not exhibit fluorescence quenching at positive bias as shown in Figure 6. 2(d) and (h). With the presence of $PC_{60}BM$, the fluorescence of P3HT in the composite NPs is strongly quenched due to an ultrafast electron transfer process from P3HT to $PC_{60}BM$, which is much faster than the energy transfer process between singlet states and holes.[228] This ultrafast charge transfer process combined with resultant short fluorescence lifetime[199] probably hampers further exciton quenching by injected holes. In addition, the injected hole concentration near the TPD/NP interface might be low due to electrostatic repulsion from photo-generated holes and low bias applied to the device. A fraction (~ 25%) of the doped NPs demonstrate fluorescence quenching of ~ 10-50% at positive bias in addition to recovery at negative bias (Figure 6. 2(e) and (i)). The difference in fluorescence modulation at positive bias observed for the 50 wt% $PC_{60}BM$ doped NPs could be ascribed to heterogeneities of the distribution of components in the NPs e.g. phase separation, slight variations in composition between different NPs, or different local environment of the NPs in the device that may lead to changes in the energetics of interfacial charge and/or energy transfer.

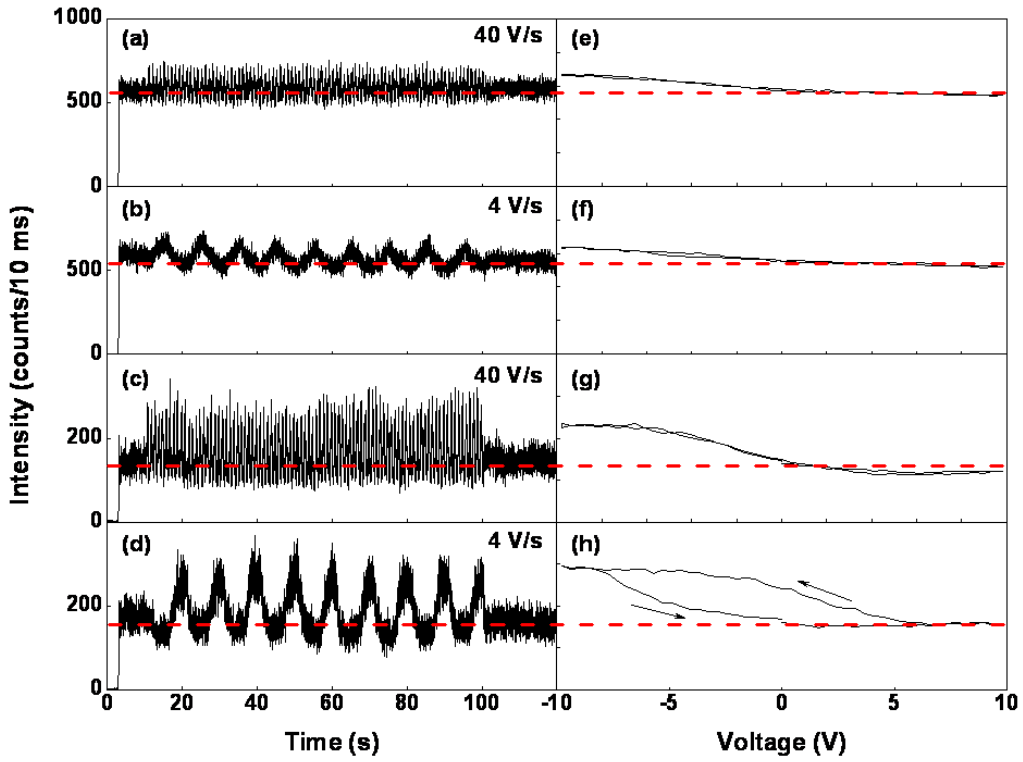

Figure 6. 4 50 wt% $PC_{60}BM$ doped nanoparticle fluorescence transients obtained while modulating a triangle bias sequence across the device. Transients in (a) and (b) displaying low fluorescence recovery under negative bias were acquired from the same nanoparticle under different sweep rates indicated in the figures. Transients in (c) and (d) showing strong fluorescence recovery were also taken from the same nanoparticle. The right column exhibits corresponding time averaged fluorescence-voltage curves (e-h) derived from the scans in the left figures (a-d). The arrows in (e-h) signify the direction of the bias scan.

When negative bias is applied to the device, nearly all of the 50 wt% $PC_{60}BM$ doped P3HT NPs show obvious fluorescence recovery ranging from 10% up to 100% (Figure 6. 4(a-d)). This observation provides clear evidence of the presence of free charge carriers ($P3HT^+$ and $PC_{60}BM^-$) due to photoinduced charge transfer from P3HT to $PC_{60}BM$ in the composite NPs. In current case, P3HT is oxidized to its cation ($P3HT^+$, quenched state) via charge transfer to $PC_{60}BM$ under photoexcitation. The

$P3HT^+$cation is reduced to its emissive state (under excitation) by hole removal at negative bias. The observation of fluorescence recovery for the oxidized P3HT when applying negative bias is to some extent in analogy to that found for photooxidized MEH-PPV single molecules, for which the photochemical species are suspected to be MEH-PPV^+/O_2^- (OH^-).[242] However, specific to the 50 wt% $PC_{60}BM$ doped P3HT NPs, additional trends in the bias-induced fluorescence modulation are observed at negative bias. First, in the negative bias region, the photooxidized MEH-PPV single molecule fluorescence recovery shows a pronounced plateau, caused by a rapid and reversible single electron transfer process in a two-level system (oxidized and reduced species).[70,242] In comparison, the composite NP data display a gradual modulation behavior as a function of applied bias, especially for NPs exhibiting small fractions of fluorescence recovery with respect to the baseline (zero bias) fluorescence, see Figure 6. 4(a-b, e-f). This gradual modulation behavior as opposed to an ON/OFF switching between two discrete states as found for single molecules or NPs[70,242] can be explained by the presence of multiple P3HT molecules in the NPs that exhibit charge transfer to $PC_{60}BM$ in the NPs or energy/charge transfer across the TPD/NP interface at different times and with different rates. Second, as shown in Figure 6. 4(c-d, g-h), for the doped NPs *stronger hysteresis at slower sweep rates* as opposed to faster sweep rates (as observed for MEH-PPV single molecules and NPs[70,242,246]) is observed, and this hysteresis effect is found mostly for NPs showing strong fluorescence intensity

recovery at negative bias. Thus, for the 50 wt% $PC_{60}BM$ doped P3HT NPs the observed hysteresis is strongly related to the modulation depth. Composite NPs showing weak recoveries as portrayed in Figure 6. 4(a-b) do not show a significant hysteresis for the sweep rates used (i.e. 40 V/s and 4.0 V/s in Figure 6. 4(e) and (f), respectively), implying a rapid hole removal and retrieval process probably due to only shallow charge traps at the TPD/NP interface or an absence of charge trapping at the NP/dielectric interface *due to a low population of free charge carriers being generated in these specific NPs*.[246,248,256] The lower population of free charge carriers in these NPs may be due to compartmentalization (phase separation) of P3HT and $PC_{60}BM$ in the NPs, or low presence of $PC_{60}BM$ in these NPs. In addition, there may be poor contact of the NPs with the TPD/Au electrode. However, the 50 wt% doped NPs showing strong modulation behavior i.e. large fraction of fluorescence recovery with respect to the baseline (zero bias) fluorescence when studied under a (low) sweep rate of 4.0 V/s exhibit a large hysteresis, as shown in Figure 6. 4(f) and (h). Specially, as shown in Figure 6. 4(c-d), a large anticlockwise hysteresis was observed at a slow sweep rate (4.0 V/s). This observation is quite distinct from that found for previously investigated photooxidized MEH-PPV single molecules or NPs, in which higher sweep rates typically yield larger clockwise hysteresis due to slow interfacial kinetics, i.e. the oxidation/reduction process is cycled too rapidly to be able to reach equilibrium.[70,246] Although these two systems seem analogous in terms of photochemically formed

species, i.e., $P3HT^+/PC_{60}BM^-$ for the composite NPs under photoexcitation in this work, and MEH-PPV^+/anions in photooxidized MEH-PPV single molecules,[70,242] significant differences should be noted. In the composite NPs, emissive excitons coexist with a large amount of free charges including $P3HT^+$, $PC_{60}BM^-$ originating from charge transfer from P3HT to $PC_{60}BM$, and $P3HT^-$ originating from direct P3HT exciton dissociation,[199,257] all of which impose significant effects on interfacial charge transfer processes and trapping. The specifics of these processes will now be further discussed by means of the data and schematics presented in Figure 6. 5.

Starting from 0 V and sweeping to + 10 V holes injected into the TPD layer are expected to be accumulated near the TPD/dielectric and TPD/NP interfaces at sufficiently high positive bias voltage. Hole accumulation and trapping most likely occurs at these interfaces, albeit that the traps are shallow (Figure 6. 5(b)).[246,248,256] Several studies have shown that fullerene anions can act as effective deep hole traps.[258-260] It is therefore likely that a fraction of the population of photogenerated holes and/or electronically injected holes remain trapped by proximal $PC_{60}BM$ anions. When cycling back from + 10 V to 0 V, photogenerated holes in the composite NPs and holes in TPD are gradually removed with decreasing positive bias, bringing the device towards hole depletion. Holes in shallow traps are quickly removed as well (Figure 6. 5(c)). As a result the population of P3HT cations is gradually reduced to neutral P3HT

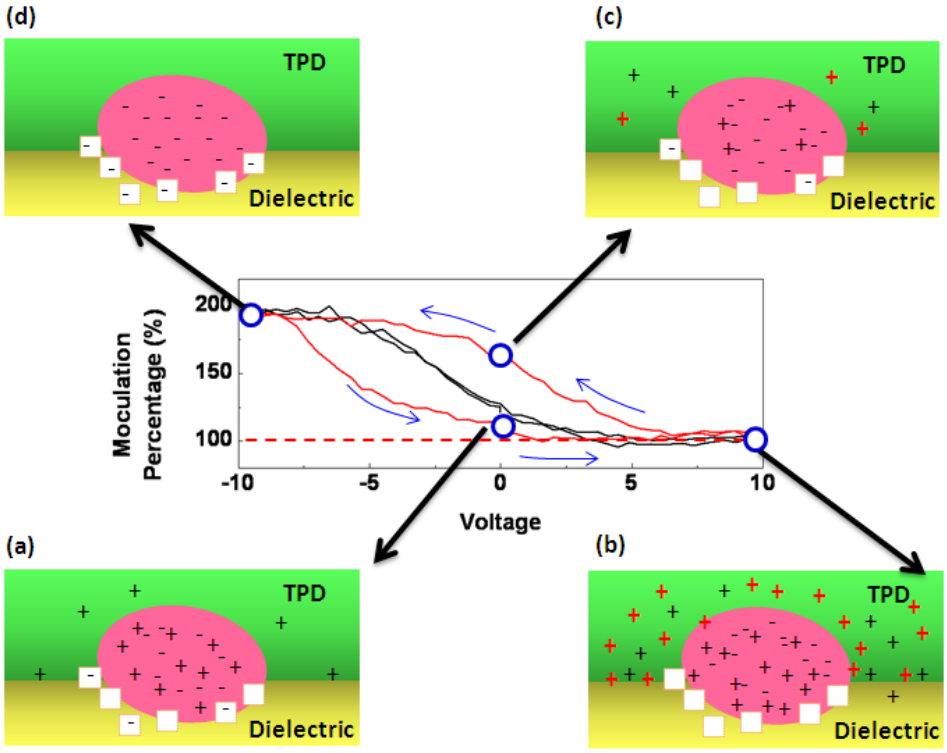

Figure 6. 5 The data plot in the middle panel displays time averaged fluorescence intensity modulation percentage vs. voltage curves collected for the same 50 wt% $PC_{60}BM$ doped P3HT nanoparticle at sweep rates of 4.0 V/s (black) and 40 V/s (red). The red dashed line indicates the base line fluorescence modulation percentage (at zero bias). The blue arrows show the direction of voltage scan (starting from 0 V). The four circles on the black curve indicate the conditions that are being represented by the cartoons. The pink ellipsoid represents a nanoparticle and the white squares indicate electron trap sites. The red and black "+" symbols represent bias injected holes and photogenerated holes, respectively, while the black "-" symbols represent photogenerated electrons.

molecules, which can be observed by a fluorescence increase with respect to the baseline fluorescence as the bias evolves to negative voltages. Continuing to reverse bias from 0 to - 10 V, more and more photogenerated holes are removed from the NP until the fluorescence recovery reaches a plateau when the applied bias exceeds - 5 V. At that point the device appears as being fully depleted from photogenerated and

previously injected holes. During this process there is still photogeneration of holes and electrons, but holes are quickly removed from the device. Thus, an excess of electrons is built up near the NPs and NP/dielectric interfaces (Figure 6. 5(d)). Previous literature reports have extensively documented that electrons can be deeply trapped at organic-dielectric interfaces or even in the bulk of the dielectric, and that $PC_{60}BM$ is a deep electron trap as well.[250,261] In these cases anticlockwise hysteresis in capacitance-voltage data was typically observed.[250,262-264] In addition, when comparing the forward sweep curve obtained at 4.0 V/s, particularly from - 10 to 0 V (forward sweep) with the corresponding fast scan curves obtained at 40 V/s, a negative shift is evident for the slow scan curve in the data reported herein. Similar observations have been reported previously for capacitance-voltage measurements on polymer-dielectric two-terminal and three-terminal devices.[251,265] Several reports have also been made where capacitance-voltage measurements were completed on P3HT and P3HT/$PC_{60}BM$ two-terminal and three-terminal devices under illumination.[249-251] Strong hysteresis was observed in all of the reports, and was attributed to a build-up of free carriers due to photoinduced charge transfer from P3HT to $PC_{60}BM$ or spontaneous exciton dissociation in the absence of $PC_{60}BM$ that results in trapping of electrons at the organic-dielectric interface. This assignment was supported particularly well in the report by Lancaster et al., where a control experiment was also completed while optically exciting the device outside of the P3HT absorption band. In that case no

accumulation and trapping of electrons was observed due to the low exciton generation rate near the organic-dielectric interface.[251] Based on these literature reports, it is thus reasonable to assign the observed anticlockwise hysteresis at lower bias sweep rates for the single composite P3HT/$PC_{60}BM$ NPs to the trapping of photogenerated free electrons at the P3HT/dielectric interface and/or on $PC_{60}BM$. The trapped electron density can be roughly estimated, as discussed in reference [251] and [266], from the negative voltage shift of the forward sweep curve (i.e. from -10 to 10 V) when comparing the slow sweep and fast sweep data, and the relation $Q=C_i\Delta V/A$ where C_i is the insulator capacitance, ΔV is the shift in the voltage which is about 2.5 V (Figure 6. 5), and A the device area of 0.066 cm^2. C_i is calculated to be 0.5 nF via $C_i=\varepsilon_r\varepsilon_0 A/d$, where $\varepsilon_r = 3$, and the dielectric layer thickness $d = 350$ nm. From this approximation the density of trapped electrons is found to be $1.2\times10^{11}/cm^2$.

Detrapping and removal of electrons is expected to occur during the forward sweep (from – 10 to +10 V). During the forward sweep holes start to accumulate in the polymer NPs (as evidenced by the decreasing fluorescence signal) and can recombine with trapped electrons (Figure 6. 5(a)). In addition, the electric field in the device during the forward sweep will help to detrap electrons. However, electrons are not likely to be injected back into the NPs or TPD layers, so the removal of electrons by recombination with holes is limited by the rate at which photogenerated and injected holes reach the organic-dielectric interface.[250,265] As shown in the middle panel of

Figure 6. 5, the reverse sweep (+10 - -10V) under slow scan conditions is shifted to positive bias compared to the faster scan experiment, probably because of hole trapping by $PC_{60}BM$ anions in the composite nanoparticles given that this effect was not observed for undoped nanoparticles.[258-260]

In summary, the hysteretic data observed for single composite P3HT/$PC_{60}BM$ NPs under illumination in the hole-only capacitor devices discussed above clearly indicate electrically bistable behavior due to electron trapping at the organic-dielectric interfaces and hole trapping by fullerene anions in composite P3HT//$PC_{60}BM$ NPs under photoexcitation. These experimental results are promising for future applications of donor-acceptor composite NPs in *photocontrolled memory devices*, *metal-insulator-semiconductor (MOS) imaging devices a*nd *photoresponsive OFETs*, with the potential for nanoscale or single NP device elements.

6.3 Conclusion

Memory functions via optical programming and electrical erasing have been reported for bulk P3HT/$PC_{60}BM$ and P3HT/CdSe based devices and attributed to electron trapping-detrapping near the organic-dielectric interface and on the electron acceptors present in these blended materials.[249,250] In the present paper, Fluorescence-Voltage/Single Particle Spectroscopy (F-V/SPS) was employed to study exciton-hole polaron interactions and interfacial charge transfer processes for *individual* undoped P3HT NPs and composite P3HT/$PC_{60}BM$ NPs in functioning

hole-injection devices. F-V/SPS data collected for individual nanoparticles reveal an apparent hysteresis in the data for composite P3HT/PC_{60}BM NPs that is attributed to the deep trapping of photogenerated free electrons at the organic-dielectric interface and hole trapping by fullerene anions in composite P3HT/PC_{60}BM NPs under photoexcitation. To our knowledge, this is the first report on the investigation of charge trapping based on single nanoparticles, and opens the door for novel approaches to understanding charge-storage mechanism on the nanometer scale and future applications of composite conjugated polymer nanoparticles in nanoscale memory and photoresponsive devices such as light activated switches and light induced amplifiers.

CHAPTER 7. NEAR-INFRARED REGION ABSORPTION SENSITIZATION OF P3HT/PC_{60}BM PHOTOVOLTAICS BY LOW BAND GAP POLYMER AND SMALL MOLECULE DYE

7.1 Introduction

Since the first report of P3HT/PC_{60}BM solar cell with a PCE more than 4%,[34] great research efforts have been devoted to the optimization of the morphology, charge transport, device designs as well as the understanding of photophysics mechanisms.[20,21,25,27,267] Despite of all these input, the reported PCE of this kind of cells still remains in the range of 1-5% depending on material sources and processing methods.[17,18] It has been estimated that P3HT, with a band gap of 1.9 eV, absorbs only about 27% of the solar photons, which strongly limits the further improvement of device PCE.[18]

To harvest more solar photons in a broad wavelength range, Kim et al fabricated OPVs with a tandem cell architecture. In this device geometry two solution processed polymer cells are stacked in series in a multilayer device.[39] This tandem architecture consisting of a P3HT/PC_{70}BM cell and a PCPDTBT/PC_{60}BM cell yields an efficiency of 6.5%, which is much higher than the individual cell performance of 3.0% and 4.7% for the PCPDTBT and P3HT device, respectively. Although tandem solar cells appear promising in improving the device performance, the wide applicability of this complicated multilayer structure has been challenged by two main factors. First, a perfect balance between the front and back cells in photocurrent is needed to prevent

the formation of an inverse heterojunction. The second issue involves the attenuation of light that can be absorbed by the back cell due to the presence of the front cell .[40] The development of novel low band gap (LBG) polymers represents another promising approach in expanding solar photons capture range.[17,268,269] However, the main challenge for OPV applications is to find the right LBG polymers that will allow for an active layer morphology conducive to efficient devices while keeping good charge transporting properties. The initial trials over the past several years with LBG polymers have result in lower than expected device performance. For instance, LBG polymer poly({2,6-(4,4-bis(2-ethylhexyl)-4H-cylopenta[2,1-b;3,4-b']dithiophene}-alt-{4,7-(2,1,3-benzothiadiazole)}) has a band gap of 1.45 eV and a broad absorption range up to 900 nm. However, OPV devices based on this polymer (in a 1:1 blend with $PC_{61}BM$) show an efficiency of 2.7% only with an open-circuit voltage (V_{oc}) of 0.65 eV and a peak EQE of about 30%.[44] This low PCE has been attributed to the low charge mobility in the active layer. Fortunately, since 2009, there has been a rapid development of efficient LBG polymers based photovoltaic devices starting with the report of poly[[9-(1-octylnonyl)-9H-carbazole-2,7-diyl]-2,5-thiophenediyl-2,1,3-benzothiadiazole-4,7-diyl-2,5-thiophenediyl (PCDTBT) with a PCE of 6.1%.[41] Following that, several LBG polymers have been synthesized that have result in efficient OPVs, among which poly[4,8-bis(2-ethylhexyloxy)-benzo[1,2-b:4,5-b']dithiophene-2,6-diyl-alt-(4-octanoyl-5-fluoro-thieno[3,4-b]thiophene-2-carboxylate)-2,6-diyl] (PBDTTT-CF)

produces an efficiency of 6.77% and PTB-7 exhibits an efficiency of 7.4%.[19,59] Although these polymers are very attractive, however, the synthetic methods of these polymers are very complicated relative to that of traditional P3HT, which makes them not easily commercially available and extremely expensive at present.

Compared to the previous two methods in extending the organic solar cell absorption range, a direct doping of absorbers into the polymer/fullerene layer with an absorbing range complementary to the absorption range of the polymer/fullerene blend represents a much simpler and versatile alternative approach. To realize effective doping, the dopant must meet the following basic criteria: (1) the energy levels of the dopant should lie intermediately to those of the polymer and fullerene; (2) the absorption coefficient of the dopant in the complementary absorbing range should be high; and (3) the dopant can either act as an electron donor and hole transporter or operate as an electron acceptor and transporter.[91] Recently, researchers have shown successful incorporation of small far-red-absorbing dyes in the prototypical P3HT/$PC_{60}BM$ cells. Peet et al demonstrated a photocurrent increase in P3HT/$PC_{70}BM$ cell when doping with a soluble oligothiophene having a diketopyrrolopyrrole core for near-infrared (NIR) absorption.[47] The introduction of phthalocyanine derivatives in OPVs for increasing the light-harvesting efficiency has been demonstrated by Honda and coworkers.[92] These investigators found that the introduction of silicon phthalocyanine (SiPc) can not only directly yield photocurrent output at the absorption wavelengths of SiPc but indirectly

enhance charge separation from P3HT excitons through energy transfer from P3HT to SiPc molecules located at the P3HT/PC_{60}BM interface. It is estimated that this energy transfer rate is more than 100 times faster than the energy migration rate in P3HT, therefore promoting the P3HT exciton diffusion and subsequent dissociation.

Compared to small molecule absorber doping, LBG polymers as dopants are more structurally favorable due to the miscibility of conjugated polymers. Despite of great efforts and trials in producing single-layer cells with LBG polymer, less attention has been put into developing LBG polymer doped cells. The NIR sensitization of P3HT/PC_{60}BM cells by a LBG polymer PCPDTBT only recently has been studied by Koppe et al.[48]

In the studies presented in this chapter, P3HT/PC_{60}BM cells incorporated with near-IR absorbing low band gap polymer PTB-7 and a small molecule dye were fabricated in order to enhance the capture of near-infrared photons in a typical P3HT/PC_{60}BM solar cell. For the PTB-7 doped system, a solvent additive 1,8-diiodooctane (DIO) was also applied to optimize nanoscale phase separation while simplifying the device fabrication process. For solar cells fabricated with DIO additive, the incorporation of 20 wt% PTB-7 into P3HT/PC_{60}BM cell leads to ~ 33% increase in the short-circuit current and a ~32% increase final device performance compared to the reference P3HT/PC_{60}BM cell processed with DIO, while a ~ 255% increase in the short-circuit current and a ~ 369% increase in final device performance is found compared to the reference

P3HT/$PC_{60}BM$ cell processed without DIO. The incorporation of the small molecule dye, in contrast, deteriorates the device performance with an appearance of S-shaped J-V curves caused by bad film morphology. The morphological, opto-electronic and photovoltaic properties of the active layers and devices discussed above were systematically studied for these two systems.

7.2 Results and Discussion

7.2.1 Sensitization by LBG polymer PTB-7

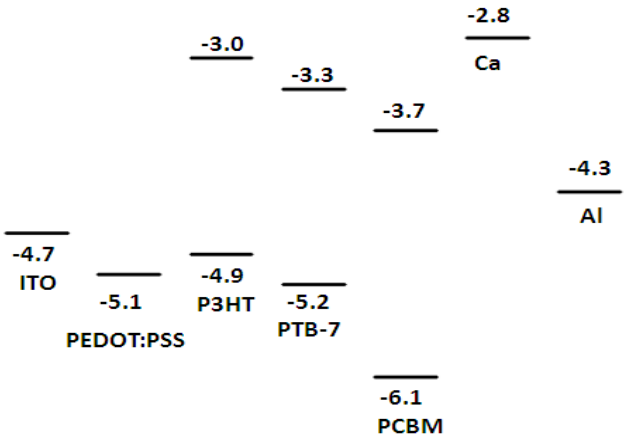

Figure 7. 1 Energy-level diagram showing the HOMO and LUMO energies of semiconductor components and the work function of electrode materials in the PTB-7 doped P3HT/$PC_{60}BM$ devices.

PTB-7 has a band gap of about 1.84 eV (Figure 7. 1) leading to an absorption extending up to 800 nm.[19] The broad absorption coverage from 600 nm to 800 nm of the PTB-7 complements well with the P3HT absorption in the visible range of the solar spectrum, given that P3HT mainly absorbs from 500 nm to 600 nm. Another critical criterion in selecting the NIR sensitizing dopant involves the energy level

consideration. To avoid charge trapping, the energy levels of the dopant should lie in between those of the P3HT and $PC_{60}BM$.[47] Figure 7. 1 illustrates an energy diagram for the materials in this ternary solar cell. As can be seen, the LUMO and HOMO levels of PTB-7 are both located between those of P3HT and $PC_{60}BM$, which is favorable for the photoinduced electron transfer from the polymer to $PC_{60}BM$. In addition, energy transfer from P3HT to PTB-7 is also possible due to a large overlap between the absorption spectrum of PTB-7 and the emission spectrum of P3HT. Meanwhile, the holes generated in PTB-7 can also transfer to P3HT matrix. Furthermore, previous investigation indicates a higher hole mobility in PTB-7 than P3HT,[19] which is also beneficial for the transport of holes photogenerated in PTB-7.

In recent years, a mixed-solvents approach, especially by using solvent additives, has been demonstrated to be very effective in controlling the film morphology and improving the device performance in several polymer solar cell systems, including prototypical P3HT and several LBG polymers.[89,134,270,271] Generally, processing additives should fulfill two criteria 1) selective solubility of the fullerene component and 2) higher boiling point than the host solvent. When the film is processed with the mixed solvent, three phase can be formed during the film drying process, i.e. a polymer phase, a polymer-fullerene phase and a fullerene-additive phase.[89] Due to the higher boiling point of the additive relative to that of the host solvent, the fullerene tends to remain dissolved longer in the additive during drying process compared with

semiconducting polymer, thereby facilitating the control of film morphology and fine phase separation. Furthermore, this processing additive approach enables an easily controllable and facile device preparation with no need for post-annealing, making it very attractive in practical applications. In present work, we selected 1,8-diiodooctane (DIO) as an additive due to its excellent performance in previous studies.[89]

Absorption and photoluminescence (PL) spectroscopy of active layers

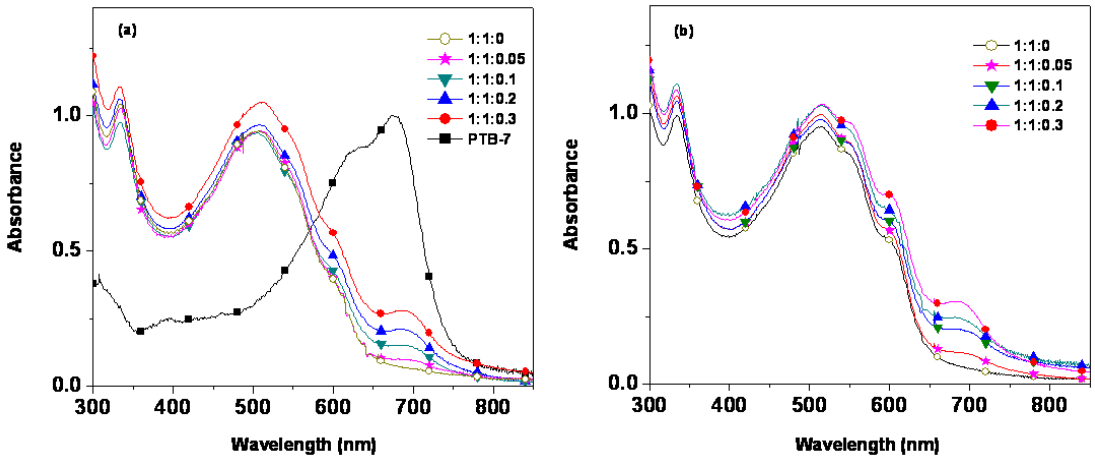

Figure 7. 2 Absorption spectra of P3HT/$PC_{60}BM$ films with different PTB-7 doping levels spin coated from DCB solutions (a) and from mixed solutions of DCB and 2.5% (volume) DIO additive (b). The absorption spectra of a pure PTB-7 film spin cast from DCB solution is also included in (a). For each absorption curve in (a) and (b), the weight ratios of P3HT:$PC_{60}BM$:PTB-7 are labeled in panel (a) and (b).

Figure 7. 2(a) displays the absorption spectra for P3HT/$PC_{60}BM$ films with different PTB-7 doping levels as well as a pure PTB-7 film spin cast from DCB solutions. For pure PTB-7 film, a broad absorption mainly ranging from 500 nm to 800 nm is found, which is complementary to the absorption of typical P3HT cells. With increasing

PTB-7 doping levels in P3HT/$PC_{60}BM$ films, from 0 wt% (weight ratio: P3HT:$PC_{60}BM$:PTB-7 = 1:1:1:0) to 30 wt% (weight ratio = 1:1:1:0.3), the ternary blend exhibits an increasing absorbance in the 650 to 800 nm range due to the contribution from PTB-7. Because of the broad absorption range of PTB-7 (300 nm to 800 nm), the addition of PTB-7 in P3HT/$PC_{60}BM$ also induces an absorbance increase in the visible region below 650 nm especially for high doping levels (20 wt%, 30 wt%) as can be seen in Figure 7. 2. The absorption spectrum of these ternary blend films is a simple superposition of the spectra of the individual components, indicative of an absence of interactions in the ground state between the components. In addition, the incorporation of PTB-7 does not result in a shift of the absorption maximum (~ 510 nm) of P3HT or disappearance of absorption shoulders at ~ 550 nm and 600 nm, suggesting that the packing of P3HT is not affected. The absorption spectra of films processed with the mixed-solvent of DCB and DIO are presented in Figure 7. 2(b). Compared with the films without DIO, the additive processed films all exhibit pronounced absorption shoulders at ~ 550 nm and 600 nm, which is attributed to an increased interchain interaction of P3HT resulting from ordered pi-stacking between polymer chains.[188] The absorption profile of PTB-7 remains similar in the films without and with DIO additive.

To obtain an understanding about possible electron or energy transfer process between P3HT and PTB-7, photoluminescence spectra were collected for films of pure P3HT,

P3HT doped with 20 wt% PTB-7 as well as pure PTB-7 films, respectively. As depicted in Figure 7. 3, The PL emission of P3HT is quenched by about 89% upon doping with 20 wt% PTB-7. In addition, compared with the pure P3HT film PL spectra, there is a significant emission intensity increase at about 755 nm for the binary blend film. To clarify this increase, a curve representing the mathematical addition of 89% quenched pure P3HT spectrum and pure PTB-7 spectra is plotted in Figure 7. 3. Note that the pure PTB-7 film has an absorption comparable to PTB-7 in the blended films. When comparing the resulting spectrum to the spectrum of the blended film of P3HT:PTB-7, it can be observed that emission the intensity above 725 nm for the blended film is about two times higher than that for the spectrum constructed by adding the 89% quenched pure P3HT and pure PTB-7 spectra. This increase is presumably due to an energy transfer process between P3HT and PTB-7. However, this increase is below that would be expected if the PL quenching of P3HT is only due to energy transfer since the PL quantum yield of thienothiophene is similar with that of P3HT.[272] Therefore, the energy transfer is not the only mechanism for the PL quenching of P3HT, but instead is suggested to be caused by a competing photoinduced electron transfer between the polymers as well.[48]

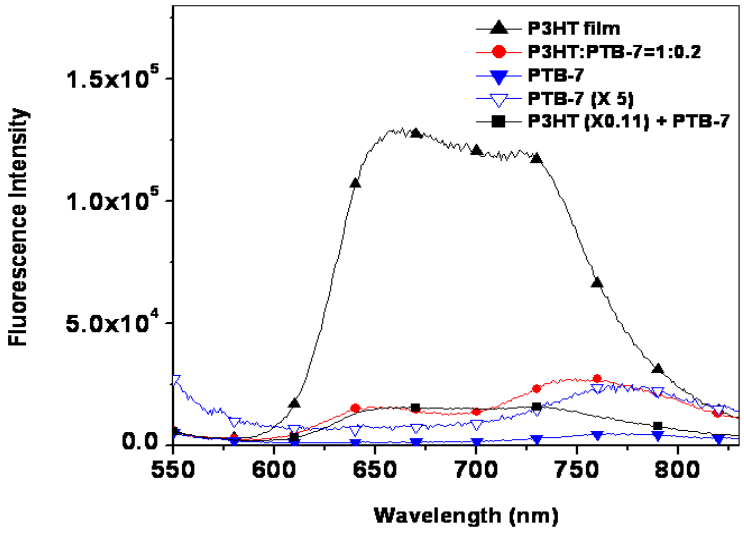

Figure 7. 3 Film photoluminescence spectra of pure P3HT, binary blend of P3HT/PTB-7 (wt. ratio: 1:0.2) and pure PTB-7. All the spectra were collected under excitation at 522 nm (absorption maximum of P3HT film). The curve labeled with ▽ displays PL spectra of PTB-7 film multiplied by 5 times for guidance about PTB-7 emission profile. The curve labeled with ■ is made by an addition of 89% quenched P3HT spectrum and pure PTB spectrum for comparison with the spectra of the binary film of P3HT/PTB-7. All the spectra were obtained under excitation of 522 nm, which is the absorption maximum of pure P3HT film.

J-V and EQE characterization

Figure 7. 4 demonstrates photocurrent density-voltage (J-V) characteristics of the ternary P3HT/PTB-7/$PC_{60}BM$ solar cells and P3HT/ $PC_{60}BM$ control cells under dark and illuminated conditions in (a) and (b), respectively. Note that all these cells were prepared in the same run so they can be used for comparison. For the dark J-V curves (Figure 7. 4(a)), it is found that all the devices exhibit low dark current. Compared with cells without DIO additive, the DIO processed cells show higher rectification ratio, indicative of better performance of the devices prepared with DIO. The J-V characteristics of devices under AM 1.5 G illumination condition are summarized in

Figure 7. 4(b). The averaged device parameters of the solar cells under illumination are summarized in Table 7. 1. For the P3HT/$PC_{60}BM$ control cell, the quick drying process and the absence of post-annealing result in an average J_{sc} of 3.94 mA/cm^2, a V_{oc} of 0.56 V and a FF of 0.37, leading to a poor power conversation efficiency (PCE) of 0.80%. In contrast, the performance of cell prepared with DIO has been significantly improved to an average PCE of 2.84%. As can be seen from Table 7. 1 and Figure 7. 4 (b), the performance enhancement is mainly due to significant improvements of J_{sc} and FF. The averaged J_{sc} has been improved from 3.94 mA/cm^2 to 10.55 mA/cm^2 when the cell was processed with DIO additive. The FF has been improved from 0.33 to 0.49 on average, while the V_{oc} value slightly reduced by 0.01 V.

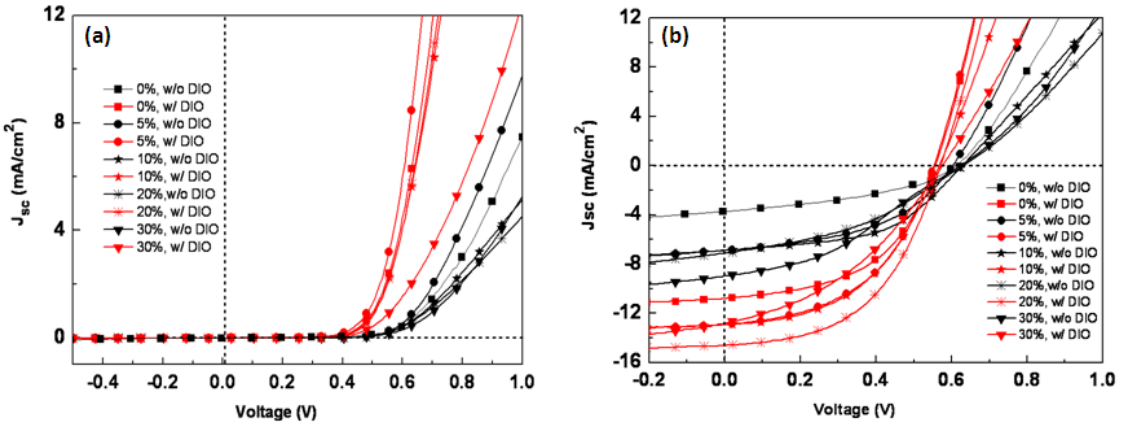

Figure 7. 4 Photocurrent density-voltage (J-V) curves of the best devices under dark (a) and under AM 1.5G illumination (b) at an irradiation intensity of 100 mW/cm^2. The doping levels (wt%) of PTB-7 in the P3HT/$PC_{60}BM$ cells are labeled in each figure. The J-V curves for devices without and with DIO are shown as black and red, respectively.

Table 7. 1 Device performance parameters of cells incorporating various concentrations (from 5-30%) of PTB-7 processed without (w/o) and with (w/) DIO additive. The PTB-7 doping levels as well as the processing condition (i.e. without (w/o) and with (w/) DIO additive) are listed in the top row. The device parameters shown are obtained by averaging over 5-9 devices. The pink and the white columns display the parameters for the cells processed without and with DIO, respectively. The numbers before (in bold) and after slash are averaged values and standard deviations, respectively. *Note that all these devices were prepared in the same run.*

	0% w/o DIO	0% w/ DIO	5% w/o DIO	5% w/ DIO	10% w/o DIO	10% w/ DIO	20% w/o DIO	20% w/ DIO	30% w/o DIO	30% w/ DIO
Jsc (mA/cm^2)	**3.94**/0.76	**10.55**/0.27	**6.00**/0.61	**11.06**/1.30	**6.84**/0.07	**11.44**/1.96	**6.10**/0.52	**14.00**/0.71	**7.02**/1.22	**12.96**/0.22
Voc (V)	**0.56**/0.07	**0.55**/0.01	**0.62**/0.01	**0.56**/0.00	**0.63**/0.00	**0.57**/0.00	**0.63**/0.00	**0.57**/0.00	**0.63**/0.00	**0.58**/0.00
FF	**0.37**/0.03	**0.49**/0.02	**0.45**/0.02	**0.49**/0.01	**0.48**/0.04	**0.47**/0.01	**0.34**/0.03	**0.47**/0.02	**0.34**/0.02	**0.36**/0.04
PCE (%)	**0.80**/0.09	**2.84**/0.16	**1.65**/0.21	**3.03**/0.39	**2.04**/0.17	**3.05**/0.59	**1.32**/0.22	**3.75**/0.30	**1.53**/0.32	**2.67**/0.23

For the cells without DIO additive, the introduction of PTB-7 results in improvement of PCE for all the PTB-7 doping levels investigated. However, 10 wt% PTB-7 doped cell yields the best performance with an efficiency of 2.04%. Although 30 wt% doped device shows a higher J_{sc} than other devices, the PCE is hampered by its low FF, which is reflected by the appearance of an S-shaped J-V curve displayed in Figure 7. 4. This kind of abnormal J-V curve can be attributed to unbalanced charge transport/collection due to factors such as vertical phase separation or unfavorable contacts.[14,273] Another interesting phenomenon is that with the doping of PTB-7 there is a slight increase in V_{oc}, i.e. from 0.57 V for the undoped device to 0.63 V for the 10-30% devices. Similar V_{oc} increases have been reported by Peet et al and been attributed to a slightly lowered HOMO level of P3HT caused by a decreased order in

P3HT domain.[47] Another factor for the V_{oc} enhancement might involve the low HOMO level of PTB-7.

With respect to the PTB-7 doped devices without DIO, the additive processed and PTB-7 doped cells exhibit increase in performance, analogous to the improvement found for the undoped device after incorporation of DIO. For the 5 wt% and 10 wt% PTB-7 doped devices, the efficiencies have increased from 1.65% to 3.03%, and 2.04% to 3.05%, respectively. Although the 20 wt% PTB-7 doped device without DIO shows lower efficiency than the 5 wt% and 10 wt% doped ones, the introduction of DIO has improved the performance significantly from 1.32% to 3.75% for the 20 wt% PTB-7 doped cells. The best device performance efficiency of 4.2% (Figure 7. 4, 20%, w/DIO) has been achieved in the 20 wt% PTB-7 doped samples processed with DIO. Compared with the undoped cell with DIO, the J_{sc} of the 20 wt% doped device has been increased by ~ 30% while the V_{oc} and FF values remain similar. Although the 30 wt% PTB -7 doping results in S-shaped J-V curve in P3HT/PC_{60}BM cell processed without DIO, after the incorporation of DIO it can found that the S-shape has virtually disappeared. However, the final efficiency of the 30 wt% PTB -7 doped cells with DIO is still less than that of the 20 wt% doped cells due to lower FF and J_{sc}. This observation is presumably due a poorer active layer morphology compared to the DIO processed 20 wt% doped PTB-7 solar cells. This is illustrated below with AFM data.

To identify the contribution of PTB-7 to the photocurrent increase in the doped cells,

EQE experiments were carried out. As shown in Figure 7. 5, for the cells without DIO additive, the doping of PTB-7 results in a significant EQE contribution in the wavelength range of 650 nm to 800 nm. In addition, in the region of 350 nm to 650 nm, there is a slight increase in EQE as well, which could be caused by a well-defined phase separation in the doped cells as will be shown in AFM imaging. The DIO additive processed cells exhibit a significant EQE enhancement compared to the cells without DIO, suggesting an efficient control over the morphology and phase separation induced by the additive for both P3HT and PTB-7. The EQE values for all the cells measured are lower than the value expected due to a quick device degradation in air since both the J-V and EQE data were collected in ambient atmosphere and the devices were not encapsulated.

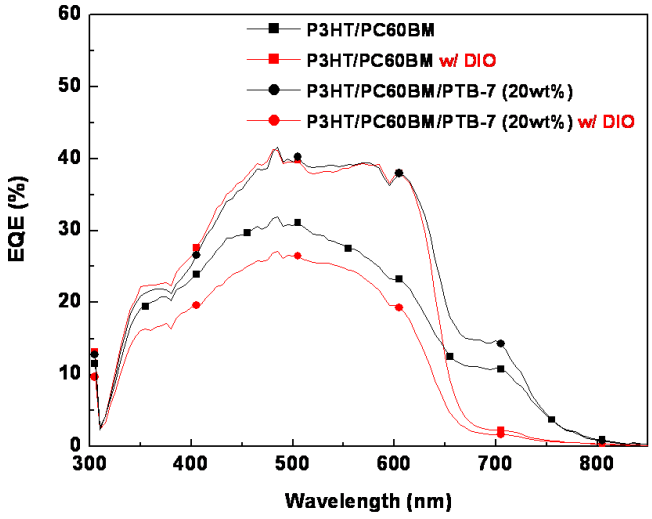

Figure 7. 5 EQE spectra of P3HT/PC_{60}BM cells without and with DIO are shown as black and red curves, respectively. The undoped P3HT/PC_{60}BM cells and the 20 wt% PTB-7 doped cells are labeled with filled square and circle, respectively.

AFM Imaging

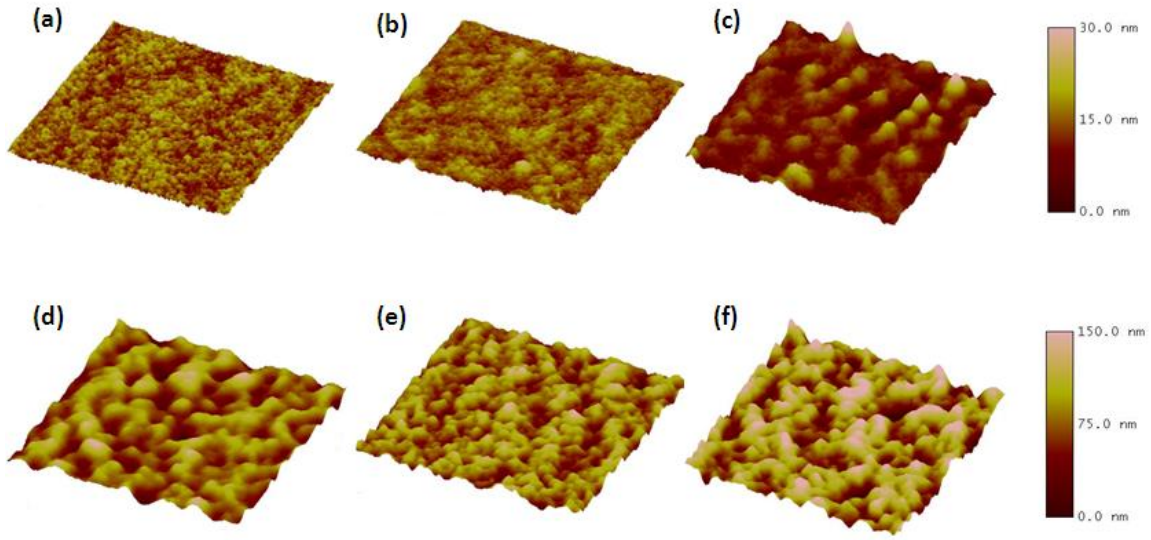

Figure 7. 6 AFM topography images of the surface of active layers. No DIO processed film: (a) P3HT/$PC_{60}BM$, (b) 20 wt% PTB-7 doped P3HT/$PC_{60}BM$ and (c) 30 wt% PTB-7 doped P3HT/$PC_{60}BM$. DIO processed film: (d) P3HT/$PC_{60}BM$, (e) 20 wt% PTB-7 doped P3HT/$PC_{60}BM$ and (f) 30 wt% PTB-7 doped P3HT/$PC_{60}BM$. The image dimensions are 5.0 × 5.0 μm^2. The scale bar is 30 nm for (a)-(c), 150 nm for (d)-(f), respectively.

The morphology of the active layer surface has been studied with AFM (Figure 7. 6) to understand the relation between morphology and device performance. For the active layer without DIO additive and PTB-7, the surface is relatively smooth as can be seen from Figure 7. 6(a). Doping with PTB-7 leads to a rougher surface (Figure 7. 6(e) and (f)) compared with the undoped device (Figure 7. 6(b) and (c)), especially for the 30 wt% doped sample, which is probably caused by a demixing process between these two polymers.[48] The active layers for both the binary and ternary devices

processed with DIO, however, display a very rough surface topography as can be seen in Figure 7. 6(d)-(e) for the undoped, 20 wt% and 30 wt% doped P3HT/PC_{60}BM films, respectively. The rough surface has also been observed in post-annealed P3HT/PC_{60}BM films and assigned to polymer self-organization into ordered structure in the film.[110] Comparing the images of Figure 7. 6(d) and (f) with (e), we can find that the doping of PTB-7 at 20 wt% in the ternary blend leads to a better defined surface topography, which probably can benefit a close contact between the active layer and deposited cathode. Figure 7. 7 demonstrate AFM phase images taken with scan area of 500 nm × 500 nm. For the P3HT/PC_{60}BM film processed without DIO, we can find that the phase separation is not well developed (Figure 7. 7(a)). PTB-7 doping shows pronounced effects on phase separation as demonstrated in Figure 7. 7(b) and (c) for 20 wt% and 30 wt% PTB-7 doped samples, in which domains with a size of ~ 10-20 nm are developed, respectively. Compared with the films without DIO, well-defined nanometer scale phase separation has been formed in the films with DIO, which is favorable for the charge carrier generation at the polymer/fullerene interface. The doping of PTB-7 in the presence of DIO additive exhibits an analogous effect on phase separation in ternary blends. Severe phase separation occurs for the 30 wt% PTB-7 doped films, which can explain the low FF observed for corresponding device.

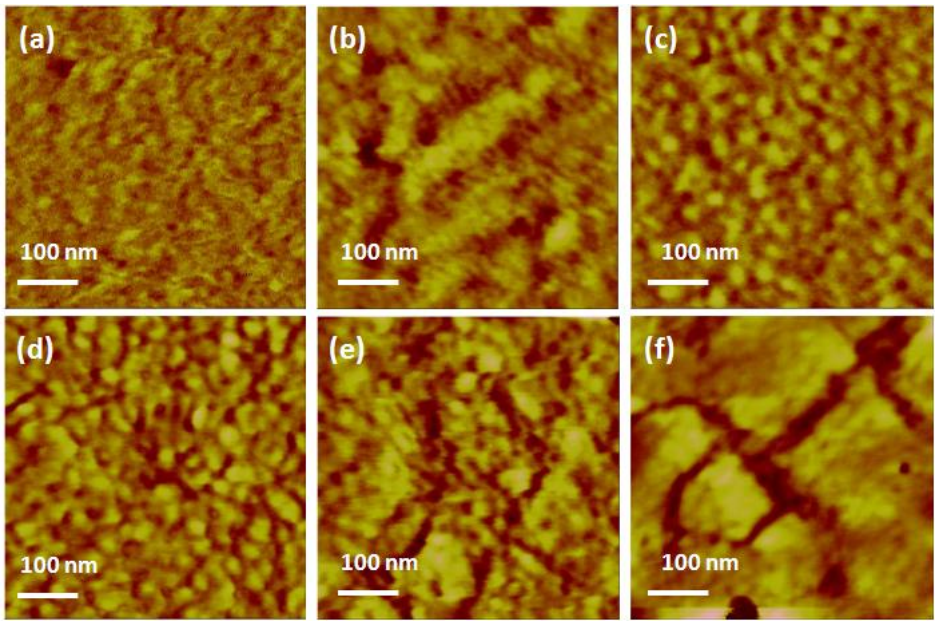

Figure 7. 7 AFM phase images for active layer surface with a scan range of 500 nm × 500 nm. (a) P3HT/PC_{60}BM device without DIO. (b) P3HT/PC_{60}BM device with DIO. (c) P3HT/PC_{60}BM device doped with 20 wt% PTB-7 without DIO. (d) P3HT/PC_{60}BM device doped with 20 wt% PTB-7 with DIO. The phase angle scale is 3° for (a) and 30° for (b)-(d), respectively.

7.2.2 Sensitization by small molecule dye (SMD)

Absorption and photoluminescence (PL) spectroscopy of active layers

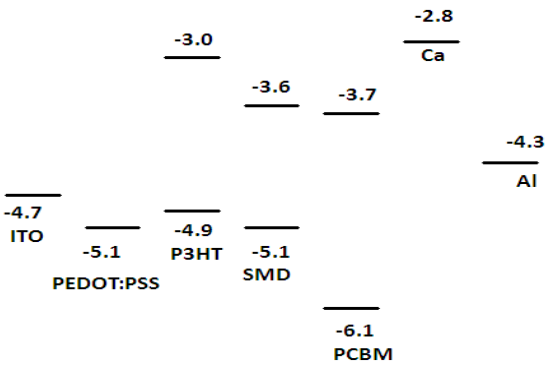

Figure 7. 8 Energy-level diagram showing the HOMO and LUMO energies of semiconductor components and the work function of electrode materials in SMD doped device.

Figure 7. 8 presents an energy diagram for materials in the ternary blended P3HT/PC_{60}BM/SMD solar cells. As can be seen, the LUMO level of the SMD is located in the middle of the LUMO levels of P3HT and PC_{60}BM, while the HOMO level is close to that of P3HT. The absorption spectra of P3HT/PC_{60}BM films with different SMD doping levels are plotted in Figure 7. 9. As can be observed, with the

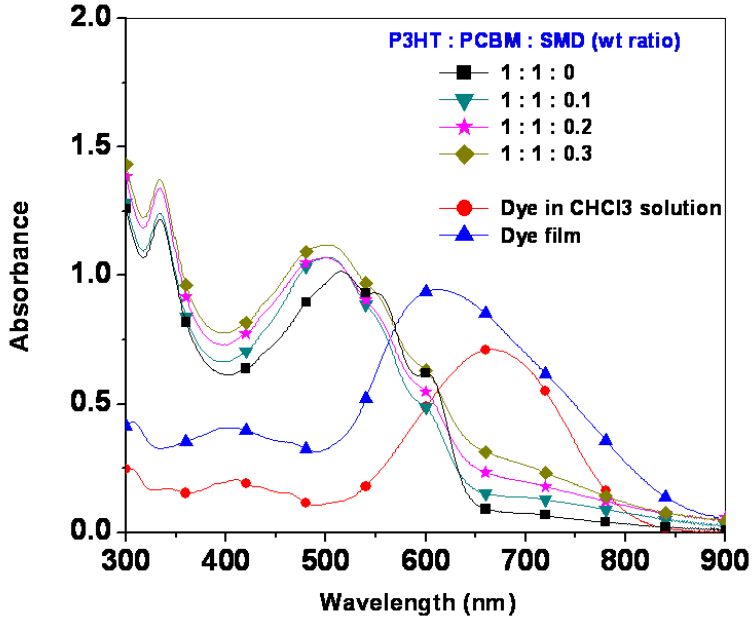

Figure 7. 9 Absorption spectra of P3HT/PC_{60}BM films doped with different levels of the SMD. The absorption profiles of pure dye film (spin cast from chloroform solution) and dye chloroform solution are also shown.

addition of the SMD, there is a corresponding absorption increase in the NIR region. However, the incorporation of the SMD induces an obvious blue shift for the P3HT absorption, indicating a disruption of the ordered P3HT structure upon dye addition,[34] which can be substantiated by AFM topography imaging shown Figure 7. 12. To

check possible electron or energy transfer process between P3HT and dye, PL spectra of films were collected and are displayed in Figure 7. 10. The films were prepared with chloroform solutions because the SMD cannot form a continuous film when processed with DCB. Compared with pure P3HT film, the 10 wt% SMD doped P3HT film exhibits PL quenching of about 3 times under excitation of 551 nm, which is the absorption peak wavelength of P3HT film spin cast from chloroform solution. This PL quenching in the doped P3HT film is not accompanied by new emission features. To check the photoluminescence of the dye, the dye film was also prepared and excited with its absorption maximum wavelength of 626 nm; however, no fluorescence signal could be detected. This indicates that the P3HT PL quenching is mainly caused by photoinduced electron transfer from P3HT to the SMD. The low photoluminescence quantum yield of the SMD is probably due to formation of H-aggregates because the dye film exhibits a strong blue shift compared to its solution counterpart (Figure 7. 9).[274,275]

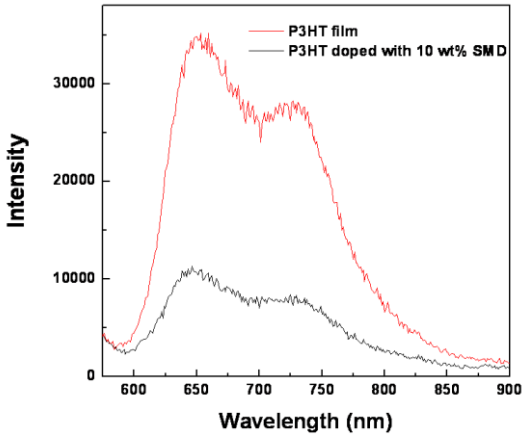

Figure 7. 10 Photoluminescence spectra collected for P3HT film and 10 wt% SMD doped P3HT film under 551 nm excitation.

J-V characterization

Figure 7. 11 exhibit the J-V curves for the devices with different SMD doping levels. The averaged device parameters are summarized in Table 7. 2. The undoped device exhibits a decent power conversion efficiency of 3.66%. However, with the introduction of SMD (even with 5 wt% doping level) in to the binary P3HT/PC_{60}BM cell, there is a dramatic decrease in PCE, which is mainly due to a strong degradation of FF as can be seen from *S*-shaped J-V curves for the doped devices. As shown in Table 7. 2, for the device with P3HT:PC_{60}BM:SMD a weight ratio of 1:1:0.2, the FF drops to only half of FF of the control cell. In addition to FF reduction, with the doping level increase, J_{sc} values also drop significantly and V_{oc} values slightly reduce. FF in solar cells is directly controlled by balanced charge transport and collection, which, in polymer-fullerene OPVs, are dominated by the morphology of the active layer and the active layer-metal contact.[276] Such *S*-shaped J-V curves and poor device performance have been reported in zinc phthalocyanine derivative (ZnPc) dope P3HT/PC_{60}BM cells and ascribed to the formation of dye aggregates in and poor morphology of the blended active layers.[92] These issues were investigated further with AFM imaging of the active layer morphology.

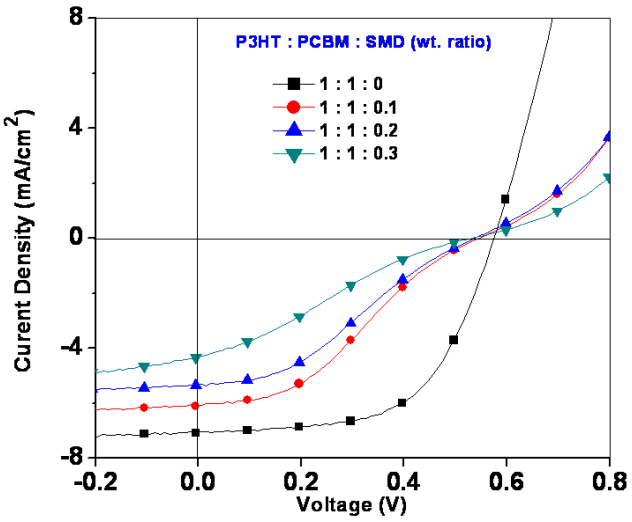

Figure 7. 11 Photocurrent density-voltage (J-V) curves of devices under AM 1.5G illumination at an irradiation intensity of 65 mW/cm^2. The different doping levels of SMD in the P3HT/PC_{60}BM cells are indicated in the figure.

Table 7. 2 Averaged device performance parameters of cells incorporating various concentrations (from 10-30%) of SMD. The data are collected under AM 1.5G illumination at an irradiation intensity of 65 mW/cm^2. The numbers before (in bold) and after slash are averaged values and standard deviations, respectively. *Note that all these devices were prepared in the same run.*

wt. ratio P3HT:PCBM:SMD	J_{sc} (mA/cm^2)	V_{oc} (V)	FF	PCE (%)
1:1:0	**7.02**/0.48	**0.58**/0.01	**0.59**/0.04	**3.66**/0.43
1:1:0.1	**5.85**/0.25	**0.54**/0.01	**0.33**/0.05	**1.63**/0.29
1:1:0.2	**5.04**/0.39	**0.54**/0.00	**0.30**/0.04	**1.27**/0.28
1:1:0.3	**4.51**/0.34	**0.52**/0.01	**0.27**/0.03	**0.99**/0.17

AFM imaging

To investigate the possible correlation between the device performance and active

layer morphology, AFM topography images of the control P3HT/PC_{60}BM film and SMD doped P3HT/PC_{60}BM films were collected and are displayed in Figure 7. 12.

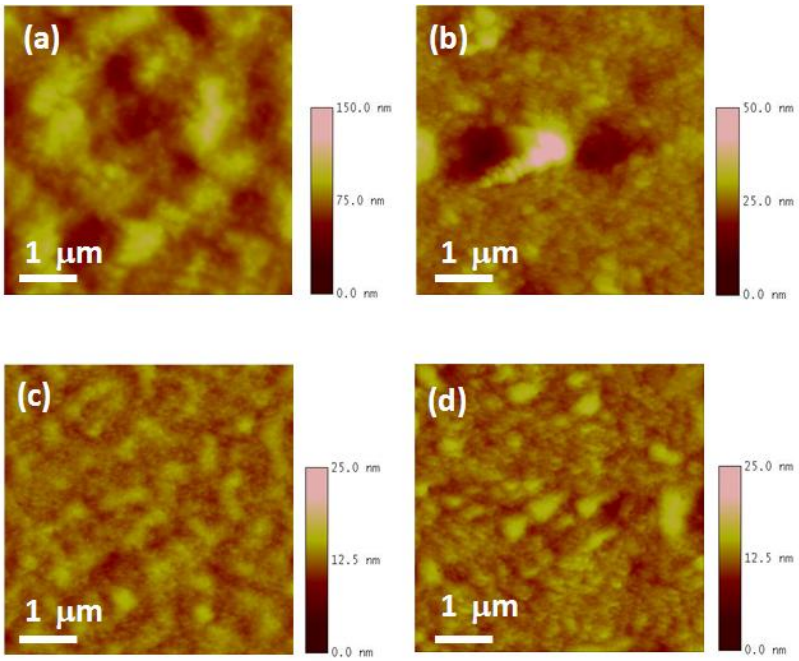

Figure 7. 12 AFM tapping mode topography images of P3HT/PC_{60}BM films with different SMD doping levels. (a) Undoped P3HT/PC_{60}BM film. (b) 10 wt% SMD doped P3HT/PC_{60}BM film. (c) 20 wt% doped P3HT/PC_{60}BM. (d) 30 wt% SMD doped P3HT/PC_{60}BM film. The scan range for all the images is 5 μm × 5 μm. The height scale bar is shown to the right of each image.

The P3HT/PC_{60}BM film exhibits a very rough surface topography, indicative of self-organization of polymer in the binary blend film due to the solvent annealing process employed in the active layer preparation.[34] With the introduction of the SMD to the binary blend of P3HT/PC_{60}BM, the surface becomes more and more smooth. This indicates a disruption of the polymer organized structure due to the SMD

incorporation. In addition, for ternary blend films with 20 wt% and 30 wt% SMD doping levels, approximately spherical or elliptical aggregates appear in the corresponding AFM topography images, which can be assigned to the phase separation caused by the SMD doping.

7.3 Conclusion

With the aim of extending the photoresponse region of the prototypical P3HT/PC_{60}BM system into the NIR region, P3HT/PC_{60}BM cells incorporating near-IR absorbing low band gap polymer PTB-7 and a small molecule dye were fabricated. It was revealed that the incorporation of PTB-7 can significantly increase the NIR region photoresponse and therefore device performance. In addition, solvent additive 1,8-diiodooctane (DIO) was applied in this system to optimize the phase separation while simplifying the device fabrication process. Data for devices fabricated with DIO additive demonstrate that the incorporation of PTB-7 in the P3HT/PC_{60}BM cells can improve the device PCE by about 32% compared with the P3HT/PC_{60}BM cell without PTB-7. A ~ 255% increase in the short-circuit current and a ~ 369% increase in final device performance is found compared to the reference P3HT/PC_{60}BM cell processed without DIO. In contrast to the performance enhancement observed in the PTB-7 doped OPVs, the doping of the small molecule dye deteriorates the device performance mainly due to destruction of P3HT ordered structures in the ternary active layer of these devices.

APPENDIX: LIST OF PUBLICATIONS

Gesquiere, A. J.; Tenery, D.; Hu, Z.J. *Single-Particle Spectroscopy on Conducting Polymer-Fullerene Composite Materials for Application in Organic Photovoltaic Devices.* Spectroscopy. **2008**, 23, 32-44.

Tenery, D.; Worden, J.G.; Hu, Z.J.; Gesquiere, A.J. *Single Particle Spectroscopy on Composite MEH-PPV/$PC_{60}BM$ Nanoparticles.* Journal of Luminescence. **2009**, 129,423-429.

Hu, Z. J.; Gesquiere, A. J. *$PC_{60}BM$ Concentration Dependent Morphology of P3HT in Composite P3HT/$PC_{60}BM$ Nanoparticles*. Chemical Physics Letters. **2009**, *476,* 51.

Hu, Z. J.; Zou, J. H.; Deibel, C.; Gesquiere, A. J.; Zhai, L. *Single-Molecule Spectroscopy and AFM Morphology Studies of a Diblock Copolymer Consisting of Poly(3-hexylthiophene) and Fullerene.* Macromolecular Chemistry and Physics. **2010**, *211*, 2416

Hu, Z. J.; Tenery, D.; Bonner, M. S.; Gesquiere, A. J. *Correlation between Spectroscopic and Morphological Properties of Composite P3HT/$PC_{60}BM$ Nanoparticles Studied by Single Particle Spectroscopy.* Journal of Luminescence. **2010**, *130,* 771.

Hu, Z. J.; Gesquiere, A. J. *Charge Trapping and Storage by Composite P3HT/$PC_{60}BM$ Nanoparticles Investigated by Fluorescence-Voltage/Single Particle Spectroscopy.* Nano Letters. Submitted.

Hu, Z. J.; Gesquiere, A. J. *The Effect of Fullerene on the Morphology of Conjugated Polymer Single Molecules and Nanoparticles. Reviews in Nanoscience and Nanotechnology.* Under preparation.

Hu, Z. J.; Bower, L. S.; Liu, J. H.; Zhai, L.; Gesquiere, A. J. *Single Molecule Spectroscopy Investigations on Thiophene-based Conjugated Polymers with Different Macroscale Crystalline Behaviors*. Under preparation.

Hu, Z. J.; Tang, S.; Gesquiere, A. J. *Improving Photoresponse in Near-Infrared Region of P3HT/$PC_{60}BM$ Photovoltaics by Low Band Gap Polymer*. Under preparation.

RFERENCES

1. Chiang, C. K.; Fincher, C. R.; Park, Y. W.; Heeger, A. J.; Shirakawa, H.; Louis, E. J.; Gau, S. C.; Macdiarmid, A. G. *Electrical conductivity in doped polyacetylene*. Physical Review Letters **1977,** 39, (17), 1098-1101.
2. Shirakawa, H.; Louis, E. J.; Macdiarmid, A. G.; Chiang, C. K.; Heeger, A. J. *Synthesis of electrically conducting organic polymers: halogen derivatives of polyacetylene, $(CH)_X$*. Journal of the Chemical Society-Chemical Communications **1977**, (16), 578-580.
3. Perepichka, I. F.; Perepichka, D. F., *Handbook of thiophene-based materials*. Wiley: Hoboken, 2009.
4. Skotheim, T. A.; Reynolds, J. R., *Handbook of conducting polymers. Conjugated polymers : theory, synthesis, properties, and characterization*. 3rd ed.; CRC Press: Boca Raton, 2007.
5. Brabec, C. J.; Dyakonov, V.; Scherf, U., *Organic photovoltaics : materials, device physics, and manufacturing technologies*. Wiley-VCH: Weinheim, 2008; p xxi, 575 p.
6. Bao, Z.; Locklin, J. J., *Organic field-effect transistors*. CRC Press: Boca Raton, 2007; p 616 p., 2 p. of plates.
7. Müllen, K.; Scherf, U., *Organic light-emitting devices : synthesis, properties, and applications*. Wiley-VCH: Weinheim, 2006; p xvii, 410 p.
8. Barford, W., *Electronic and optical properties of conjugated polymers*. Clarendon Press: Oxford, 2005; p xv, 262 p.
9. Sariciftci, N. S., *Primary photoexcitations in conjugated polymers : molecular excitation versus semiconductor band model*. World Scientific: Singapore ; River Edge, NJ, 1997; p 621 p.
10. Lupton, J. M. *Single-Molecule Spectroscopy for Plastic Electronics: Materials Analysis from the Bottom-Up*. Advanced Materials **2010,** 22, (15), 1689-1721.
11. Vacha, M.; Habuchi, S. *Conformation and physics of polymer chains: a single-molecule perspective*. NPG Asia Materials **2010,** 2, 134-1142.
12. Moulé, A. J.; Meerholz, K. *Controlling Morphology in Polymer–Fullerene Mixtures*. Advanced Materials **2008,** 20, (2), 240-245.
13. Barbara, P. F.; Gesquiere, A. J.; Park, S. J.; Lee, Y. J. *Single-molecule spectroscopy of conjugated polymers*. Accounts of Chemical Research **2005,** 38, (7), 602-610.
14. de Villers, B. T.; Tassone, C. J.; Tolbert, S. H.; Schwartz, B. J. *Improving the Reproducibility of P3HT:PCBM Solar Cells by Controlling the PCBM/Cathode Interface*. Journal of Physical Chemistry C **2009,** 113, (44), 18978-18982.
15. Sugimoto, T.; Ebihara, Y.; Ogino, K.; Vacha, M. *Structure-dependent photophysics studied in single molecules of polythiophene derivatives*.

Chemphyschem **2007,** 8, (11), 1623-1628.
16. Thompson, B. C.; Fréchet, J. M. J. *Polymer–Fullerene Composite Solar Cells*. Angewandte Chemie International Edition **2008,** 47, (1), 58-77.
17. Brabec, C. J.; Gowrisanker, S.; Halls, J. J. M.; Laird, D.; Jia, S.; Williams, S. P. *Polymer-Fullerene Bulk-Heterojunction Solar Cells*. Advanced Materials **2010,** 22, (34), 3839-3856.
18. Dennler, G.; Scharber, M. C.; Brabec, C. J. *Polymer-Fullerene Bulk-Heterojunction Solar Cells*. Advanced Materials **2009,** 21, (13), 1323-1338.
19. Liang, Y. Y.; Xu, Z.; Xia, J. B.; Tsai, S. T.; Wu, Y.; Li, G.; Ray, C.; Yu, L. P. *For the Bright Future-Bulk Heterojunction Polymer Solar Cells with Power Conversion Efficiency of 7.4%*. Advanced Materials **2010,** 22, (20), E135-+.
20. Thompson, B. C.; Frechet, J. M. J. *Organic photovoltaics - Polymer-fullerene composite solar cells*. Angewandte Chemie-international Edition **2008,** 47, (1), 58-77.
21. Clarke, T. M.; Durrant, J. R. *Charge Photogeneration in Organic Solar Cells*. Chemical Reviews **2010,** 110, (11), 6736-6767.
22. Sariciftci, N. S.; Smilowitz, L.; Heeger, A. J.; Wudl, F. *Photoinduced Electron-Transfer from a Conducting Polymer to Buckminsterfullerene*. Science **1992,** 258, (5087), 1474-1476.
23. Tang, C. W. *2-Layer Organic Photovoltaic Cell*. Applied Physics Letters **1986,** 48, (2), 183-185.
24. Park, S. H.; Roy, A.; Beaupre, S.; Cho, S.; Coates, N.; Moon, J. S.; Moses, D.; Leclerc, M.; Lee, K.; Heeger, A. J. *Bulk heterojunction solar cells with internal quantum efficiency approaching 100%*. Nature Photonics **2009,** 3, (5), 297-U5.
25. Mihailetchi, V. D.; Xie, H. X.; de Boer, B.; Koster, L. J. A.; Blom, P. W. M. *Charge transport and photocurrent generation in poly (3-hexylthiophene): Methanofullerene bulk-heterojunction solar cells*. Advanced Functional Materials **2006,** 16, (5), 699-708.
26. Skotheim, T. A.; Reynolds, J. R., *Handbook of conducting polymers. Conjugated polymers : processing and applications*. 3rd ed.; CRC Press: Boca Raton, 2007.
27. Chen, L. M.; Xu, Z.; Hong, Z. R.; Yang, Y. *Interface investigation and engineering - achieving high performance polymer photovoltaic devices*. Journal of Materials Chemistry **2010,** 20, (13), 2575-2598.
28. Xu, Z.; Chen, L. M.; Yang, G. W.; Huang, C. H.; Hou, J. H.; Wu, Y.; Li, G.; Hsu, C. S.; Yang, Y. *Vertical Phase Separation in Poly(3-hexylthiophene): Fullerene Derivative Blends and its Advantage for Inverted Structure Solar Cells*. Advanced Functional Materials **2009,** 19, (8), 1227-1234.
29. Li, G.; Shrotriya, V.; Yao, Y.; Huang, J. S.; Yang, Y. *Manipulating regioregular poly(3-hexylthiophene): 6,6 -phenyl-C-61-butyric acid methyl ester blends -*

route towards high efficiency polymer solar cells. Journal Of Materials Chemistry **2007,** 17, (30), 3126-3140.

30. Liao, H. H.; Chen, L. M.; Xu, Z.; Li, G.; Yang, Y. *Highly efficient inverted polymer solar cell by low temperature annealing of Cs2CO3 interlayer*. Applied Physics Letters **2008,** 92, (17).
31. Li, G.; Chu, C. W.; Shrotriya, V.; Huang, J.; Yang, Y. *Efficient inverted polymer solar cells*. Applied Physics Letters **2006,** 88, (25).
32. Hu, Z.; Tenery, D.; Bonner, M. S.; Gesquiere, A. J. *Correlation between spectroscopic and morphological properties of composite P3HT/PCBM nanoparticles studied by single particle spectroscopy*. Journal Of Luminescence **2010,** 130, (5), 771-780.
33. Dante, M.; Garcia, A.; Nguyen, T. Q. *Three-Dimensional Nanoscale Organization of Highly Efficient Low Band-Gap Conjugated Polymer Bulk Heterojunction Solar Cells*. Journal of Physical Chemistry C **2009,** 113, (4), 1596-1600.
34. Li, G.; Shrotriya, V.; Huang, J.; Yao, Y.; Moriarty, T.; Emery, K.; Yang, Y. *High-efficiency solution processable polymer photovoltaic cells by self-organization of polymer blends*. Nature Materials **2005,** 4, (11), 864-868.
35. Ma, W. L.; Yang, C. Y.; Gong, X.; Lee, K.; Heeger, A. J. *Thermally stable, efficient polymer solar cells with nanoscale control of the interpenetrating network morphology*. Advanced Functional Materials **2005,** 15, (10), 1617-1622.
36. Peet, J.; Soci, C.; Coffin, R. C.; Nguyen, T. Q.; Mikhailovsky, A.; Moses, D.; Bazan, G. C. *Method for increasing the photoconductive response in conjugated polymer/fullerene composites*. Applied Physics Letters **2006,** 89, (25).
37. Sista, S.; Park, M. H.; Hong, Z. R.; Wu, Y.; Hou, J. H.; Kwan, W. L.; Li, G.; Yang, Y. *Highly Efficient Tandem Polymer Photovoltaic Cells*. Advanced Materials **2010,** 22, (3), 380-+.
38. Ameri, T.; Dennler, G.; Lungenschmied, C.; Brabec, C. J. *Organic tandem solar cells: A review*. Energy & Environmental Science **2009,** 2, (4), 347-363.
39. Kim, J. Y.; Lee, K.; Coates, N. E.; Moses, D.; Nguyen, T. Q.; Dante, M.; Heeger, A. J. *Efficient tandem polymer solar cells fabricated by all-solution processing*. Science **2007,** 317, (5835), 222-225.
40. Meillaud, F.; Shah, A.; Droz, C.; Vallat-Sauvain, E.; Miazza, C. *Efficiency limits for single junction and tandem solar cells*. Solar Energy Materials And Solar Cells **2006,** 90, (18-19), 2952-2959.
41. Park, S. H.; Roy, A.; Beaupré, S.; Cho, S.; Coates, N.; Moon, J. S.; Moses, D.; Leclerc, M.; Lee, K.; Heeger, A. J. *Bulk heterojunction solar cells with internal quantum efficiency approaching 100%*. Nature Photonics **2009,** 3, (5), 297-302.
42. Roncali, J. *Molecular Engineering of the Band Gap of π-Conjugated Systems:*

Facing Technological Applications. Macromolecular Rapid Communications **2007,** 28, (17), 1761-1775.

43. Liang, Y. Y.; Feng, D. Q.; Wu, Y.; Tsai, S. T.; Li, G.; Ray, C.; Yu, L. P. *Highly Efficient Solar Cell Polymers Developed via Fine-Tuning of Structural and Electronic Properties*. Journal of the American Chemical Society **2009,** 131, (22), 7792-7799.
44. Muhlbacher, D.; Scharber, M.; Morana, M.; Zhu, Z. G.; Waller, D.; Gaudiana, R.; Brabec, C. *High photovoltaic performance of a low-bandgap polymer (vol 18, pg 2884, 2006)*. Advanced Materials **2006,** 18, (22), 2931-2931.
45. Peet, J.; Kim, J. Y.; Coates, N. E.; Ma, W. L.; Moses, D.; Heeger, A. J.; Bazan, G. C. *Efficiency enhancement in low-bandgap polymer solar cells by processing with alkane dithiols*. Nature Materials **2007,** 6, (7), 497-500.
46. Chen, C. P.; Chan, S. H.; Chao, T. C.; Ting, C.; Ko, B. T. *Low-bandgap poly(thiophene-phenylene-thiophene) derivatives with broaden absorption spectra for use in high-performance bulk-heterojunction polymer solar cells*. Journal Of The American Chemical Society **2008,** 130, (38), 12828-12833.
47. Peet, J.; Tamayo, A. B.; Dang, X. D.; Seo, J. H.; Nguyen, T. Q. *Small molecule sensitizers for near-infrared absorption in polymer bulk heterojunction solar cells*. Applied Physics Letters **2008,** 93, (16), 163306.
48. Koppe, M.; Egelhaaf, H.-J.; Dennler, G.; Scharber, M. C.; Brabec, C. J.; Schilinsky, P.; Hoth, C. N. *Near IR Sensitization of Organic Bulk Heterojunction Solar Cells: Towards Optimization of the Spectral Response of Organic Solar Cells*. Advanced Functional Materials **2010,** 20, (2), 338-346.
49. Mark Dante; Changduk Yang; Bright Walker; Fred Wudl; Nguyen, T.-Q. *Self-Assembly and Charge-Transport Properties of a Polythiophene-Fullerene Triblock Copolymer*. Advanced Materials **2010,** 22, (16), 1835-1839.
50. Liu, C.-Y.; Holman, Z. C.; Kortshagen, U. R. *Optimization of Si NC/P3HT Hybrid Solar Cells*. Advanced Functional Materials **2010,** 20, (13), 2157-2164.
51. Chamberlain, G. A. *Organic Solar-Cells - a Review*. Solar Cells **1983,** 8, (1), 47-83.
52. Zhao, J. H.; Wang, A. H.; Green, M. A.; Ferrazza, F. *19.8% efficient "honeycomb" textured multicrystalline and 24.4% monocrystalline silicon solar cells*. Applied Physics Letters **1998,** 73, (14), 1991-1993.
53. Brabec, C. J.; Sariciftci, N. S.; Hummelen, J. C. *Plastic solar cells*. Advanced Functional Materials **2001,** 11, (1), 15-26.
54. Oregan, B.; Gratzel, M. *A low-cost, high-efficiency solar cell based on dye-sensitized colloidal TiO_2 films*. Nature **1991,** 353, (6346), 737-740.
55. Hagfeldt, A.; Gratzel, M. *Molecular photovoltaics*. Accounts Of Chemical Research **2000,** 33, (5), 269-277.
56. Gratzel, M. *Dye-sensitized solar cells*. Journal of Photochemistry and Photobiology C-Photochemistry Reviews **2003,** 4, (2), 145-153.

57. Gunes, S.; Neugebauer, H.; Sariciftci, N. S. *Conjugated polymer-based organic solar cells*. Chemical Reviews **2007,** 107, (4), 1324-1338.
58. Peumans, P.; Yakimov, A.; Forrest, S. R. *Small molecular weight organic thin-film photodetectors and solar cells*. Journal Of Applied Physics **2003,** 93, (7), 3693-3723.
59. Chen, H.-Y.; Hou, J.; Zhang, S.; Liang, Y.; Yang, G.; Yang, Y.; Yu, L.; Wu, Y.; Li, G. *Polymer solar cells with enhanced open-circuit voltage and efficiency*. Nat Photon **2009,** 3, (11), 649-653.
60. http://www.konarka.com.
61. Scharber, M. C.; Mühlbacher, D.; Koppe, M.; Denk, P.; Waldauf, C.; Heeger, A. J.; Brabec, C. J. *Design Rules for Donors in Bulk-Heterojunction Solar Cells—Towards 10 % Energy-Conversion Efficiency*. Advanced Materials **2006,** 18, (6), 789-794.
62. Boudreault, P. L. T.; Najari, A.; Leclerc, M. *Processable Low-Bandgap Polymers for Photovoltaic Applications*. Chemistry Of Materials **2011,** 23, (3), 456-469.
63. Cai, W.; Gong, X.; Cao, Y. *Polymer solar cells: Recent development and possible routes for improvement in the performance*. Solar Energy Materials And Solar Cells **2010,** 94, (2), 114-127.
64. Meskers, S. C. J.; Hübner, J.; Oestreich, M.; Bässler, H. *Time-resolved fluorescence studies and Monte Carlo simulations of relaxation dynamics of photoexcitations in a polyfluorene film*. Chemical Physics Letters **2001,** 339, (3-4), 223-228.
65. Graupner, W.; Leising, G.; Lanzani, G.; Nisoli, M.; DeSilvestri, S.; Scherf, U. *Femtosecond relaxation of photoexcitations in a poly(para-phenylene)-type ladder polymer*. Physical Review Letters **1996,** 76, (5), 847-850.
66. Muller, J. G.; Lupton, J. M.; Feldmann, J.; Lemmer, U.; Scharber, M. C.; Sariciftci, N. S.; Brabec, C. J.; Scherf, U. *Ultrafast dynamics of charge carrier photogeneration and geminate recombination in conjugated polymer : fullerene solar cells*. Physical Review B **2005,** 72, (19).
67. Huser, T.; Yan, M.; Rothberg, L. J. *Single chain spectroscopy of conformational dependence of conjugated polymer photophysics*. P. Natl. Acad. Sci. USA **2000,** 97, (21), 11187-11191.
68. Vandenbout, D. A.; Yip, W. T.; Hu, D. H.; Fu, D. K.; Swager, T. M.; Barbara, P. F. *Discrete Intensity Jumps and Intramolecular Electronic Energy Transfer in the Spectroscopy of Single Conjugated Polymer Molecules*. Science **1997,** 277, (5329), 1074-1077.
69. Yu, J.; Hu, D. H.; Barbara, P. F. *Unmasking electronic energy transfer of conjugated polymers by suppression of O-2 quenching*. Science **2000,** 289, (5483), 1327-1330.
70. Gesquiere, A. J.; Park, S. J.; Barbara, P. F. *F-V/SMS: A new technique for*

studying the structure and dynamics of single molecules and nanoparticles. Journal of Physical Chemistry B **2004,** 108, (29), 10301-10308.

71. Huser, T.; Yan, M. *Solvent-related conformational changes and aggregation of conjugated polymers studied by single molecule fluorescence spectroscopy*. Journal of Photochemistry and Photobiology a-Chemistry **2001,** 144, (1), 43-51.
72. Yu, Z. H.; Barbara, P. F. *Low-temperature single-molecule spectroscopy of MEH-PPV conjugated polymer molecules*. Journal of Physical Chemistry B **2004,** 108, (31), 11321-11326.
73. De Leener, C.; Hennebicq, E.; Sancho-Garcia, J. C.; Beljonne, D. *Modeling the Dynamics of Chromophores in Conjugated Polymers: The Case of Poly (2-methoxy-5-(2 '-ethylhexyl)oxy 1,4-phenylene vinylene) (MEH-PPV)*. Journal of Physical Chemistry B **2009,** 113, (5), 1311-1322.
74. Mirzov, O.; Scheblykin, I. G. *Photoluminescence spectra of a conjugated polymer: from films and solutions to single molecules*. Physical Chemistry Chemical Physics **2006,** 8, (47), 5569-5576.
75. Hu, D. H.; Yu, J.; Wong, K.; Bagchi, B.; Rossky, P. J.; Barbara, P. F. *Collapse of stiff conjugated polymers with chemical defects into ordered, cylindrical conformations*. Nature **2000,** 405, (6790), 1030-1033.
76. Ebihara, Y.; Vacha, M. *A method for determining the absorption ellipsoid of single conjugated polymer molecules and single luminescent nanoparticles*. The Journal of Chemical Physics **2005,** 123, (24), 244710.
77. Ebihara, Y.; Vacha, M. *Relating Conformation and Photophysics in Single MEH-PPV Chains*. The Journal of Physical Chemistry B **2008,** 112, (40), 12575-12578.
78. Dedecker, P.; Muls, B.; Deres, A.; Uji-i, H.; Hotta, J.; Sliwa, M.; Soumillion, J. P.; Mullen, K.; Enderlein, J.; Hofkens, J. *Defocused Wide-field Imaging Unravels Structural and Temporal Heterogeneity in Complex Systems*. Advanced Materials **2009,** 21, (10-11), 1079-1090.
79. Bohmer, M.; Enderlein, J. *Orientation imaging of single molecules by wide-field epifluorescence microscopy*. Journal of the Optical Society of America B-Optical Physics **2003,** 20, (3), 554-559.
80. Mehta, A.; Kumar, P.; Dadmun, M. D.; Zheng, J.; Dickson, R. M.; Thundat, T.; Sumpter, B. G.; Barnes, M. D. *Oriented Nanostructures from Single Molecules of a Semiconducting Polymer: Polarization Evidence for Highly Aligned Intramolecular Geometries*. Nano Letters **2003,** 3, (5), 603-607.
81. Hoppe, H.; Niggemann, M.; Winder, C.; Kraut, J.; Hiesgen, R.; Hinsch, A.; Meissner, D.; Sariciftci, N. S. *Nanoscale morphology of conjugated polymer/fullerene-based bulk-heterojunction solar cells*. Advanced Functional Materials **2004,** 14, (10), 1005-1011.
82. Groves, C.; Reid, O. G.; Ginger, D. S. *Heterogeneity in Polymer Solar Cells:*

Local Morphology and Performance in Organic Photovoltaics Studied with Scanning Probe Microscopy. Accounts of Chemical Research **2010,** 43, (5), 612-620.

83. Pingree, L. S. C.; Reid, O. G.; Ginger, D. S. *Imaging the Evolution of Nanoscale Photocurrent Collection and Transport Networks during Annealing of Polythiophene/Fullerene Solar Cells*. Nano Letters **2009,** 9, (8), 2946-2952.
84. Nguyen, T. Q.; Schwartz, B. J.; Schaller, R. D.; Johnson, J. C.; Lee, L. F.; Haber, L. H.; Saykally, R. J. *Near-field scanning optical microscopy (NSOM) studies of the relationship between interchain interactions, morphology, photodamage, and energy transport in conjugated polymer films*. Journal of Physical Chemistry B **2001,** 105, (22), 5153-5160.
85. Coakley, K. M.; McGehee, M. D. *Conjugated polymer photovoltaic cells*. Chemistry Of Materials **2004,** 16, 4533-4542.
86. Smestad, G. P.; Krebs, F. C.; Lampert, C. M.; Granqvist, C. G.; Chopra, K. L.; Mathew, X.; Takakura, H. *Reporting solar cell efficiencies in solar energy materials and solar cells*. Solar Energy Materials and Solar Cells **2008,** 92, (4), 371-373.
87. Hoppe, H.; Sariciftci, N. S. *Organic solar cells: An overview*. Journal of Materials Research **2004,** 19, (7), 1924-1945.
88. Liang, Y. Y.; Yu, L. P. *A New Class of Semiconducting Polymers for Bulk Heterojunction Solar Cells with Exceptionally High Performance*. Accounts Of Chemical Research **2010,** 43, (9), 1227-1236.
89. Lee, J. K.; Ma, W. L.; Brabec, C. J.; Yuen, J.; Moon, J. S.; Kim, J. Y.; Lee, K.; Bazan, G. C.; Heeger, A. J. *Processing additives for improved efficiency from bulk heterojunction solar cells*. Journal of the American Chemical Society **2008,** 130, (11), 3619-3623.
90. Shrotriya, V.; Wu, E. H. E.; Li, G.; Yao, Y.; Yang, Y. *Efficient light harvesting in multiple-device stacked structure for polymer solar cells*. Applied Physics Letters **2006,** 88, (6).
91. Huang, J.-H.; Velusamy, M.; Ho, K.-C.; Lin, J.-T.; Chu, C.-W. *A ternary cascade structure enhances the efficiency of polymer solar cells*. Journal Of Materials Chemistry **2010,** 20, (14), 2820.
92. Honda, S.; Nogami, T.; Ohkita, H.; Benten, H.; Ito, S. *Improvement of the Light-Harvesting Efficiency in Polymer/Fullerene Bulk Heterojunction Solar Cells by Interfacial Dye Modification*. ACS Applied Materials & Interfaces **2009,** 1, (4), 804-810.
93. Xie, X. S. *Single-molecule spectroscopy and dynamics at room temperature*. Accounts of Chemical Research **1996,** 29, (12), 598-606.
94. Einstein, A. *Investigations on the Theory of Brownian Movement*. Ann. d. Phys **1905,** 17, 549.
95. Avouris, P. *Manipulation of Matter at the Atomic and Molecular Levels*.

Accounts Of Chemical Research **1995,** 28, (3), 95-102.

96. Hla, S. W. *Scanning tunneling microscopy single atom/molecule manipulation and its application to nanoscience and technology*. Journal Of Vacuum Science & Technology B **2005,** 23, 1351-1360.
97. Walba, D. M.; Stevens, F.; Clark, N. A.; Parks, D. C. *Detecting Molecular Chirality by Scanning Tunneling Microscopy*. Accounts Of Chemical Research **1996,** 29, (12), 591-597.
98. Moerner, W. E.; Ambrose, W. P. *Single pentacene molecules detected by fluorescence excitation in a p-terphenyl crystal - Comment*. Physical Review Letters **1991,** 66, (10), 1376-1376.
99. Orrit, M.; Bernard, J. *Single pentacene molecules detected by fluorescence excitation in a p-terphenyl crystal*. Physical Review Letters **1990,** 65, (21), 2716-2719.
100. Garcia-Parajo, M. F.; Veerman, J. A.; Bouwhuis, R.; Vallee, R.; van Hulst, N. F. *Optical probing of single fluorescent molecules and proteins*. Chemphyschem **2001,** 2, (6), 347-360.
101. Moerner, W. E.; Fromm, D. P. *Methods of single-molecule fluorescence spectroscopy and microscopy*. Review of Scientific Instruments **2003,** 74, (8), 3597-3619.
102. Nie, S. M.; Zare, R. N. *Optical detection of single molecules*. Annual Review Of Biophysics And Biomolecular Structure **1997,** 26, 567-596.
103. http://www.microscopyu.com/tutorials/java/imageformation/airyna/.
104. Kasai, H.; Nalwa, H. S.; Oikawa, H.; Okada, S.; Matsuda, H.; Minami, N.; Kakuta, A.; Ono, K.; Mukoh, A.; Nakanishi, H. *A Novel Preparation Method of Organic Microcrystals*. Japanese Journal of Applied Physics Part 2-Letters **1992,** 31, (8A), L1132-L1134.
105. Nakanishi, H.; Oikawa, H. *Reprecipitation method for organic nanocrystals*. Single Organic Nanoparticles **2003**, 17-31.
106. Zheng, C.; Xu, X.; He, F.; Li, L.; Wu, B.; Yu, G.; Liu, Y. *Preparation of High-Quality Organic Semiconductor Nanoparticle Films by Solvent-Evaporation-Induced Self-Assembly*. Langmuir **2010,** 26, (22), 16730-16736.
107. Cravino, A.; Schilinsky, P.; Brabec, C. J. *Characterization of organic solar cells: the importance of device layout*. Advanced Functional Materials **2007,** 17, (18), 3906-3910.
108. Nunzi, J. M. *Organic photovoltaic materials and devices*. Comptes Rendus Physique **2002,** 3, (4), 523-542.
109. Shaw, P. E.; Ruseckas, A.; Samuel, I. D. W. *Exciton diffusion measurements in poly(3-hexylthiophene)*. Advanced Materials **2008,** 20, (18), 3516-3520.
110. Li, G.; Shrotriya, V.; Huang, J. S.; Yao, Y.; Moriarty, T.; Emery, K.; Yang, Y. *High-efficiency solution processable polymer photovoltaic cells by*

self-organization of polymer blends. Nature Materials **2005,** 4, (11), 864-868.

111. Jorgensen, M.; Norrman, K.; Krebs, F. C. *Stability/degradation of polymer solar cells*. Solar Energy Materials and Solar Cells **2008,** 92, (7), 686-714.
112. Campoy-Quiles, M.; Ferenczi, T.; Agostinelli, T.; Etchegoin, P. G.; Kim, Y.; Anthopoulos, T. D.; Stavrinou, P. N.; Bradley, D. D. C.; Nelson, J. *Morphology evolution via self-organization and lateral and vertical diffusion in polymer: fullerene solar cell blends*. Nature Materials **2008,** 7, (2), 158-164.
113. Stalmach, U.; de Boer, B.; Videlot, C.; van Hutten, P. F.; Hadziioannou, G. *Semiconducting diblock copolymers synthesized by means of controlled radical polymerization techniques*. Journal of the American Chemical Society **2000,** 122, (23), 5464-5472.
114. Lindner, S. M.; Huttner, S.; Chiche, A.; Thelakkat, M.; Krausch, G. *Charge separation at self-assembled nanostructured bulk interface in block copolymers*. Angewandte Chemie-International Edition **2006,** 45, (20), 3364-3368.
115. Sivula, K.; Ball, Z. T.; Watanabe, N.; Frechet, J. M. J. *Amphiphilic diblock copolymer compatibilizers and their effect on the morphology and performance of polythiophene: Fullerene solar cells*. Advanced Materials **2006,** 18, (2), 206-+.
116. Segalman, R. A.; McCulloch, B.; Kirmayer, S.; Urban, J. J. *Block Copolymers for Organic Optoelectronics*. Macromolecules **2009,** 42, (23), 9205-9216.
117. Schmitt, C.; Nothofer, H. G.; Falcou, A.; Scherf, U. *Conjugated polyfluorene/polyaniline block copolymers*. Macromolecular Rapid Communications **2001,** 22, (8), 624-628.
118. Lindner, S. M.; Thelakkat, M. *Nanostructures of n-type organic semiconductor in a p-type matrix via self-assembly of block copolymers*. Macromolecules **2004,** 37, (24), 8832-8835.
119. Ramos, A. M.; Rispens, M. T.; van Duren, J. K. J.; Hummelen, J. C.; Janssen, R. A. J. *Photoinduced electron transfer and photovoltaic devices of a conjugated polymer with pendant fullerenes*. Journal of the American Chemical Society **2001,** 123, (27), 6714-6715.
120. Richard, F.; Brochon, C.; Leclerc, N.; Eckhardt, D.; Heiser, T.; Hadziioannou, G. *Design of a linear poly(3-hexylthiophene)/fullerene-based donor-acceptor rod-coil mock copolymer*. Macromolecular Rapid Communications **2008,** 29, (11), 885-891.
121. Yang, C.; Lee, J. K.; Heeger, A. J.; Wudl, F. *Well-defined donor-acceptor rod-coil diblock copolymers based on P3HT containing C-60: the morphology and role as a surfactant in bulk-heterojunction solar cells*. Journal Of Materials Chemistry **2009,** 19, (30), 5416-5423.
122. Palacios, R. E.; Barbara, P. F. *Single molecule spectroscopy of poly 3-octyl-thiophene (P3OT)*. Journal of Fluorescence **2007,** 17, 749-757.
123. Yu, J.; Lammi, R.; Gesquiere, A. J.; Barbara, P. F. *Singlet-triplet and*

triplet-triplet interactions in conjugated polymer single molecules. Journal of Physical Chemistry B **2005,** 109, (20), 10025-10034.

124. Burrows, H. D.; Arnaut, L. G.; Pina, J.; de Melo, J. S.; Chattopadhyay, N.; Alcacer, L.; Charas, A.; Morgado, J. *Characterisation of the triplet state of a fluorene-terthiophene alternating copolymer*. Chemical Physics Letters **2005,** 402, (1-3), 197-201.
125. Hofkens, J.; Cotlet, M.; Vosch, T.; Tinnefeld, P.; Weston, K. D.; Ego, C.; Grimsdale, A.; Mullen, K.; Beljonne, D.; Bredas, J. L.; Jordens, S.; Schweitzer, G.; Sauer, M.; De Schryver, F. *Revealing competitive Forster-type resonance energy-transfer pathways in single bichromophoric molecules*. Proceedings of the National Academy of Sciences of the United States of America **2003,** 100, 13146-13151.
126. Brabec, C. J.; Zerza, G.; Cerullo, G.; De Silvestri, S.; Luzzati, S.; Hummelen, J. C.; Sariciftci, S. *Tracing photoinduced electron transfer process in conjugated polymer/fullerene bulk heterojunctions in real time*. Chemical Physics Letters **2001,** 340, (3-4), 232-236.
127. Hofkens, J.; Maus, M.; Gensch, T.; Vosch, T.; Cotlet, M.; Kohn, F.; Herrmann, A.; Mullen, K.; De Schryver, F. *Probing photophysical processes in individual multichromophoric dendrimers by single-molecule spectroscopy*. Journal of the American Chemical Society **2000,** 122, (38), 9278-9288.
128. Kaneko, T.; Matsui, H.; Shimokawa, O.; Nakahara, A.; Hyodo, I. *Cellular membrane fluidity measurement by fluorescence polarization in indomethacin-induced gastric cellular injury in vitro*. Journal of Gastroenterology **2007,** 42, (12), 939-946.
129. Feng, D. Q.; Caruso, A. N.; Losovyj, Y. B.; Shulz, D. L.; Dowben, P. A. *Identification of the possible in poly(3-hexylthiophene) thin defect states films*. Polymer Engineering And Science **2007,** 47, 1359-1364.
130. Bugar, I.; Kovac, J.; Matuszna, K.; Lukes, V.; Cik, G. *Polymer structure characterization of polythiophenes by fluorescence spectroscopy in solution*. Laser Physics **2004,** 14, (4), 527-532.
131. Wise, D. L., *Electrical and optical polymer systems*. M. Dekker: New York, 1998; p xii, 1239 p.
132. Grey, J. K.; Kim, D. Y.; Lee, Y. J.; Gutierrez, J. J.; Luong, N.; Ferraris, J. P.; Barbara, P. F. *Single-molecule studies of electronic energy transfer in a diblock conjugated polymer*. Angewandte Chemie-International Edition **2005,** 44, (38), 6207-6210.
133. Grey, J. K.; Kim, D. Y.; Lee, Y. J.; Gutierrez, J. J.; Luong, N.; Ferraris, J. P.; Barbara, P. F. *Single-Molecule Studies of Electronic Energy Transfer in a Diblock Conjugated Polymer*. Angewandte Chemie International Edition **2005,** 44, (38), 6207-6210.
134. Dante, M.; Peet, J.; Nguyen, T. Q. *Nanoscale charge transport and internal*

structure of bulk heterojunction conjugated polymer/fullerene solar cells by scanning probe microscopy. Journal of Physical Chemistry C **2008,** 112, (18), 7241-7249.

135. Waldauf, C.; Morana, M.; Denk, P.; Schilinsky, P.; Coakley, K.; Choulis, S. A.; Brabec, C. J. *Highly efficient inverted organic photovoltaics using solution based titanium oxide as electron selective contact*. Applied Physics Letters **2006,** 89, (23).
136. Lim, J. A.; Liu, F.; Ferdous, S.; Muthukumar, M.; Briseno, A. L. *Polymer semiconductor crystals*. Materials Today **2010,** 13, (5), 14-24.
137. Salleo, A. *Charge transport in polymeric transistors*. Materials Today **2007,** 10, (3), 38-45.
138. Mena-Osteritz, E.; Meyer, A.; Langeveld-Voss, B. M. W.; Janssen, R. A. J.; Meijer, E. W.; Bauerle, P. *Two-dimensional crystals of poly(3-alkylthiophene)s: Direct visualization of polymer folds in submolecular resolution*. Angewandte Chemie-international Edition **2000,** 39, (15), 2680-2684.
139. Brun, M.; Demadrille, R.; Rannou, P.; Pron, A.; Travers, J. P.; Grevin, B. *Multiscale scanning Tunneling Microscopy Study of self-assembly phenomena in two-dimensional polycrystals of pi-conjugated polymers: The case of regioregular poly (dioctylbithiophene-alt-fluore-none)*. Advanced Materials **2004,** 16, (23-24), 2087-2092.
140. Payerne, R.; Brun, M.; Rannou, P.; Baptist, R.; Grevin, B. *STM studies of poly(3-alkylthiophene)s: model systems for plastic electronics*. Synthetic Metals **2004,** 146, (3), 311-315.
141. Liu, J.; Mikhailov, I. A.; Zou, J.; Osaka, I.; Masunov, A. E.; McCullough, R. D.; Zhai, L. *Insight into How Molecular Structures of Thiophene-based Conjugated Polymers Affect Crystallization Behaviors*. Polymer **2011,** 52, (10), 2302-2309.
142. Liu, J. S.; Loewe, R. S.; McCullough, R. D. *Employing MALDI-MS on poly(alkylthiophenes): Analysis of molecular weights, molecular weight distributions, end-group structures, and end-group modifications*. Macromolecules **1999,** 32, (18), 5777-5785.
143. Liu, J. H.; Arif, M.; Zou, J. H.; Khondaker, S. I.; Zhai, L. *Controlling Poly(3-hexylthiophene) Crystal Dimension: Nanowhiskers and Nanoribbons*. Macromolecules **2009,** 42, (24), 9390-9393.
144. Hu, Z. J.; Zou, J. H.; Deibel, C.; Gesquiere, A. J.; Zhai, L. *Single-Molecule Spectroscopy and AFM Morphology Studies of a Diblock Copolymer Consisting of Poly(3-hexylthiophene) and Fullerene*. Macromolecular Chemistry and Physics **2010,** 211, (22), 2416-2424.
145. O'Connor, B.; Chan, E. P.; Chan, C.; Conrad, B. R.; Richter, L. J.; Kline, R. J.; Heeney, M.; McCulloch, I.; Soles, C. L.; DeLongchamp, D. M. *Correlations between Mechanical and Electrical Properties of Polythiophenes*. ACS Nano **2010,** 4, (12), 7538-7544.

146. Sun, Q. J.; Park, K.; Dai, L. M. *Liquid Crystalline Polymers for Efficient Bilayer-Bulk-Heterojunction Solar Cells*. Journal Of Physical Chemistry C **2009,** 113, (18), 7892-7897.
147. Wang, S.; Tang, J. C.; Zhao, L. H.; Png, R. Q.; Wong, L. Y.; Chia, P. J.; Chan, H. S. O.; Ho, P. K. H.; Chua, L. L. *Solvent effects and multiple aggregate states in high-mobility organic field-effect transistors based on poly(bithiophene-alt-thienothiophene)*. Applied Physics Letters **2008,** 93, (16).
148. Cook, S.; Furube, A.; Katoh, R. *Analysis of the excited states of regioregular polythiophene P3HT*. Energy & Environmental Science **2008,** 1, (2), 294-299.
149. Taliani, C.; Blinov, L. M. *The electronic structure of solid alpha-sexithiophene*. Advanced Materials **1996,** 8, (4), 353-359.
150. Osaka, I.; Sauve, G.; Zhang, R.; Kowalewski, T.; McCullough, R. D. *Novel thiophene-thiazolothiazole copolymers for organic field-effect transistors*. Advanced Materials **2007,** 19, (23), 4160-+.
151. Osaka, I.; Zhang, R.; Sauve, G.; Smilgies, D. M.; Kowalewski, T.; McCullough, R. D. *High-Lamellar Ordering and Amorphous-Like pi-Network in Short-Chain Thiazolothiazole-Thiophene Copolymers Lead to High Mobilities*. Journal of the American Chemical Society **2009,** 131, (7), 2521-2529.
152. Zhang, X. N.; Johnson, J. P.; Kampf, J. W.; Matzger, A. J. *Ring fusion effects on the solid-state properties of alpha-oligothiophenes*. Chemistry Of Materials **2006,** 18, (15), 3470-3476.
153. Zhang, X. N.; Matzger, A. J. *Effect of ring fusion on the electronic absorption and emission properties of oligothiophenes*. Journal Of Organic Chemistry **2003,** 68, (25), 9813-9815.
154. Quan, S. Y.; Teng, F.; Xu, Z.; Quan, L.; Zhang, T.; Liu, D.; Hou, Y. B.; Wang, Y. S.; Xu, X. R. *Temperature dependence of photoluminescence in MEH-PPV blend films*. Journal of Luminescence **2007,** 124, (1), 81-84.
155. Spano, F. C. *Modeling disorder in polymer aggregates: The optical spectroscopy of regioregular poly(3-hexylthiophene) thin films*. Journal of Chemical Physics **2005,** 122, (23).
156. Cleave, V.; Yahioglu, G.; Le Barny, P.; Friend, R. H.; Tessler, N. *Harvesting singlet and triplet energy in polymer LEDs*. Advanced Materials **1999,** 11, (4), 285-288.
157. Garnier, F.; Hajlaoui, R.; Yassar, A.; Srivastava, P. *All-Polymer Field-Effect Transistor Realized by Printing Techniques*. Science **1994,** 265, (5179), 1684-1686.
158. Bao, Z.; Dodabalapur, A.; Lovinger, A. J. *Soluble and processable regioregular poly(3-hexylthiophene) for thin film field-effect transistor applications with high mobility*. Applied Physics Letters **1996,** 69, (26), 4108-4110.
159. Friend, R. H.; Gymer, R. W.; Holmes, A. B.; Burroughes, J. H.; Marks, R. N.; Taliani, C.; Bradley, D. D. C.; Dos Santos, D. A.; Bredas, J. L.; Logdlund, M.;

Salaneck, W. R. *Electroluminescence in conjugated polymers*. Nature **1999,** 397, (6715), 121-128.

160. Sirringhaus, H.; Tessler, N.; Friend, R. H. *Integrated optoelectronic devices based on conjugated polymers*. Science **1998,** 280, (5370), 1741-1744.
161. Drori, T.; Sheng, C. X.; Ndobe, A.; Singh, S.; Holt, J.; Vardeny, Z. V. *Below-gap excitation of pi-conjugated polymer-fullerene blends: Implications for bulk organic heterojunction solar cells*. Physical Review Letters **2008,** 101, (3), 037401.
162. Yu, G.; Gao, J.; Hummelen, J. C.; Wudl, F.; Heeger, A. J. *Polymer Photovoltaic Cells - Enhanced Efficiencies Via a Network of Internal Donor-Acceptor Heterojunctions*. Science **1995,** 270, (5243), 1789-1791.
163. Lindner, T.; Paasch, G.; Scheinert, S. *Influence of distributed trap states on the characteristics of top and bottom contact organic field-effect transistors*. Journal of Materials Research **2004,** 19, (7), 2014-2027.
164. Lindner, T.; Paasch, G.; Scheinert, S. *Hysteresis in organic field-effect devices: Simulated effects due to trap recharging*. Journal of Applied Physics **2005,** 98, (11), 114505
165. Ma, W. L.; Yang, C. Y.; Heeger, A. J. *Spatial Fourier-transform analysis of the morphology of bulk heterojunction materials used in "plastic" solar cells*. Advanced Materials **2007,** 19, (10), 1387-+.
166. Dante, M.; Garcia, A.; Nguyen, T.-Q. *Three-Dimensional Nanoscale Organization of Highly Efficient Low Band-Gap Conjugated Polymer Bulk Heterojunction Solar Cells*. The Journal of Physical Chemistry C **2009,** 113, (4), 1596-1600.
167. Grey, J. K.; Kim, D. Y.; Norris, B. C.; Miller, W. L.; Barbara, P. F. *Size-dependent spectroscopic properties of conjugated polymer nanoparticles*. Journal of Physical Chemistry B **2006,** 110, (51), 25568-25572.
168. Szymanski, C.; Wu, C. F.; Hooper, J.; Salazar, M. A.; Perdomo, A.; Dukes, A.; McNeill, J. *Single molecule nanoparticles of the conjugated polymer MEH-PPV, preparation and characterization by near-field scanning optical microscopy*. Journal Of Physical Chemistry B **2005,** 109, (18), 8543-8546.
169. Wang, F.; Han, M. Y.; Mya, K. Y.; Wang, Y. B.; Lai, Y. H. *Aggregation-driven growth of size-tunable organic nanoparticles using electronically altered conjugated polymers*. Journal of the American Chemical Society **2005,** 127, (29), 10350-10355.
170. Kurokawa, N.; Yoshikawa, H.; Hirota, N.; Hyodo, K.; Masuhara, H. *Size-dependent spectroscopic properties and thermochromic behavior in poly(substituted thiophene) nanoparticles*. Chemphyschem **2004,** 5, (10), 1609-1615.
171. Scheblykin, I.; Zoriniants, G.; Hofkens, J.; De Feyter, S.; Van der Auweraer, M.; De Schryver, F. C. *Photoluminescence intensity fluctuations and*

electric-field-induced photoluminescence quenching in individual nanoclusters of poly(phenylenevinylene). Chemphyschem **2003,** 4, (3), 260-267.

172. Moerner, W. E.; Orrit, M. *Illuminating single molecules in condensed matter*. Science **1999,** 283, 1670-1676.
173. Orrit, M.; Bernard, J.; Personov, R. I. *High-Resolution Spectroscopy of Organic-Molecules in Solids - from Fluorescence Line Narrowing and Hole-Burning to Single-Molecule Spectroscopy*. Journal of Physical Chemistry **1993,** 97, (40), 10256-10268.
174. Nie, S.; Zare, R. *Optical Detection of Single Molecules*. Annu. Rev. Biophys. Biomol. Struct. **1997,** 26, 567-596.
175. Ambrose, W. P.; Goodwin, P. M.; Jett, J. H.; Van Orden, A.; Werner, J. H.; Keller, R. A. *Single Molecule Fluorescence Spectroscopy at Ambient Temperature*. Chem. Rev. **1999,** 99, (10), 2929-2956.
176. Xie, X. S.; Trautman, J. K. *Optical Studies of Single Molecules at Room Temperature*. Annu. Rev. Phys. Chem. **1998,** 49, 441-480.
177. Huser, T.; Yan, M.; Rothberg, L. J. *Single chain spectroscopy of conformational dependence of conjugated polymer photophysics*. Proceedings of the National Academy of Sciences of the United States of America **2000,** 97, (21), 11187-11191.
178. Schindler, F.; Lupton, J. M.; Feldmann, J.; Scherf, U. *A universal picture of chromophores in pi-conjugated polymers derived from single-molecule spectroscopy*. Proceedings of the National Academy of Sciences of the United States of America **2004,** 101, (41), 14695-14700.
179. Gesquiere, A. J.; Uwada, T.; Asahi, T.; Masuhara, H.; Barbara, P. F. *Single molecule spectroscopy of organic dye nanoparticles*. Nano Letters **2005,** 5, (7), 1321-1325.
180. Markiewicz, P.; Goh, M. C. *Atomic-Force Microscopy Probe Tip Visualization and Improvement of Images Using a Simple Deconvolution Procedure*. Langmuir **1994,** 10, (1), 5-7.
181. Zhou, X. F.; Xu, H.; Fan, C. H.; Sun, J. L.; Zhang, Y.; Li, M. Q.; Shen, W. Q.; Hu, J. *Compression of single conjugated-polymer nanoparticles with AFM tips*. Chemistry Letters **2005,** 34, (11), 1488-1489.
182. Grey, J. K.; Kim, D. Y.; Norris, B. C.; Miller, W. L.; Barbara, P. F. *Size-dependent spectroscopic properties of conjugated polymer nanoparticles*. Journal of Physical Chemistry B **2006,** 110, 25568-25572.
183. Hirota, N.; Hisamatsu, N.; Maeda, S.; Tsukahara, H.; Hyodo, K. *Thermochromism of poly(substituted thiophene) with urethane bond and its application to reversible thermal recording*. Synthetic Metals **1996,** 80, (1), 67-72.
184. Schwartz, B. J. *Conjugated polymers as molecular materials : How chain conformation and film morphology influence energy transfer and interchain*

interactions. Annual Review of Physical Chemistry **2003,** 54, 141-172.

185. Brown, P. J.; Thomas, D. S.; Kohler, A.; Wilson, J. S.; Kim, J. S.; Ramsdale, C. M.; Sirringhaus, H.; Friend, R. H. *Effect of interchain interactions on the absorption and emission of poly(3-hexylthiophene)*. Physical Review B **2003,** 67, (6), 064203.
186. Clark, J.; Silva, C.; Friend, R. H.; Spano, F. C. *Role of intermolecular coupling in the photophysics of disordered organic semiconductors: Aggregate emission in regioregular polythiophene*. Physical Review Letters **2007,** 98, (20), 206406.
187. Heffner, G. W.; Pearson, D. S. *Molecular Characterization of Poly(3-Hexylthiophene)*. Macromolecules **1991,** 24, (23), 6295-6299.
188. Bai, X.; Holdcroft, S. *Molecular Control of Luminescence from Poly(3-Hexylthiophenes)*. Macromolecules **1993,** 26, (17), 4457-4460.
189. Padmanaban, G.; Ramakrishnan, S. *Conjugation length control in soluble poly[2-methoxy-5-((2 '-ethylhexyl)oxy)-1,4-phenylenevinylene] (MEHPPV): Synthesis, optical properties, and energy transfer*. Journal of The American Chemical Society **2000,** 122, (10), 2244-2251.
190. Shrotriya, V.; Ouyang, J.; Tseng, R. J.; Li, G.; Yang, Y. *Absorption spectra modification in poly(3-hexylthiophene): methanofullerene blend thin films*. Chemical Physics Letters **2005,** 411, (1-3), 138-143.
191. Traiphol, R.; Sanguansat, P.; Srikhirin, T.; Kerdcharoen, T.; Osotchan, T. *Spectroscopic study of photophysical change in collapsed coils of conjugated polymers: Effects of solvent and temperature*. Macromolecules **2006,** 39, (3), 1165-1172.
192. Padmanaban, G.; Ramakrishnan, S. *Fluorescence spectroscopic studies of solvent- and temperature-induced conformational transition in segmented poly[2-methoxy-5-(2 '-ethylhexyl)oxy-1,4-phenylenevinylene] (MEHPPV)*. Journal Of Physical Chemistry B **2004,** 108, (39), 14933-14941.
193. Martini, I. B.; Smith, A. D.; Schwartz, B. J. *Exciton-exciton annihilation and the production of interchain species in conjugated polymer films: Comparing the ultrafast stimulated emission and photoluminescence dynamics of MEH-PPV*. Physical Review B **2004,** 69, (3).
194. Wu, C. F.; Szymanski, C.; McNeill, J. *Preparation and encapsulation of highly fluorescent conjugated polymer nanoparticles*. Langmuir **2006,** 22, (7), 2956-2960.
195. Dyakonov, V.; Zoriniants, G.; Scharber, M.; Brabec, C. J.; Janssen, R. A. J.; Hummelen, J. C.; Sariciftci, N. S. *Photoinduced charge carriers in conjugated polymer-fullerene composites studied with light-induced electron-spin resonance*. Physical Review B **1999,** 59, (12), 8019-8025.
196. Li, Y. N.; Vamvounis, G.; Holdcroft, S. *Tuning optical properties and enhancing solid-state emission of poly(thiophene)s by molecular control: A postfunctionalization approach*. Macromolecules **2002,** 35, (18), 6900-6906.

197. Wang, J.; Wang, D.; Miller, E. K.; Moses, D.; Heeger, A. J. *Static and dynamic photoluminescence (PL) quenching of polymer : quencher systems in solutions*. Synthetic Metals **2001,** 119, (1-3), 591-592.
198. Wang, J.; Wang, D. L.; Moses, D.; Heeger, A. J. *Dynamic quenching of 5-(2 '-ethyl-hexyloxy)-p-phenylene vinylene (MEH-PPV) by charge transfer to a C-60 derivative in solution*. Journal of Applied Polymer Science **2001,** 82, (10), 2553-2557.
199. Piris, J.; Dykstra, T. E.; Bakulin, A. A.; van Loosdrecht, P. H. M.; Knulst, W.; Trinh, M. T.; Schins, J. M.; Siebbeles, L. D. A. *Photogeneration and Ultrafast Dynamics of Excitons and Charges in P3HT/PCBM Blends*. Journal Of Physical Chemistry C **2009,** 113, (32), 14500-14506.
200. Nguyen, L. H.; Hoppe, H.; Erb, T.; Gunes, S.; Gobsch, G.; Sariciftci, N. S. *Effects of annealing on the nanomorphology and performance of poly(alkylthiophene): fullerene bulk-heterojunction solar cells*. Advanced Functional Materials **2007,** 17, (7), 1071-1078.
201. Grey, J. K.; Kim, D. Y.; Donley, C. L.; Miller, W. L.; Kim, J. S.; Silva, C.; Friend, R. H.; Barbara, P. F. *Effect of temperature and chain length on the bimodal emission properties of single polyfluorene copolymer molecules*. Journal of Physical Chemistry B **2006,** 110, (38), 18898-18903.
202. Braeken, E.; Marsal, P.; Vandendriessche, A.; Smet, M.; Dehaen, W.; Vallee, R. A. L.; Beljonne, D.; Van der Auweraer, M. *Investigation of probe molecule-polymer interactions*. Chemical Physics Letters **2009,** 472, (1-3), 48-54.
203. Hofkens, J.; Vosch, T.; Maus, M.; Kohn, F.; Cotlet, M.; Weil, T.; Herrmann, A.; Mullen, K.; De Schryver, F. C. *Conformational rearrangements in and twisting of a single molecule*. Chemical Physics Letters **2001,** 333, (3-4), 255-263.
204. Stracke, F.; Blum, C.; Becker, S.; Mullen, K.; Meixner, A. J. *Correlation of emission intensity and spectral diffusion in room temperature single-molecule spectroscopy*. Chemphyschem **2005,** 6, (7), 1242-1246.
205. Bolognesi, A.; Porzio, W.; Provasoli, A.; Botta, C.; Comotti, A.; Sozzani, P.; Simonutti, R. *Structural and thermal behavior of poly(3-octylthiophene): a DSC, C-13 MAS NMR, XRD, photoluminescence, and Raman scattering study*. Macromolecular Chemistry And Physics **2001,** 202, (12), 2586-2591.
206. Ho, P. K. H.; Kim, J. S.; Tessler, N.; Friend, R. H. *Photoluminescence of poly(p-phenylenevinylene)-silica nanocomposites: Evidence for dual emission by Franck-Condon analysis*. Journal of Chemical Physics **2001,** 115, (6), 2709-2720.
207. Bjorklund, T. G.; Lim, S. H.; Bardeen, C. J. *The optical spectroscopy of poly (p-phenylene vinylene)/polyvinyl alcohol blends: from aggregates to isolated chromophores*. Synthetic Metals **2004,** 142, (1-3), 195-200.
208. Collison, C. J.; Rothberg, L. J.; Treemaneekarn, V.; Li, Y. *Conformational*

effects on the photophysics of conjugated polymers: A two species model for MEH-PPV spectroscopy and dynamics. Macromolecules **2001,** 34, (7), 2346-2352.

209. He, G. F.; Li, Y. F.; Liu, J.; Yang, Y. *Enhanced electroluminescence using polystyrene as a matrix*. Applied Physics Letters **2002,** 80, (22), 4247-4249.
210. Brown, P. J.; Thomas, D. S.; Kohler, A.; Wilson, J. S.; Kim, J. S.; Ramsdale, C. M.; Sirringhaus, H.; Friend, R. H. *Effect of interchain interactions on the absorption and emission of poly(3-hexylthiophene)*. Physical Review B **2003,** 67, (6).
211. Clark, J.; Silva, C.; Friend, R. H.; Spano, F. C. *Role of intermolecular coupling in the photophysics of disordered organic semiconductors: aggregate emission in regioregular polythiophene*. Phys Rev Lett **2007,** 98, (20), 206406.
212. Meskers, S. C. J.; Janssen, R. A. J.; Haverkort, J. E. M.; Wolter, J. H. *Relaxation of photo-excitations in films of oligo- and poly(para-phenylene vinylene) derivatives*. Chemical Physics **2000,** 260, (3), 415-439.
213. Chen, T. A.; Wu, X. M.; Rieke, R. D. *Regiocontrolled Synthesis of Poly(3-alkylthiophenes) Mediated by Rieke Zinc: Their Characterization and Solid-State Properties*. Journal of The American Chemical Society **1995,** 117, (1), 233-244.
214. Prosa, T. J.; Winokur, M. J.; Moulton, J.; Smith, P.; Heeger, A. J. *X-Ray Structural Studies of Poly(3-Alkylthiophenes) - an Example of an Inverse Comb*. Macromolecules **1992,** 25, (17), 4364-4372.
215. Prosa, T. J.; Winokur, M. J.; McCullough, R. D. *Evidence of a novel side chain structure in regioregular poly(3-alkylthiophenes)*. Macromolecules **1996,** 29, (10), 3654-3656.
216. Ruseckas, A.; Namdas, E. B.; Ganguly, T.; Theander, M.; Svensson, M.; Andersson, M. R.; Inganas, O.; Sundstrom, V. *Intra- and interchain luminescence in amorphous and semicrystalline films of phenyl-substituted polythiophene*. Journal of Physical Chemistry B **2001,** 105, (32), 7624-7631.
217. Bolognesi, A.; Porzio, W.; Zhuo, G.; Ezquerra, T. *The thermal behaviour of poly(3-octylthienylene) synthesized by an Ni-based catalyst: DSC, optical microscopy and XRD analyses*. European Polymer Journal **1996,** 32, (9), 1097-1103.
218. Chandler, D. *Interfaces and the driving force of hydrophobic assembly*. Nature **2005,** 437, 640-647.
219. ten Wolde, P. R.; Chandler, D. *Drying-induced hydrophobic polymer collapse*. Proceedings of the National Academy of Sciences of the United States of America **2002,** 99, (10), 6539-6543.
220. A. C. Mayer; Michael F. Toney; Shawn R. Scully; Jonathan Rivnay; Christoph J. Brabec; Marcus Scharber; Marcus Koppe; Martin Heeney; Iain McCulloch; McGehee, M. D. *Bimolecular Crystals of Fullerenes in Conjugated Polymers*

and the Implications of Molecular Mixing for Solar Cells Advanced Functional Materials **2009,** 19, (8), 1173 - 1179.

221. Koppe, M.; Scharber, M.; Brabec, C.; Duffy, W.; Heeney, M.; McCulloch, I. *Polyterthiophenes as donors for polymer solar cells*. Advanced Functional Materials **2007,** 17, (8), 1371-1376.
222. Geng, J. X.; Zeng, T. Y. *Influence of single-walled carbon nanotubes induced crystallinity enhancement and morphology change on polymer photovoltaic devices*. Journal of the American Chemical Society **2006,** 128, (51), 16827-16833.
223. Liang, Y. Y.; Xu, Z.; Xia, J. B.; Tsai, S. T.; Wu, Y.; Li, G.; Ray, C.; Yu, L. P. *For the Bright Future-Bulk Heterojunction Polymer Solar Cells with Power Conversion Efficiency of 7.4%*. Advanced Materials **2010,** 22, (20), E135-E138.
224. Zaumseil, J.; Sirringhaus, H. *Electron and ambipolar transport in organic field-effect transistors*. Chemical Reviews **2007,** 107, (4), 1296-1323.
225. Meijer, E. J.; De Leeuw, D. M.; Setayesh, S.; Van Veenendaal, E.; Huisman, B. H.; Blom, P. W. M.; Hummelen, J. C.; Scherf, U.; Klapwijk, T. M. *Solution-processed ambipolar organic field-effect transistors and inverters*. Nature Materials **2003,** 2, (10), 678-682.
226. Marjanovic, N.; Singh, T. B.; Dennler, G.; Gunes, S.; Neugebauer, H.; Sariciftci, N. S.; Schwodiauer, R.; Bauer, S. *Photoresponse of organic field-effect transistors based on conjugated polymer/fullerene blends*. Organic Electronics **2006,** 7, (4), 188-194.
227. Bredas, J. L.; Norton, J. E.; Cornil, J.; Coropceanu, V. *Molecular Understanding of Organic Solar Cells: The Challenges*. Accounts of Chemical Research **2009,** 42, (11), 1691-1699.
228. Ferguson, A. J.; Kopidakis, N.; Shaheen, S. E.; Rumbles, G. *Quenching of excitons by holes in poly(3-hexylthiophene) films*. Journal of Physical Chemistry C **2008,** 112, (26), 9865-9871.
229. Liu, C. Y.; Chen, S. A. *Charge mobility and charge traps in conjugated polymers*. Macromolecular Rapid Communications **2007,** 28, (17), 1743-1760.
230. Byers, J. C.; Ballantyne, S.; Rodionov, K.; Mann, A.; Semenikhin, O. A. *Mechanism of Recombination Losses in Bulk Heterojunction P3HT: PCBM Solar Cells Studied Using Intensity Modulated Photocurrent Spectroscopy*. Acs Applied Materials & Interfaces **2011,** 3, (2), 392-401.
231. Groves, C.; Blakesley, J. C.; Greenham, N. C. *Effect of Charge Trapping on Geminate Recombination and Polymer Solar Cell Performance*. Nano Letters **2010,** 10, (3), 1063-1069.
232. Chang, W.-S.; Link, S.; Yethiraj, A.; Barbara, P. F. *Single molecule spectroscopy of conjugated polymer chains in an electric field-aligned liquid crystal*. Journal Of Physical Chemistry B **2008,** 112, (2), 448-453.
233. Sherwood, G. A.; Cheng, R.; Smith, T. M.; Werner, J. H.; Shreve, A. P.; Peteanu,

L. A.; Wildeman, J. *Aggregation Effects on the Emission Spectra and Dynamics of Model Oligomers of MEH-PPV*. Journal Of Physical Chemistry C **2009,** 113, (43), 18851-18862.

234. Karam, P.; Ngo, A. T.; Rouiller, I.; Cosa, G. *Unraveling electronic energy transfer in single conjugated polyelectrolytes encapsulated in lipid vesicles*. Proceedings of the National Academy of Sciences of the United States of America **2010,** 107, (41), 17480-17485.
235. Tcherniak, A.; Ha, J. W.; Dominguez-Medina, S.; Slaughter, L. S.; Link, S. *Probing a Century Old Prediction One Plasmonic Particle at a Time*. Nano Letters **2010,** 10, (4), 1398-1404.
236. English, D. S.; Harbron, E. J.; Barbara, P. F. *Role of rare sites in single molecule spectroscopy measurements of spectral diffusion*. Journal of Chemical Physics **2001,** 114, (23), 10479-10485.
237. Patra, D. *Application and new developments in fluorescence spectroscopic techniques in studying individual molecules*. Applied Spectroscopy Reviews **2008,** 43, (5), 389-415.
238. Reznik, C.; Berg, R.; Foster, E.; Advincula, R.; Landes, C. F. *Transient Three-Dimensional Orientation of Molecular Ions in an Ordered Polyelectrolyte Membrane*. Journal of Physical Chemistry Letters **2011,** 2, (6), 592-598.
239. Yu, J.; Song, N. W.; McNeill, J. D.; Barbara, P. F. *Efficient exciton quenching by hole polarons in the conjugated polymer MEH-PPV*. Israel Journal of Chemistry **2004,** 44, (1-3), 127-132.
240. Palacios, R. E.; Fan, F. R. F.; Grey, J. K.; Suk, J.; Bard, A. J.; Barbara, P. F. *Charging and discharging of single conjugated-polymer nanoparticles*. Nature Materials **2007,** 6, (9), 680-685.
241. Gesquiere, A. J.; Park, S. J.; Barbara, P. F. *Hole-induced quenching of triplet and singlet excitons in conjugated polymers*. Journal of the American Chemical Society **2005,** 127, (26), 9556-9560.
242. Park, S. J.; Gesquiere, A. J.; Yu, J.; Barbara, P. F. *Charge injection and photooxidation of single conjugated polymer molecules*. Journal of the American Chemical Society **2004,** 126, (13), 4116-4117.
243. Gesquiere, A. J.; Lee, Y. J.; Yu, J.; Barbara, P. F. *Single molecule modulation spectroscopy of conjugated polymers*. Journal of Physical Chemistry B **2005,** 109, (25), 12366-12371.
244. Bolinger, J. C.; Fradkin, L.; Lee, K. J.; Palacios, R. E.; Barbara, P. F. *Light-assisted deep-trapping of holes in conjugated polymers*. Proceedings of the National Academy of Sciences of the United States of America **2009,** 106, (5), 1342-1346.
245. Lee, Y. J.; Park, S. J.; Gesquiere, A. J.; Barbara, P. F. *Probing a molecular interface in a functioning organic diode*. Applied Physics Letters **2005,** 87, (5),

051906.

246. Palacios, R. E.; Lee, K. J.; Rival, A.; Adachi, T.; Bolinger, J. C.; Fradkin, L.; Barbara, P. F. *Single conjugated polymer nanoparticle capacitors*. Chemical Physics **2009,** 357, (1-3), 21-27.
247. Fradkin, L.; Palacios, R. E.; Bolinger, J. C.; Lee, K. J.; Lackowski, W. M.; Barbara, P. F. *Factors Controlling Hole Injection in Single Conjugated Polymer Molecules*. Journal of Physical Chemistry A **2009,** 113, (16), 4739-4745.
248. Bolinger, J.; Lee, K. J.; Palacios, R. E.; Barbara, P. F. *Detailed Investigation of Light Induced Charge Injection into a Single Conjugated Polymer Chain*. Journal Of Physical Chemistry C **2008,** 112, (47), 18608-18615.
249. Chen, C. C.; Chiu, M. Y.; Sheu, J. T.; Wei, K. H. *Photoresponses and memory effects in organic thin film transistors incorporating poly(3-hexylthiophene)/CdSe quantum dots*. Applied Physics Letters **2008,** 92, (14), 143105.
250. Mohamad, K. A.; Goto, K.; Uesugi, K.; Fukuda, H. *Poly(3-hexylthiophene)/Fullerene Organic Thin-Film Transistors: Investigation of Photoresponse and Memory Effects*. Japanese Journal Of Applied Physics **2010,** 49, (6), 06GG09.
251. Lancaster, J.; Taylor, D. M.; Sayers, P.; Gomes, H. L. *Voltage- and light-induced hysteresis effects at the high-k dielectric- poly(3-hexylthiophene) interface*. Applied Physics Letters **2007,** 90, (10), 103513.
252. Taylor, D. M.; Drysdale, J. A.; Torres, I.; Fernandez, O. *Electron trapping and inversion layer formation in photoexcited metal-insulator-poly(3-hexylthiophene) capacitors*. Applied Physics Letters **2006,** 89, (18), 183512.
253. Jørgensen, M.; Norrman, K.; Krebs, F. C. *Stability/degradation of polymer solar cells*. Solar Energy Materials and Solar Cells **2008,** 92, (7), 686-714.
254. Dicker, G.; de Haas, M. P.; Siebbeles, L. D. A.; Warman, J. M. *Electrodeless time-resolved microwave conductivity study of charge-carrier photogeneration in regioregular poly(3-hexylthiophene) thin films*. Physical Review B **2004,** 70, (4), 045203.
255. Sheng, C. X.; Tong, M.; Singh, S.; Vardeny, Z. V. *Experimental determination of the charge/neutral branching ratio eta in the photoexcitation of pi-conjugated polymers by broadband ultrafast spectroscopy*. Physical Review B **2007,** 75, (8), 085206.
256. Karg, S.; Steiger, J.; von Seggern, H. *Determination of trap energies in Alq(3) and TPD*. Synthetic Metals **2000,** 111, 277-280.
257. Grzegorczyk, W. J.; Savenije, T. J.; Dykstra, T. E.; Piris, J.; Schins, J. M.; Siebbeles, L. D. A. *Temperature-Independent Charge Carrier Photogeneration in P3HT-PCBM Blends with Different Morphology*. Journal Of Physical Chemistry C **2010,** 114, (11), 5182-5186.

258. Youn, J. H.; Lee, Y. I.; Moon, H. T.; Ryu, M. S.; Kim, J.; Jang, J. *Trap energy level of P3HT: PCBM-71 bulk heterojunction solar cells with PICTS (photo-induced current transient spectroscopy)*. Current Applied Physics **2010,** 10, (3), S525-S527.
259. Nam, C. Y.; Su, D.; Black, C. T. *High-Performance Air-Processed Polymer-Fullerene Bulk Heterojunction Solar Cells*. Advanced Functional Materials **2009,** 19, (22), 3552-3559.
260. Grunnet-Jepsen, A.; Wright, D.; Smith, B.; Bratcher, M. S.; DeClue, M. S.; Siegel, J. S.; Moerner, W. E. *Spectroscopic determination of trap density in C-60-sensitized photorefractive polymers*. Chemical Physics Letters **1998,** 291, (5-6), 553-561.
261. Kusunoki, T.; Nakayama, K.; Pu, Y. J.; Kido, J. *Mobility Improvement in N-Type Organic FET with Hetero-Layered Structure*. Molecular Crystals And Liquid Crystals **2009,** 504, 124-132.
262. Liu, J. Q.; Yin, Z. Y.; Cao, X. H.; Zhao, F.; Lin, A. P.; Xie, L. H.; Fan, Q. L.; Boey, F.; Zhang, H.; Huang, W. *Bulk Heterojunction Polymer Memory Devices with Reduced Graphene Oxide as Electrodes*. Acs Nano **2010,** 4, (7), 3987-3992.
263. Singh, B.; Marjanovic, N.; Sariciftci, N. S.; Schwodiauer, R.; Bauer, S. *Electrical characteristics of metal-insulator-semiconductor diodes and transistors with space charge electret insulators: Towards nonvolatile organic memories*. Ieee Transactions on Dielectrics and Electrical Insulation **2006,** 13, (5), 1082-1086.
264. Chu, C. W.; Ouyang, J.; Tseng, H. H.; Yang, Y. *Organic donor-acceptor system exhibiting electrical bistability for use in memory devices*. Advanced Materials **2005,** 17, (11), 1440-1443.
265. William, S.; Mabrook, M. F.; Taylor, D. M. *Floating-gate memory based on an organic metal-insulator-semiconductor capacitor*. Applied Physics Letters **2009,** 95, (9), 093309.
266. Yun, M.; Ravindran, R.; Hossain, M.; Gangopadhyay, S.; Scherf, U.; Bunnagel, T.; Galbrecht, F.; Arif, M.; Guha, S. *Capacitance-voltage characterization of polyfluorene-based metal-insulator-semiconductor diodes*. Applied Physics Letters **2006,** 89, (1), 013506.
267. Chen, L. M.; Hong, Z. R.; Li, G.; Yang, Y. *Recent Progress in Polymer Solar Cells: Manipulation of Polymer: Fullerene Morphology and the Formation of Efficient Inverted Polymer Solar Cells*. Advanced Materials **2009,** 21, (14-15), 1434-1449.
268. Wienk, M. M.; Struijk, M. P.; Janssen, R. A. J. *Low band gap polymer bulk heterojunction solar cells*. Chemical Physics Letters **2006,** 422, (4-6), 488-491.
269. Yao, Y.; Shi, C. J.; Li, G.; Shrotriya, V.; Pei, Q. B.; Yang, Y. *Effects of C-70 derivative in low band gap polymer photovoltaic devices: Spectral*

complementation and morphology optimization. Applied Physics Letters **2006,** 89, (15).

270. Ouyang, J.; Xia, Y. *High-performance polymer photovoltaic cells with thick P3HT:PCBM films prepared by a quick drying process*. Solar Energy Materials and Solar Cells **2009,** 93, (9), 1592-1597.
271. Rogers, J. T.; Schmidt, K.; Toney, M. F.; Kramer, E. J.; Bazan, G. C. *Structural Order in Bulk Heterojunction Films Prepared with Solvent Additives*. Advanced Materials **2011**, 2284-2288.
272. Zhang, S. M.; Fan, H. J.; Liu, Y.; Zhao, G. J.; Li, Q. K.; Li, Y. F.; Zhan, X. W. *Soluble Dithienothiophene Polymers: Effect of Link Pattern*. Journal Of Polymer Science Part A-polymer Chemistry **2009,** 47, (11), 2843-2852.
273. Gupta, D.; Bag, M.; Narayan, K. S. *Correlating reduced fill factor in polymer solar cells to contact effects*. Applied Physics Letters **2008,** 92, (9), 093301.
274. An, B. K.; Kwon, S. K.; Jung, S. D.; Park, S. Y. *Enhanced emission and its switching in fluorescent organic nanoparticles*. Journal Of The American Chemical Society **2002,** 124, (48), 14410-14415.
275. Shimizu, M.; Hiyama, T. *Organic Fluorophores Exhibiting Highly Efficient Photoluminescence in the Solid State*. Chemistry-an Asian Journal **2010,** 5, (7), 1516-1531.
276. Jin, H.; Tuomikoski, M.; Hiltunen, J.; Kopola, P.; Maaninen, A.; Pino, F. *Polymer-Electrode Interfacial Effect on Photovoltaic Performances in Poly(3-hexylthiophene):Phenyl-C61-butyric Acid Methyl Ester Based Solar Cells*. Journal Of Physical Chemistry C **2009,** 113, (38), 16807-16810.